

MASTER

Modeling and design of air cooler applicable in a heat pump

Slakhorst, Karsten H.E.

Award date:
2023

[Link to publication](#)

Disclaimer

This document contains a student thesis (bachelor's or master's), as authored by a student at Eindhoven University of Technology. Student theses are made available in the TU/e repository upon obtaining the required degree. The grade received is not published on the document as presented in the repository. The required complexity or quality of research of student theses may vary by program, and the required minimum study period may vary in duration.

General rights

Copyright and moral rights for the publications made accessible in the public portal are retained by the authors and/or other copyright owners and it is a condition of accessing publications that users recognise and abide by the legal requirements associated with these rights.

- Users may download and print one copy of any publication from the public portal for the purpose of private study or research.
- You may not further distribute the material or use it for any profit-making activity or commercial gain

DEPARTMENT OF MECHANICAL ENGINEERING -
POWER & FLOW

Master Thesis

Modeling and design of air cooler applicable in a heat pump

K.H.E. (Karsten) Slakhorst
1011254

“This report was made in accordance with the TU/e Code of Scientific Conduct for the Master thesis”

Supervisor Alliander: ir. H. (Hans) Korsman
1st supervisor TU/e: dr. ir. B.P.M. (Bart) van Esch
2nd supervisor TU/e: dr. ir. M.F.M. (Michel) Speetjens

Contents

1	Introduction	6
2	Background	8
2.1	Heat exchange geometries	8
2.2	Frost formation	9
2.2.1	Frost growth	9
2.2.2	Density	11
2.2.3	Effective thermal conductivity	11
2.2.4	Specific heat capacity	11
2.3	Heat & mass transfer	12
2.3.1	Convection	12
2.3.2	Conduction	12
2.3.3	Nusselt number	12
2.3.4	Condensation	13
2.4	Simple-heat exchange model	13
3	Model description	15
3.1	MATLAB model	15
3.1.1	Condensation	16
3.1.2	Frost growth	17
3.1.3	Heat transfer coefficient	18
3.1.4	Model description - Counter flow	19
3.1.5	Model description - Cross flow	21
3.1.6	Model assembly	23
3.1.7	Iterative solving	25
3.1.8	Mesh/time convergence	28
3.2	ANSYS model	29
3.2.1	Model explanation	29
3.2.2	Solvers	31
3.2.3	Geometries	32
3.2.4	Mesh/time convergence	33
4	Validation	36
4.1	Heat exchanger conditions	36
4.2	Dry conditions	36
4.3	Wet conditions	42
4.4	Frost conditions	45
5	Results	49
5.1	Dry conditions	49
5.1.1	Temperature difference	49
5.1.2	Domain height	50
5.1.3	Domain length	51
5.2	Wet conditions	52
5.2.1	Temperature difference	53
5.2.2	Humidity	54
5.3	Frost conditions	56
5.3.1	Temperature difference	56
5.3.2	Humidity	59
6	Discussion	62
7	Conclusions and Recommendations	65
7.1	Conclusions	65
7.2	Recommendations	65

A	Condensation & Deposition	69
A.1	Contact with a surface	69
A.2	Decrease air temperature	70
A.3	Deposition	71
B	ANSYS model	72
B.1	Volume of Fluid (VOF)	72
B.2	Solidification	73
B.3	Turbulence boundary conditions	74
C	Algorithm flowchart	76
D	Validation results	77
D.1	Processing results 2D counterflow model	77
D.2	Validation results	77
E	Results	80

Nomenclature

<i>Greek symbols</i>			Pr	Prandtl number	[-]
			We	Weber number	[-]
ρ	density	[kg.m ⁻³]	AH	absolute humidity	[kg.m ⁻³]
μ	dynamic viscosity	[Pa.s]	Ca	Capillary number	[-]
δ	thickness	[m]	Le	Lewis number	[-]
ϕ	relative humidity	[%]	C	Courant number	[-]
ε	effectiveness	[-]	y	normal distance to heat exchange surface	[m]
ε	dissipation rate	[m ² .s ⁻³]	z	depth of the heat exchanger	[m]
α	thermal diffusivity	[m ² .s ⁻¹]	x	distance between two points	[m]
γ	relaxation factor	[-]	NTU	number of transfer units	[-]
τ	stress tensor	[Pa]	T	temperature	[K]
ψ	scalar	[-]	M	molecular weight	[kg/kmol]
Γ	diffusion coefficient	[m ² .s ⁻¹]	H	enthalpy	[J.kg ⁻¹]
σ	surface tension coefficient	[N.m ⁻¹]	u	velocity	[m.s ⁻¹]
κ	interface curvature	[m ⁻¹]	V	volume	[m ³]
β	liquid fraction	[-]	\dot{V}	volume flux	[m ³ .s ⁻¹]
ω	humidity ratio	[kg.kg ⁻¹]	M	molecular weight	[kg.mol ⁻¹]
<i>Latin symbols</i>			I	identity matrix	[-]
A	surface area	[m ²]	E	energy	[J]
c_p	specific heat capacity	[J.kg ⁻¹ .K ⁻¹]	h	sensible enthalpy	[J]
t	time	[s]	Y	mass fraction	[-]
m''	mass flux	[kg.m ⁻² .s ⁻¹]	B	vector	[-]
d	diameter	[m]	b	boundary condition	[-]
D	diffusion coefficient	[m.s ⁻²]	m	number of boundaries	[-]
p	pressure	[Pa]	f	vector with boundary conditions	[-]
h	heat transfer coefficient	[W.m ⁻² .K ⁻¹]	J	reaction rate	[kg.m ⁻² .s ⁻²]
U	global heat transfer coefficient	[W.m ⁻² .K ⁻¹]	y	thickness	[m]
k	thermal conductivity	[W.m ⁻¹ .K ⁻¹]	c	molar concentration	[mol.m ⁻³]
k	turbulence kinetic energy	[J.kg ⁻¹]	<i>Abbreviations</i>		
N	molar flux	[mol.m ⁻² .s ⁻¹]	ATES	aquifer thermal energy storage	
S_v	energy source term	[J]	LMTD	log mean temperature difference	
S_m	mass source term	[kg.m ⁻² .s ⁻¹]	<i>Subscripts</i>		
S_h	source of energy due to chemical reaction	[J]	h	hot	
G_k	turbulence kinetic energy of velocity	[J]	hyd	hydraulic	
G_b	turbulence kinetic energy of buoyancy	[J]	c	cold	
F	external body force	[N]	b	bulk	
Nu	Nusselt number	[-]	w	water	
P	longitudinal tube pitch	[-]	l	liquid	
L	latent heat	[J.kg ⁻¹]	avg	average	
Pr	Prandtl number	[-]	c	convective	
q	heat flux	[W.m ⁻²]	v	vapour	
\dot{Q}	heat transfer rate	[W]	lm	log-mean	
\dot{m}	mass flow rate	[kg.s ⁻¹]	out	outlet	
Re	Reynolds number	[-]	in	inlet	
Ra	Rayleigh number	[-]	f	frost	
			s	surface	

a	air
in	inlet
out	outlet
min	minimum
max	maximum
ice	ice
wall	wall
x	coordinate
as	air fluid stream
ws	water fluid stream
a,s	saturated air
eff	effective
p	phase
fl	fluid
k	turbulence kinetic energy
ε	dissipation rate
ref	reference
mesh	mesh
sol	solid
D_H	hydraulic diameter
T	thermal
sat	saturated
cell	cell

Abstract

The use of centralised heat supply systems in neighbourhoods is increasing in popularity. Heat is extracted from the ambient air to produce hot water. A problem that can arise when using a heat pump in heating mode is frost formation on the heat exchanger. Frost build-up impedes the airflow and reduces the heat transfer rate. Periodic defrosting is required to prevent a complete shutdown and maximise the air cooler's performance. A better understanding of frost formation could improve the performance. Two models have been developed for an air-to-water counter-current flow heat exchanger based on a different approach. The segmented 1D quasi-steady state mode predicts the dynamic formation of a dense frost layer and condensation by heat and mass balances. The 2D time-dependent model is based on conservation laws for each individual phase and the entire mixture and an enthalpy-porosity formulation for forming a frost layer.

The results of both models are not validated with experimental results. Only the air and water temperature and sensible and latent heat transfer of both models are compared. It is concluded that the amount of condensing water vapour is significantly different due to implementation differences and that the frost layer negatively affects the heat exchanger's performance. Comparison with experimental data is required to identify whether either model can be used to optimise the heat exchanger design with frost formation.

1 Introduction

The use of centralized heat supply systems in neighbourhoods is increasing in popularity. In many places, especially when houses in a neighbourhood are close together, these heat networks are a good and cheap option to make these neighbourhoods natural gas free. Different heat sources are applicable in these systems, like industrial residual heat, thermal energy in the subsurface or ambient air. A combination of thermal energy in the subsurface and ambient air is a promising heat source if no residual heat is available. Both can be combined in a heat pump to produce hot water for houses in the neighbourhood. But ambient air as a source for a heat pump has several disadvantages. In the first place, power and efficiency decrease when the heat demand is greatest: at low outside temperatures. And secondly, the relative humidity around the freezing point is often quite high, causing ice build-up on the evaporator [30]. When the air cooler surface temperature is below the freezing point, and ambient air humidity is higher than saturation humidity, frost forms on the air cooler surface [42]. This ice build-up is initially favourable since it increases the air-side heat transfer coefficient due to reduced resistance and rough frost surface, which acts like small heat fins. But, as frost thickness increases, it impedes the airflow, increases the air-side pressure drop, reduces the heat transfer rate, and degrades the positive factors [13]. The mass flux of the airflow will be decreased, but that is also depending on the characteristics of the applied fan. This can result in a too-low exit temperature, and an undesired increase in the non-homogeneity of the air condition in the refrigerated area [30]. Periodic defrosting is required to prevent a complete shutdown and maximize the air cooler's performance. During defrosting, the heat pump cannot supply heat and even absorbs heat (and electricity) to speed up defrosting [39]. All of this affects efficiency to the extent that it is difficult to predict.

The air cooler is placed parallel to an Aquifer Thermal Energy Storage (ATES) to provide heat during the winter period, which is shown in Figure 1.

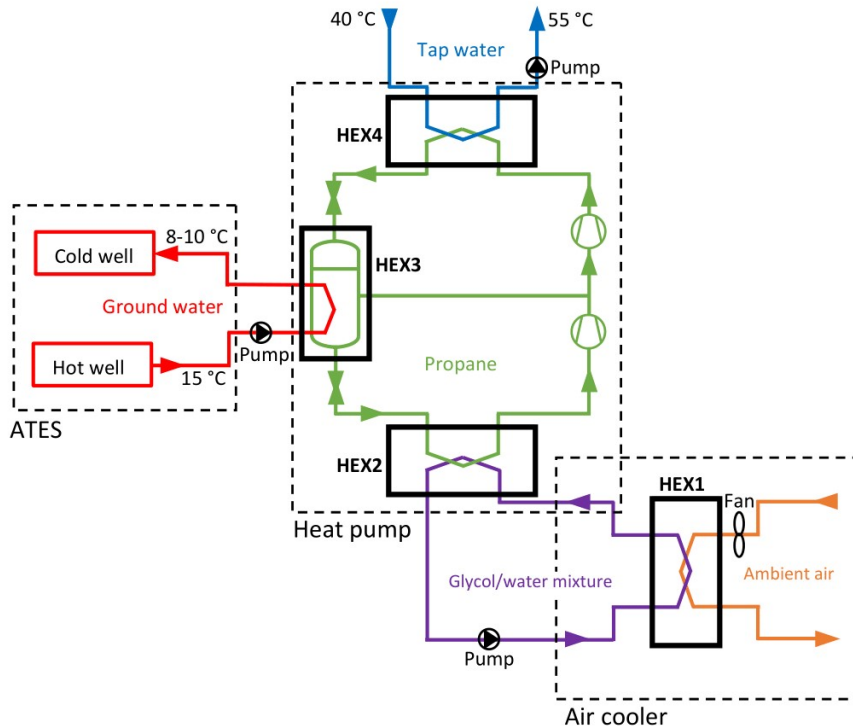


Figure 1: Schematic display of the heat supply system, consisting of a heat pump with two heat sources: ATES & an air cooler. Water with a temperature of 15 °C from the hot well is pumped up and provides heat to HEX3 (evaporator). The cooled groundwater, with a temperature of 8-10 °C, is stored in the cold well of ATES. A water-glycol mixture is the heat source of HEX2 (economizer). This mixture is heated by the air cooler, which extracts heat from the ambient air in the air cooler (HEX1).

ATES consists of two different underground water wells. One of these wells is a hot well with a temperature of 15 °C, shown in red in Figure 1. The other well is the cold well, with an average temperature of 8 – 10 °C. In winter conditions, groundwater will be pumped up from the hot well. This water will be transported to the economizer side of the heat pump, where heat will be extracted and act as a heat source for the heat pump. The cooled groundwater will be stored in the cold well of ATES. Technically it is possible to produce a tap water temperature of 55 °C with only a heat pump and ATES, but this requires large amounts of water from the hot well. This relatively high water demand requires large wells with relatively high investment costs. An air cooler is added to the system to reduce the size of the wells and, therefore, the investment costs. This air cooler is a water-air heat exchanger which extracts heat from the air and heat, thereby creating a water-glycol mixture. By adding glycol to water, the water will not freeze at 0 °C. This heated water-glycol mixture is an extra heat source for the heat pump to evaporate the refrigerant liquid. All evaporated refrigerant will flow upwards through the high-stage compressor to the condenser. The refrigerant will transfer its heat to the water, which is flowing on the other side of the heat exchanger at the condenser. This heated water needs to be at least 55 °C and will be transported to the houses.

When the heat demand is significantly lower, for instance, during the summer period, the extracted heat from ambient air by the air cooler can be used to recharge the hot well. According to the rules of the licensing authorities, the heat that is extracted or added from the groundwater must remain 'in balance' over the seasons. This means that deficits and surpluses (at a later date) have to be compensated. Therefore, ATES is directly coupled to the air cooler (HEX1 in Figure 1). Due to this reason, the ambient air has no direct coupling with the heat pump. The air cooler is a separate device that can be coupled to the heat pump or ATES and heats up water in both circumstances.

Ambient air is used as a heat source in the air cooler. The air is propelled by a fan and transfers heat within the air cooler to the water-glycol mixture. It will certainly reach its dew point when the hot and humid air cools down. At this point, the air consists of its maximum amount of moisture. Further decrease in temperature will lead to condensation of this moisture [39]. Possibly will, the air temperature decreases below 0 °C so that condensation will lead to a frost layer at the fins and tubes of the heat exchanger. Frosting deteriorates the operation and energy efficiency. It reduces the output heating capacity because it reduces the airflow passages area and acts as a thermal insulator, leading to performance degradation or even shutdown [13]. Therefore, in the most favourable situation, the frost layer has a minimal thickness and covers only a tiny part of the heat exchanger.

The aim of this research is to develop a model for the air cooler, in which frost formation will be included, that can be used to study and optimize the design of air coolers operating in frosting conditions.

2 Background

Before explaining the models themselves, some background information about heat exchangers is described. Different types of heat exchangers are widely used. Each of them has its characteristics. Nevertheless, the main purpose of each of them is to exchange heat between fluids. Different types of heat and mass transfer are involved and discussed. Heat and also mass is transferred due to condensing or sublimated water vapour. The most essential characteristics of the formed frost layer are given. Simple heat-exchange models can describe the overall heat transfer itself. The most used methods to determine the performance of the heat exchanger are explained.

2.1 Heat exchange geometries

Heat exchangers are widely used in space heating, refrigeration and air conditioning. Its primary purpose is the transfer of energy between two fluids. Each application requires a different type of heat exchanger. These can be classified into two categories: mixing and non-mixing. Physical mixing of the two fluids occurs in regenerators and open-type heat exchangers. In recuperators, the hot and cold fluid streams have no direct contact but are separated by a tube or surface. The wall's surface area between the two fluids is maximised to maximise efficiency, while the resistance to both fluids flows is minimised [5]. This type of heat exchanger is considered in this research.

The recuperator is classified by the configuration and the number of passes of each fluid through the heat exchanger. Each fluid flows only once through the exchanger in a single-pass heat exchanger. Their flow arrangement can still vary. Both fluids enter the exchanger at the same end and flow in the same direction to the other side in a parallel flow exchanger, while the fluids flow in opposite directions in a counter-flow configuration. These configurations are primarily used in a double-pipe setup, shown in Figure 2. More complex geometries often consist of these basic configurations.

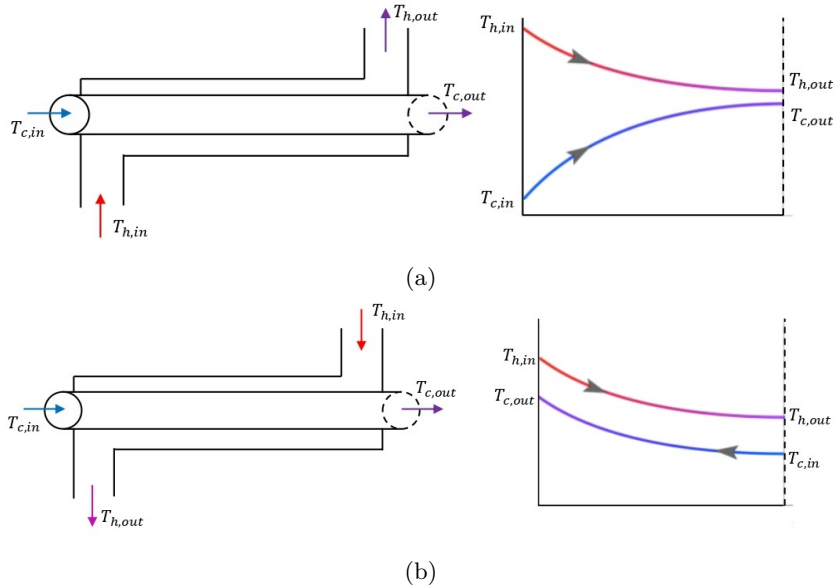


Figure 2: Schematic sketch of a double-pipe heat exchanger in counter- (a) and parallel (b) flow configuration, with the temperature profiles of both fluids over the length of the heat exchanger.

Generally, more heat is transferred within the counter flow configuration, and the temperature difference between two fluids is kept constant. That results in a higher outlet temperature for the cold fluid. The parallel configuration is only beneficial when both outlet temperatures are expected to be the same. The area of the heat exchange surface for both configurations can be increased by increasing the diameter or length of the tube. This makes it impractical to use in some applications. In these applications, the cross-flow configuration is mostly used.

In a cross-flow heat exchanger, fluids flow perpendicularly, with an angle of 90 degrees. An example of such a configuration is the shell and tube exchanger, where one fluid flows in the tube side, and the

other passes perpendicular around the tubes on the shell side. This type of heat exchanger can also be constructed as a counter or parallel flow heat exchanger. The plate-fin heat exchanger is another cross-flow configuration [56], shown in Figure 3. Fins are used to separate the parallel plates, which also helps to increase the heat transfer area. Different shapes of fins, like rectangular, triangular or wavy, are used. The fluids flow through these fins. A tube-fin configuration is mainly used for air coolers in which a fluid and gas exchange heat. Furthermore, fins are used to increase the effective heat exchange surface area. These fins also separate the channels for the airflow to pass over these pipes.

The effectiveness of the cross-flow heat exchanger can be increased by providing a multi-pass for the water flow. In this setup, the water flows through the heat exchanger several times. This also prevents non-uniform outflow temperatures for the water flow.

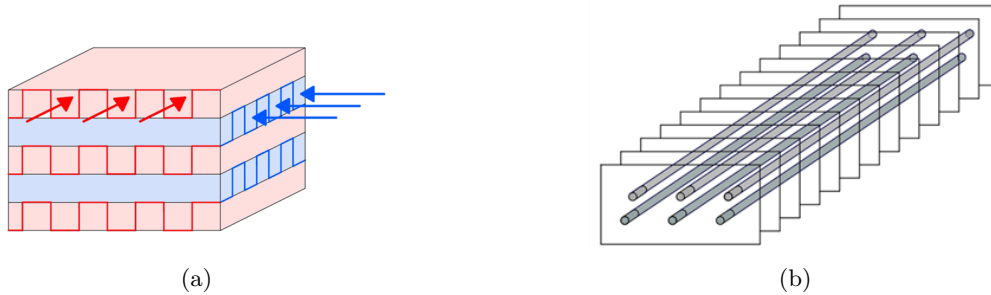


Figure 3: Illustration of two types of cross-flow heat exchangers: plate-fin (a) and finned-tube (b) heat exchanger [47].

2.2 Frost formation

Each heat exchange geometry's surface acts as a heat transfer medium between two fluids. If the surface temperature is beneath zero degrees Celsius and the saturation temperature of the surpassing air is higher than the surface temperature, the formation and growth of a frost layer can occur due to the deposition of water vapour in the air. For frost formation on the fins or tubes, certain preliminary requirements can be formulated concerning the dew point temperature of humid air and the cooling wall temperature [39]. The characteristics of this frost layer, such as the density and thermal conductivity, are important for the performance of the air cooler under frost formation. Furthermore, different phenomena are incorporated during the growth process of a frost layer, like the geometry and dimensions. A strong in-homogeneity usually characterizes frost layers in density and porosity [18]. Ice compositions change along the frost height and position on the wall. For instance, the porosity and growth rate differ over the frost layer. But also, the frost thickness varies with space [57]. The frost growth rate toward the front of the plate is higher than toward the rear, especially at lower airflow rates. For higher air flow rates, the frost growth is uniform over the layer [57] but increases the frost growth rate and creates denser frost layers [31].

The frost layer leads to an increased heat resistance between the heat transfer surface and airflow and a decrease in air flow rate. This degrades the performance of the air cooler [56]. This effect is more significant for higher air temperatures. For increasing air temperatures with a constant humidity ratio, frost thickness and energy transfer resistance decrease continuously, indicating that thinner but denser frost layers are formed with higher air temperatures.

2.2.1 Frost growth

The frost growth is divided into several periods: 1) the crystal growth period, 2) the frost layer growth period, and 3) the frost layer full growth period [16]. Nucleation will form ice crystals in the first stage [39]. This nucleation process requires supersaturated water vapour to overcome the Gibbs energy barrier, and a surface below the freezing temperature [15]. Even after this stage, if a thin frost layer is formed, the water vapour has to be supersaturated for frost growth. The change in Gibbs energy of the water vapour occurs through a pressure or temperature change [35]. The Gibbs energy is the highest close to the surface, and frost nucleation will only occur on the cold surface.

Initially, the ice crystals are formed relatively far from each other and grow in the vertical direction. They will interconnect when more crystals are formed [16]. From that point, the second period starts. The ice crystals begin to grow due to the transport of water vapour molecules from the airflow to the surface [39]. This results in a porous frost layer, shown in figure (e) of Figure 4. Ice crystals have a hexagonal shape. At these corners, the gradient of partial vapour pressure is the greatest. This results in a higher attraction of water vapour molecules at these places. Volumetric diffusion within the frost layer will not transport these molecules fast enough. Growth, preferably at the corners, will be the result [39]. If the frost layer becomes denser, when the neighbouring ice crystals influence each other, the growth rate decreases [16].

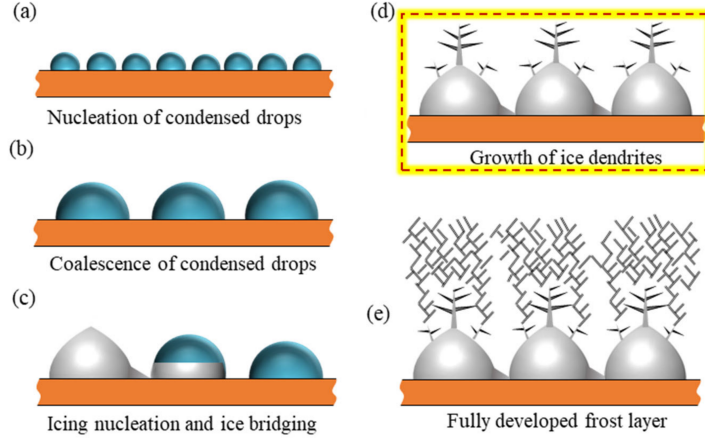


Figure 4: A schematic representation of the frost layer growth process. The nucleation/crystal growth period is represented by figures (a)-(c), and the frost layer growth period is by figures (d) & (e) [19].

At a certain point, the frost layer has grown enough such that the temperature of the frost layer surface exceeds the freezing point. That is the beginning of the frost layer's full growth period. Liquid water forms on this surface and flows into the frost layer. Refreezing results in the densification of the frost layer, which is known as permeation [49]. This process continues as long as the frost layer acts as a porous medium into which the diffusion of water vapour results in an increase of thickness and/or density [17]. A schematic representation of these mass fluxes is shown in 5. As a result of the frost formation, heat is released in the form of latent heat.

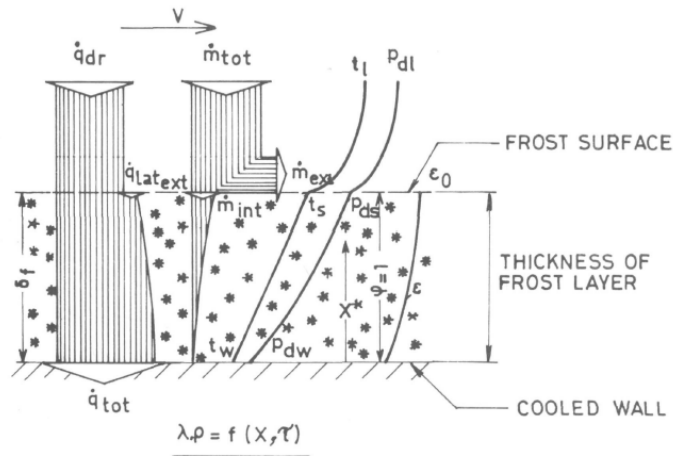


Figure 5: A schematic representation of the frost layer with mass and heat fluxes. The total mass flux \dot{m}_{tot} to the frost layer is sub-divided into a diffusing mass flux \dot{m}_{int} for densification of the frost layer, and a mass flux that contributes to the growth of the frost thickness \dot{m}_{int} . This mass flux increases the frost thickness δ_f [39].

2.2.2 Density

The density of the frost layers differs over time and place. In the initial stage of frost formation, a significant number of small ice crystals may be observed at the heat transfer surface [39]. The formed layer has a higher density than a thicker frost layer. Thicker frost layers have an unequal density depending on the distance to the heat transfer surface. This depends on the growth mechanisms and internal diffusion of water vapour from the frosted surface to the heat transfer surface. Next to the stage of frost formation are other factors that influence the frost density, such as air velocity, surface temperature, air temperature, and humidity [56]. Commonly, the frost density increases with an increased air velocity due to variation in the air-side heat transfer coefficient [57]. The density increase is more significant at higher surface temperatures and dew point temperatures. The density also increases for higher frost growth rates [39]. All these influencing parameters make it difficult to find a correct correlation for the average frost density. Simplifications can be made if the nucleation and crystal growth period are not included [27]. During these stages, the frost density is considerably lower than the frost density during frost growth ($\approx 30 \text{ kgm}^{-3}$) [22]. This constant frost density is applied to the model for frost thickness below 0.1 mm. For larger values, the frost density is a function of the heat exchange surface temperature (T_s). The frost density can be calculated with the following equation:

$$\rho_f = \begin{cases} 30 & \text{if } T_s < 255.85 \text{ K} \\ 13.61 \cdot T_s - 1345 & \text{if } 255.85 \text{ K} < T_s < 273.15 \text{ K} \end{cases} \quad (1)$$

For surface temperatures below 255.85 K, is the frost density equal to the frost density during the nucleation phase.

2.2.3 Effective thermal conductivity

Thermal conductivity is a material constant that indicates how well the material conducts heat. The effective thermal conductivity gives the mean value. The thermal conductivity of frost depends on several parameters, which makes it almost impossible to define an accurate mean value for modelling purposes. First, the temperature at which frost crystals form influences the type of crystalline formation and directly affects the thermal conductivity [38]. Secondly, the density affects thermal conductivity, but two frost layers with identical densities might still have different thermal conductivity. This difference results from the shape and orientation of the ice crystals within the frost layer structure. If the crystals are oriented in parallel planes to the direction of the heat flow, the frost layer would have its highest thermal conductivity. However, for the same given density, a relatively low thermal conductivity would occur if the ice crystals oriented themselves in planes perpendicular to the direction of the heat flow [38]. Also, the air velocity influences the thermal conductivity of the frost layer for a similar value for the frost density [16]. The thermal conductivity increases due to a decrease in frost growth rate [57]. Furthermore, the thermal conductivity is affected by the stage at which the frost grows. Separate correlations have been used at the frost layer's early and full growth stages. The thermal conductivity is low in the early stages and increases as time passes [39].

Although the variety of influencing parameters is assumed, the thermal conductivity can be expressed as a function of the density [3]. The following expression is applicable during the frost layer growth period and is applicable for flat plate parallel and counter-flow heat exchangers.

$$k_f = 0.132 + 3.13 \times 10^{-4} \rho_f + 1.6 \times 10^{-7} \rho_f \quad (2)$$

2.2.4 Specific heat capacity

The specific heat capacity of frost is a value for the required heat to increase the temperature of a certain mass amount. For frost, this only varies due to differences in density [18]. The average specific heat capacity of frost is given in the following equation:

$$c_{p,f}^{eff} = 0.001202 \rho_f^{0.963} \quad (3)$$

This expression can be used for a frost layer with porosity and strong homogeneity. The equation can be applied to plate-fin and shell tube heat exchangers.

2.3 Heat & mass transfer

The air cooler transfers heat from the in-flowing ambient air to the water-glycol mixture in a counter-flowing direction, shown by Figure 2. These fluids also transfer heat due to mass transfer within their flow domain. Different modes of heat transfer are involved in this process. Each of these modes is described, and corresponding fundamental equations for the rate of energy transfer are given in the following subsections. It is assumed that radiation is negligible. This mode of heat transfer is not explained.

2.3.1 Convection

Convection is the heat transfer between a surface and an adjacent fluid or due to heterogeneity and body forces on a fluid. A distinction can be made between forced convection, in which the fluid is forced to flow by an external force from a fan or pump, and free convection, wherein the temperature difference within is fluid causes circulation. Within the air cooler, both types of convection are present. Both fluids are forced to flow by a pump or fan, and there is also a temperature gradient within each fluid. The rate of heat transfer is given by the Newton rate equation [54]:

$$q = h\Delta T \quad (4)$$

The convective heat transfer coefficient is dependent on the type of convection and geometry. This coefficient can be calculated with the expressions for the Nusselt number, given in Section 2.3.3.

2.3.2 Conduction

Conduction is the heat transfer within and through a material itself. The heat is transferred from the hotter to the colder side of the material by molecular interaction. The molecule with a greater motion, at a higher energy level, transfers its energy to adjacent molecules at a lower energy level. The heat transfer rate per area is proportional to the negative temperature gradient. Fourier's law gives a general relation for this heat flux:

$$q = -k\nabla T \quad (5)$$

The thermal conductivity is assumed to be independent of the direction, which makes it only applicable to isotropic mediums. It is a material property that is primarily a function of temperature or density (in case of a varying density). Generally, gasses have a low thermal conductivity, while solids have a relatively higher one.

2.3.3 Nusselt number

A key dimensionless variable for the ratio between convective and conductive heat transfer is given by the Nusselt number, which is defined as:

$$Nu = \frac{\text{Convective heat transfer}}{\text{Conductive heat transfer}} = \frac{hx}{k} \quad (6)$$

The characteristic length should be chosen in the direction of the boundary layer, for instance, the outer diameter of a cylinder.

The Nusselt number is often expressed as a function of other dimensionless variables. Its expression is dependent on the geometry of the flow domain. For a counter- and parallel heat exchanger, the fluid can flow over a flat plate or within a pipe flow. The average Nusselt number for a laminar flow over a flat plate, from the inlet edge to a downstream distance x is given by [20]:

$$\overline{Nu}_x = 2 \cdot 0.332 Re_x^{1/2} Pr^{1/3} = 0.664 Re_x^{1/2} Pr^{1/3}, (Pr > 0.6) \quad (7)$$

For fluids flowing in a laminar regime within a pipe flow, the following correlation for the Nusselt number can be used:

$$Nu = \frac{hd_{hyd}}{k} \quad (8)$$

These correlations do not apply to cross-flow heat exchangers since they have different geometry. The air side of the heat exchanger flows through finned tube bundles with smooth rectangular fins and circular

tubes. The Nusselt correlation for this air side is given by [24]:

$$\text{Nu}(d_{ae}) = C_1 \text{Re}(d_{ae})^{0.625} \text{Pr}^{\frac{1}{3}} \left(\frac{d_{ae}}{P_1} \right)^{\frac{1}{3}} \quad (9)$$

where C_1 is a constant that depends on the specific tube setup (e.g. the number of rows), d_{ae} is the characteristic length of a single flow channel, and P_1 is the longitudinal tube pitch.

A different correlation can describe the water flow within the tubes for the Nusselt number. The expression for the Nusselt number for the entrance region of a laminar tube flow is given by the Sieder-Tate correlation [9]:

$$\text{Nu} = 1.86 \left(\frac{\text{Re Pr } d}{L} \right)^{\frac{1}{3}} \left(\frac{\mu_b}{\mu_w} \right)^{0.14} \quad (10)$$

where μ_b is the fluid viscosity at the bulk water temperature and μ_w is the fluid viscosity at the heat-transfer boundary surface temperature.

2.3.4 Condensation

Condensation of water vapour upon a cold surface involves the simultaneous transfer of heat and mass. A film of the condensed liquid is formed on a cold surface which separates the surface from the air-flow through which the condensate is transferred by molecular diffusion [54]. The molar flux can be derived from the general differential equation for mass transfer in the gas phase, which states that the molar flux normal to the heat exchange surface is constant:

$$\frac{d}{dz} N = 0 \quad (11)$$

The molar flux, for a small temperature gradient between the gas film and the condensed liquid, can be expressed as:

$$N = \frac{(cD_{AB})_{\text{avg}}(y_{A1} - y_{A2})}{(z_2 - z_1)y_{B,lm}} \quad (12)$$

in which D_{AB} is the diffusion coefficient of water vapour diffusing through the air, c the molar concentration, $y_{B,lm}$ log-mean mole fraction of air, and z and y_A respectively the normal distance and mole fraction. z_1 is located within the film of gas and z_2 at the surface of the condensate liquid film.

This mass transfer also involves a corresponding heat transfer. The heat-transfer coefficient for the natural convection of air with a relatively low amount of diffusion vapour content can be estimated by the Churchill and Chu correlation [10]:

$$\text{Nu}_L = 0.68 + \frac{0.670 \text{Ra}_L^{1/4}}{[1 + (0.492/\text{Pr})^{9/16}]^{4/9}} \quad (13)$$

The total energy flux through the liquid surface also passes through the liquid film. This can be expressed by:

$$\frac{q_z}{A} = h_{\text{liquid}}(T_2 - T_3) = h_c(T_1 - T_2) + N_{A,z}M_A(H_1 - H_2) \quad (14)$$

where h_{liquid} is the convective heat-transfer coefficient in the liquid film, h_c is the natural convective heat-transfer coefficient in the gas film, M_A is the molecular weight of water vapour, and H_1 and H_2 are respectively the enthalpies of the vapour at the gas film and at the surface of the condensate liquid film. The temperature at the condensing surface is given by T_3 .

2.4 Simple-heat exchange model

The total heat transfer of phenomena that are described within Section 2.3 can be expressed with simple-heat exchange models. The log-mean temperature difference can describe the heat exchange rate of every single-pass flow arrangement (LMTD) [54] for simple-heat exchange geometries, presented in Figure 2. The LMTD can be determined based on the variables shown in this figure. A single equation can describe the total heat transfer:

$$\dot{Q} = UA\Delta T_{LMTD} \quad (15)$$

in which A is the area of the entire heat transfer area, U is the global heat transfer coefficient, and ΔT_{LMTD} is the log mean temperature difference. This is the mean temperature difference between two fluid flows, which drives the heat exchange. The expression for this driving force is given by:

$$\Delta T_{LMTD} = \frac{(T_{h, out} - T_{c, out}) - (T_{h, in} - T_{c, in})}{\ln \left[\frac{T_{h, out} - T_{c, out}}{T_{h, in} - T_{c, in}} \right]} \quad (16)$$

For both counter and parallel flow configurations, the LMTD method can be applied. Other flow configurations, like a shell- and tube or cross-flow heat exchanger, are more difficult to approach analytically. Correction factors are used within Eq. 15 [7].

The global heat transfer coefficient of Eq. 15 combines the heat transfer coefficients for the hot and cold fluid and the wall separating both fluids. These coefficients can be determined by Eq 6. The LMTD method is based upon a constant value for this coefficient. In practice, this coefficient will not remain constant. A value of U taken midway through both ends of the heat exchanger is usually accurate enough [54]. The mean value for the heat transfer coefficient can be expressed as:

$$U_t A = \frac{1}{\frac{1}{h_a A} + \frac{x_{wall}}{2k_1 A} + \frac{1}{h_w A}} \quad (17)$$

In case not all inlet and outlet temperatures are known, the effectiveness equation can be used [36]. This defines the ratio between the actual heat transfer and maximum possible heat transfer in a heat exchanger geometry. The expression for the effectiveness is given by:

$$\varepsilon = \frac{\dot{Q}}{\dot{Q}_{max}} = \frac{\dot{m}_h c_{p,h} (T_{h,in} - T_{h,out})}{(\dot{m}c_p)_{min} (T_{h,in} - T_{c,in})} = \frac{\dot{m}_c c_{p,c} (T_{c, out} - T_{c,in})}{(\dot{m}c_p)_{min} (T_{h,in} - T_{c,in})} \quad (18)$$

in which $(\dot{m}c_p)_{min}$ is the minimum value of $\dot{m}_h c_{p,h}$ and $\dot{m}_c c_{p,c}$.

The effectiveness can also be computed from the number of transfer units (NTU) and the ratio between capacity ratios of both fluid streams. The performances of a heat exchanger can be readily evaluated if the number of transfer units is known [59]. This ratio can be expressed as:

$$NTU = \frac{UA}{(\dot{m}C_p)_{min}} \quad (19)$$

The effectivity can be derived from graphs or expressions matching the number of transfer units to the effectiveness. Each heat exchanger geometry has its own correlations and graphs [25]. The effectiveness of a counter-current flow heat exchanger can be calculated with:

$$\varepsilon = \frac{1 - \exp[-NTU(1 - C_r)]}{1 - C_r \exp[-NTU(1 - C_r)]} \quad (20)$$

with the heat capacity ratio $C_r = (\dot{m}C_p)_{min} / (\dot{m}C_p)_{max}$. In a situation in which a phase change (condensation or evaporation) is occurring in one of the heat exchanger fluids. The effectiveness is independent of the flow arrangement and is given by:

$$\varepsilon = 1 - e^{-NTU} \quad (21)$$

Methods described within this section are coupled to each other by Eq. 18. Small deviations can arise due to mesh convergence errors. Nevertheless, these methods are relatively fast and simple calculations for a heat exchanger and give an indication of the rate of heat exchange.

3 Model description

This research focuses on presenting a numerical model for an air cooler in both winter and summer conditions. An adequate frost growth model is one of the components of the air cooler model in frost conditions. A mathematical formulation based on energy and mass balance equations that govern the frost layer with latent heat transfer effects describes this process in these models.

In the following chapter are several models described for different geometries. The MATLAB model can be applied to a 1D counter-flow, shown in Figure 2 and a 2D cross-flow heat exchanger. Another 2D counter-flow model has been computed in ANSYS. This model is used to validate the MATLAB counter-flow model due to the lack of experimental data for this geometry.

3.1 MATLAB model

This mathematical model has been deployed to predict condensation and frost formation behaviour on the heat transfer surface of two different geometries, a counter-flow and cross-flow geometry. The model concerns the dynamic formation of frost and condensation. Therefore, both heat and mass transfer has to be incorporated. The freezing process on the heat exchange surface simultaneously involved heat and mass transfer.

The following assumptions have been made in the development of the model:

- The freezing process can be considered to be a quasi-steady-state process. Thus in a time step, the air-flow is stable, and the properties of air and the frost are constants.
- Since the heat resistances of the fins and tube is much lower than the heat resistances of the frost layer and the air-flow, the thermal conductivity of the fins and tube are neglected [39].
- The radiation between the heat transfer surface and the air is negligible. Only convection and conduction are incorporated into this model [57].
- Constant density of air and water for the entire heat exchanger is assumed.
- Constant inlet velocity of air and water is assumed. This means that the resulting mass flows depend only on the cross-flow area.
- Constant heat transfer coefficients are assumed.
- Constant value for the latent heat of evaporation. The released energy from condensation is a function of the air temperature, but in this model, the latent heat is assumed to be constant.
- Air properties within the heat exchanger are calculated based upon a constant pressure equal to the atmospheric pressure.
- Variable variation of air humidity and temperature of the surface, air and water within the element is neglected.
- One-dimensional mass transport and heat transfer are assumed. This means that frost only grows in the direction normal to the cold surface [57].
- Simulation of the frost growth starts from a thin layer. Hence, nucleation and crystal growth are not included in the model [27].

The model employs one-dimensional heat and mass transfer based on a local average value within each element. The entire counter-flow heat exchanger is divided into different sections. The heat and mass transfer from moisture air to a water-glycol mixture is averaged in these sections and calculated on each boundary. Within each section is the heat balance solved, in which sensible heat from the moist air stream is transferred to the frost layer. This frost layer build-up near the wall in the air-fluid domain is governed by condensation and de-sublimation of water vapour while releasing latent heat. The sensible and latent heat is mainly transferred to the water fluid stream, which is flowing in the opposite direction. This is the system definition of the counter-current heat exchanger governed by the 1D model.

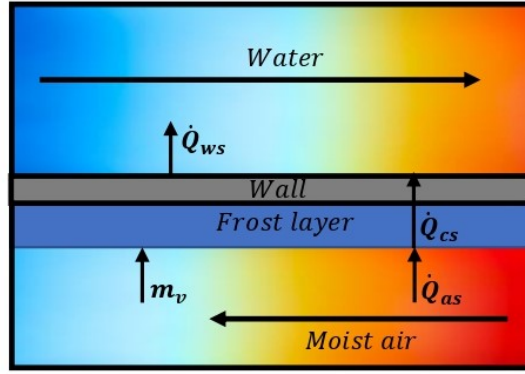


Figure 6: The system definition of the counter-current heat exchanger. Moist air releases sensible heat (\dot{Q}_{as}) by a temperature decrease that is transferred to the frost layer by the wall together with a condensation/deposition mass flux (m_v). These heat fluxes are equal to the heat supply rate on the waterside (\dot{Q}_{ws}). This heat supply will heat the counter-flowing water on the other side of the wall.

3.1.1 Condensation

Air flowing through the air cooler transfers heat to the fins to increase the temperature of the water-glycol mixture. This leads to a decreasing air temperature and possibly condensation. Colder air can contain less water vapour and becomes saturated with water vapour at a certain temperature. The temperature at which the air is saturated with water vapour is the dew point temperature [39]. At this temperature, the excess water vapour can condense. The higher the initial humidity level, the closer the dew point is to the temperature of the air. The air is already almost saturated at higher humidity and only needs to be cooled slightly to condense.

The air humidity can increase above its saturation level due to a decreased air temperature beneath its dew point. Since the parameters are non-varying within each section, the saturation level is only calculated on each boundary. Figure 7 shows a schematic representation of the heat exchanger's division into different sections.

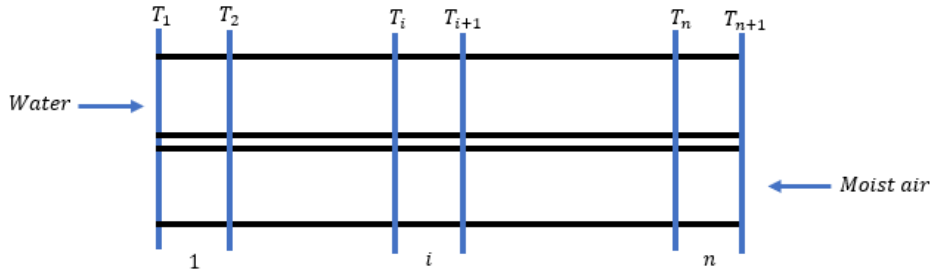


Figure 7: The subdivision of the heat exchanger in n sections (shown at the bottom). The water flows into the heat exchanger from the left to right side. On the bottom side of the wall is moisture air flowing in the opposite direction. The matrix implementation can calculate temperatures and air moisture content at all $n + 1$ boundaries.

The saturation level, expressed as the relative humidity within the model, of the boundary upstream $i + 1$ and the temperature decline over the section determines the saturation level of the following boundary i . If the relative humidity increases above 100% at this boundary, a certain amount of water vapour should condense between both boundaries to remain at 100%. The amount of water vapour per unit area that has to condense to stay at a relative humidity of 100% is expressed by Eq. 22.

$$m''_{v,i} = \frac{\frac{0.0132e^{\frac{17.67(T_{a,i+1}-273.15)}{(T_{a,i+1}-38.65)}}}{T_{a,i+1}}\phi_{i+1} - \frac{0.0132e^{\frac{17.67(T_{a,i}-273.15)}{(T_{a,i}-38.65)}}}{T_{a,i}}\phi_i}{A} \quad (22)$$

The air humidity can also increase above saturation level due to contact with a surface at a temperature beneath the dew point [43]. The resulting mass flux can be calculated by the difference of the air-fluid stream humidity ratio compared to the humidity ratio of the heat exchange surface, expressed by Eq. 23.

$$m_v'' = U_m(\omega_a - \omega_s) \quad (23)$$

The derivation of both mass transfer functions is described in Appendix A.

Since the heat exchanger is modelled with a one-dimensional domain, both conditions are incorporated in all cells of the moist air domain. These cells contain a flow, which can decrease beneath its dew point due to a decreasing air temperature, and have contact with a heat exchange surface, which can have a temperature beneath the dew point. The maximum value of either equation, Eqs. 22 and 23, is used as the corresponding condensation mass flux.

The energy stored in this mass flow can be expressed by incorporating the latent heat of this mass transfer. Latent heat is energy in a hidden form which is supplied or extracted to change the state of a substance without changing its temperature [53]. In this model, the latent heat has three different values. The mass flux and latent heat equal zero if the relative humidity is beneath the saturation level. In wet conditions, the latent heat has two values depending on the temperature of the heat exchange surface (T_s). If this temperature is below the freezing point, deposition creates a frost layer. Otherwise, the moisture content will only condense. This can mathematically be expressed as [52]:

$$L = \begin{cases} 0 & \text{if } \phi_{a,s} > \phi_a \\ 2260e3 & \text{if } \phi_{a,s} \leq \phi_a \text{ and } T_s > 273.15 \text{ K} \\ 2594e3 & \text{if } \phi_{a,s} \leq \phi_a \text{ and } T_s < 273.15 \text{ K} \end{cases} \quad (24)$$

3.1.2 Frost growth

The mass flux of condensation, given by Eqs. 22 and 23, represents the amount of water vapour condenses. If the surface temperature is below the freezing point of 273.15 K, the condensed water vapour will form a frost layer on the heat exchange surface. When the air cooler surface temperature is below the freezing point, and ambient air humidity is higher than saturation humidity, frost forms on the air cooler surface.

The simulation of the frost growth starts from a thin layer of $2 * 10^{-5}$ m. The frost density for a frost thickness larger than 0.1 mm is expressed by Eq. 1. The frost thickness can be calculated, with the frost density and the mass flux per unit area, due to the quasi-steady state assumption and the assumption that the mass transport and heat transfer are only one-dimensional. A schematic representation of the frost layer with its properties is shown in Figure 8

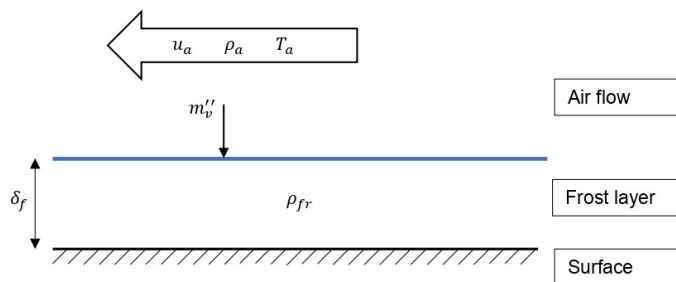


Figure 8: A schematic representation of the frost layer, with a thickness δ_f , density ρ_{fr} and condensation mass flux m_v'' from the air-flow. The density is constant over the entire frost layer. All parameters are also constant within each time step due to the quasi-steady state assumption.

Due to the quasi-steady state assumption, the thickness and density of the frost layer are kept constant within each time step. At the end of the time step, these parameters are updated based on the condensing mass flux and surface temperature. The increase of the thickness after the time step can be calculated

with the following equation [56]:

$$\delta_f = \frac{m''_{v,i} \Delta t}{\rho_{fr} A} \quad (25)$$

After this time step, all the values can be recalculated for a different free stream area of the flowing air. The height of the free stream is decreased with the frost layer thickness. By repeating this process for each time step, the effect of the frost layer can be shown.

The growth of this frost layer affects the mass flow rate of air. Water vapour is, due to deposition, transferred to the frost layer. This mass amount is extracted from the air-flow, increasing the frost layer thickness. The resulting mass flow rate of air at the boundary downstream (i) can be computed with the mass flow rate of air at the boundary upstream ($i - 1$) and the deposition mass flux rate:

$$\dot{m}_{a,i} = \dot{m}_{a,i-1} - m''_{v,i} A \quad (26)$$

3.1.3 Heat transfer coefficient

The air- and water flow are separated by a wall where conductive heat is transferred. The heat exchange rate depends on the temperatures of both fluids and the heat resistance of the wall and frost layer. The heat resistance of the wall depends on the thickness and material. Each material has a thermal conductivity that indicates how well the material conducts heat. This value is a constant material property.

The frost layer on the air side of the wall has a variable thermal conductivity, which depends on the crystalline formation, air velocity, stage at which the frost is growing and surface roughness. The governing relation for thermal conductivity is given by Eq. 2, based on the frost density. The function for the density is expressed in Eq. 1.

The overall heat transfer coefficient can express the insulating effect of the combined wall and frost layer. The combined layer is constructed of two materials, as shown in Figure 9.

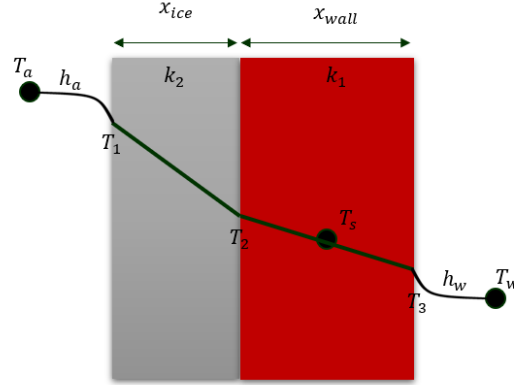


Figure 9: Steady-state heat transfer through a wall with two materials (solid wall & frost layer)

The heat flux through both walls can be expressed with the unidirectional Fourier and Newton rate equation [54]. The relations for the convective and conductive heat flux, given in Eqs. 4 and 5, can be used to provide a relation for the overall heat flux q_x :

$$q_x = h_a A (T_a - T_1) = \frac{k_2 A}{x_{ice}} (T_1 - T_2) = \frac{k_1 A}{x_{wall}/2} (T_2 - T_s) = \frac{k_1 A}{x_{wall}/2} (T_s - T_3) = h_w A (T_3 - T_w) \quad (27)$$

The global heat transfer between the air temperature (T_a) and surface temperature (T_s) can be expressed by Eq. 28. The frost thickness and density influence this value. Each time step, the frost thickness x_{ice} is updated. This also affects the global heat transfer coefficient. Thus, this needs to be updated at each time step.

$$U_a \equiv \frac{1}{\left(\frac{1}{h_a A} + \frac{x_{ice}}{k_2 A} + \frac{x_{wall}}{2k_1 A} \right)} = \frac{q_x}{A (T_a - T_s)} \quad (28)$$

The overall heat transfer between the surface temperature (T_a) and surface temperature (T_s) can be expressed as:

$$U_w \equiv \frac{1}{\left(\frac{1}{h_w A} + \frac{x_{wall}}{2k_1 A}\right)} = \frac{q_x}{A(T_s - T_w)} \quad (29)$$

3.1.4 Model description - Counter flow

The absolute air humidity will not remain constant during wet conditions. The decrease in air temperature or contact with a surface at a temperature beneath the dew point results in an increase of air humidity above its saturation level. This results in a condensation or deposition mass flux to the heat exchange surface. Next to the heat transfer equations, the mass transfer equations must include these condensation or deposition mass fluxes.

The air humidity and the condensation/deposition mass flux have to be incorporated next to the temperatures and the heat fluxes. This is shown for the entire water-air heat exchanger with a frost layer formation in Figure 6. A more detailed system definition for an individual section, shown in Figure 7, is given below. The heat exchange relations of the model are solved for every section.

massa balans toevoegen

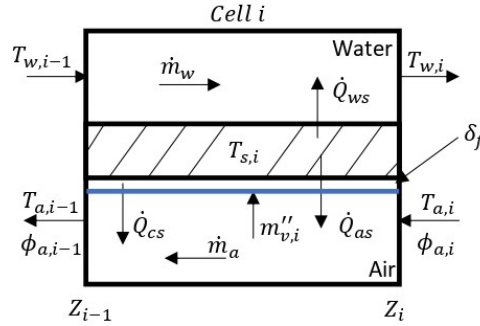


Figure 10: A sketch of the heat transfer of section i of the water-air heat exchanger with the formation of a frost layer with thickness δ_{fr} . The energy from the temperature decrease at the air side (\dot{Q}_{as}) and the latent heat (\dot{Q}_{cs}) of the condensation/deposition mass flux (m''_v) is transferred to the wall. The mass flux and change in air temperature results in a non-constant relative humidity (ϕ). These heat fluxes are equal to the heat supply rate on the waterside (\dot{Q}_{ws}). This heat supply will heat the counter-flowing water on the other side of the wall.

Mass is conserved within the heat exchanger. The law of conservation of mass states that mass is conserved over time, the mass within the fluid flow cannot change:

$$\frac{\partial \rho}{\partial t} + \nabla \cdot (\rho \vec{u}) = S_m \quad (30)$$

For quasi-steady conditions can be assumed that the mass (flux) of both fluid streams is not changed within each time step, resulting in the following law of conservation:

$$\nabla \cdot \vec{u} = 0 \quad (31)$$

This holds for the water fluid stream and also for changes over time. All mass flowing into the heat exchanger also flows out over time. Within the air-fluid stream, water vapour can de-sublimate and form a frost layer on the heat exchange surface. This mass amount is extracted from the air-flow, resulting in a change in mass flux at the in and outflow boundary. The following equation can express the difference:

$$\Delta \dot{m}_a = \sum_{i=1}^n m''_{v,i} A_i \quad (32)$$

Within the time step, the mass flow rate of the air-fluid stream is kept constant. After the time step, the new mass flow rate can be calculated with Eq. 26.

The heat equations can be derived from the general energy transport equation [54]. This equation incorporates the diffusion and conduction heat transfer and its influence on the temperature in spatial directions.

$$\rho c_p \left(\frac{\delta T}{\delta t} + \underline{u} \cdot \nabla T \right) = \alpha \nabla^2 T + S_v \quad (33)$$

For quasi-steady conditions can be assumed that the temperature is steady within each time step. Time-dependent variables equal zero, so $\frac{\delta T}{\delta t} = 0$. Furthermore, the quasi-steady assumption states that diffusion is equal to the conduction of the heat source. Both describe the transfer of internal energy. The diffusion term $\alpha \nabla^2 T$ can be removed from the equation [6]. This simplifies the general energy transport equation for quasi-steady-state simulation to the following expression:

$$\rho c_p (\underline{u} \cdot \nabla T) = S_v \quad (34)$$

The latent and sensible heat from the air domain heats the water fluid through the wall that separates both domains. For a single section, the heat source, represented by S_v in Eq. 34, can be expressed by the following figure:

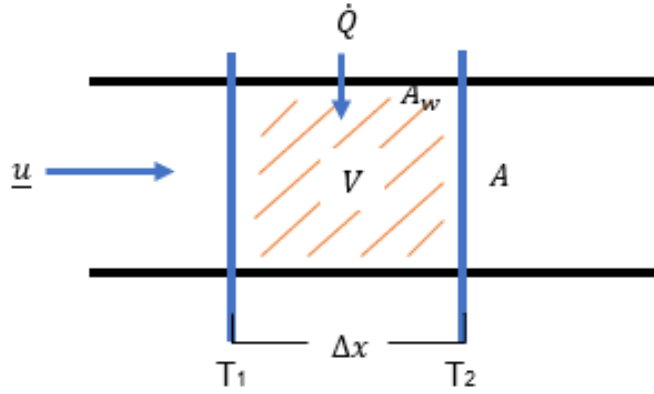


Figure 11: A sketch of the heat exchange on one side of the heat exchanger. The flowing medium is flowing with velocity \underline{u} and is heated by a heat source with energy rate \dot{Q} between the two boundaries (shown with blue lines). The heat exchange area equals A_w , and the heated volume (2D) equals $\Delta x * A = V$. Due to this heat supply will, the temperature increase from T_1 at the left boundary to T_2 on the right boundary of the heat exchanger section. This is shown in the general energy transport equation as ∇T .

The heat supply rate through the wall, shown as \dot{Q} in Figure 11, can be expressed with Fourier's Law [29], given by Eq. 5. This conductive heat flux is transferred to the flowing fluid with a convective heat flux, expressed by the Newton rate equation 4. Applying this law to the situation presented in Figure 11, results in the following expression for the heat source:

$$\dot{Q} = S_v \cdot V = \rho \underline{u} A c_p (T_2 - T_1) = \dot{m} c_p (T_2 - T_1) \quad (35)$$

If \dot{Q} is positive, there is a heat supply. The heat supply rate to the water fluid stream, shown as \dot{Q}_{ws} in Figure 10, can be expressed with Fourier's Law. Fourier's law can be applied to a homogeneous material, like the solid wall between the air and water flow, and a 1-D heat flow, as described in Section 2.3. For the waterside, can the heat supply rate be expressed as:

$$\dot{Q}_{ws} = \alpha_w A (T_s - T_w) \quad (36)$$

This heat supply rate changes the temperature of the water fluid stream. According to the system definition shown in Figure 10, the water flow flows from boundary $i - 1$ to i . Substituting the heat supply rate of Eq. 36 into the expression for the heat source (Eq. 35) results in an expression for the heat balance of the water fluid stream within section i of Figure 10:

$$\dot{m}_w c_{p,w} (T_{w,i} - T_{w,i-1}) = \alpha_w A (T_{s,i} - T_{w,i}) \quad (37)$$

The heat supply rate in the air-fluid domain consists of a combination of latent (\dot{Q}_{cs}) and sensible heat (\dot{Q}_{as}), shown in Figure 10. The latent heat represents the heat the condensation/de-sublimation phase

change releases. The condensation mass flux, described by Eq. 22 and 23 represents the amount of water vapour condenses per unit area. The latent heat rate of this phase change can be calculated by multiplying the condensation mass flux by the latent heat constant, given by Eq. 88 and the heat exchange area, shown as A_w in Figure 11. The sensible heat supply rate can be expressed with Fourier's law. The following equation gives a combination of both heat supply rates:

$$\dot{Q}_{as} + \dot{Q}_{cs} = \alpha_a A (T_a - T_s) + m''_{v,t} AL \quad (38)$$

The relative humidity and temperature of the air-fluid stream determine the heat supply rate. The relative humidity depends on the temperature and saturation level of the air-fluid stream, which is explained in Appendix A. This air fluid stream flows from boundary i to $i - 1$, according to the system definition shown in Figure 10. Substituting the heat supply rate of Eq. 38 into the expression for the heat source (Eq. 35) results in an expression for the heat balance of the air-fluid stream within section i of Figure 10:

$$\dot{m}_a c_{p,a} (T_{a,i} - T_{a,i-1}) + m''_{v,i} AL = \alpha_w A (T_{a,i} - T_{s,i}) \quad (39)$$

As shown in Figure 10, the heat flux from the air side is in balance with the heat flux to the waterside. The heat balance for the surface is presented by:

$$(\dot{Q}_{ws} + \dot{Q}_{cs} + \dot{Q}_{as}) = 0 \quad (40)$$

The general expression for the heat source, given by Eq. 35, can be applied to the heat supply rates of both domains, given by Eq. 36 and 38 for respectively the water and air domain. Substituting both equations into the heat balance of the surface, given by Eq. 40, results in the energy balance of the heat exchange surface:

$$\alpha_a A (T_{a,i} - T_{s,i}) + m''_{v,i} AL = \alpha_w A (T_{s,i} - T_{w,i}) \quad (41)$$

The energy balances of section i for both fluid domains and heat exchange surface, given by Eq. 39, 39 and 41 for respectively the air and water fluid and heat exchange surface, are used to compute the temperature and relative humidity at both boundaries. These expressions for the heat balance in each section can be used for an energy balance in the entire system. Each cell needs to have an equation for the heat balance on the air and waterside, and an equation for the relative humidity. The algorithm for solving these expressions is explained within Section 3.1.6.

The value for the relative humidity at each boundary within the air-fluid domain is used to calculate the condensation/deposition mass flux with Eq. 22 and 23. But the relative humidity change also depends on the condensation /deposition mass flux. This is called mutual dependence.

If the condensation/deposition mass flux equals zero, only heat is transferred between both domains. In that case, the absolute air humidity remains constant. Furthermore, it is also possible to apply these heat balances for a heat exchanger where the heat is transferred from the waterside to the air side. The heat flux is only switched. The condensation/deposition mass flow rate will equal zero during these conditions. The air will heat up, which means that it can contain more water vapour and will not condensate.

3.1.5 Model description - Cross flow

An alternative setup is a cross-flow type heat exchanger. In this type, the flows do not flow in opposite directions but in perpendicular directions. An example of the cross-flow is the shell and tube exchanger, in which a fluid flows in the tubes, and the other fluid passes around the tubes in the shell. These are usually used in the two-phase system. Another type of cross-flow heat exchanger is the plate-fin heat exchanger, in which parallel plates connected by fins separate the two flows. The fluids flow through these fins. It is a compact heat exchanger with a relatively high heat transfer surface area to volume ratio [2]. A 2D variant of this plate-fin heat exchanger has been modelled, shown in Figure 12.

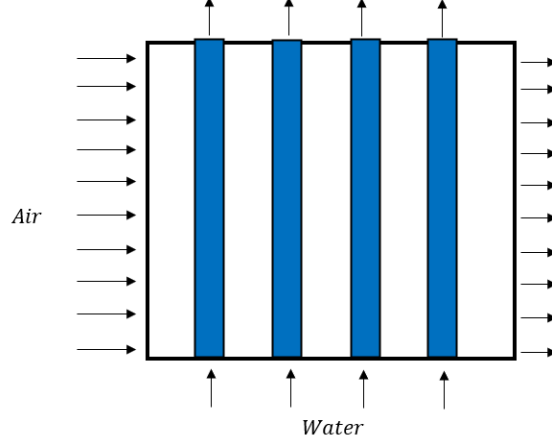


Figure 12: A schematic diagram of the 2D plate-fin cross-flow heat exchanger. The air flows from left to right, while the water flows through tubes from the bottom to the top.

Physically, it is impossible to construct a 2D plate-fin cross-flow heat exchanger according to the schematic diagram for unmixed flows. It is only possible if the flows flow perpendicularly on top of each other. This 2D model involves, therefore, only the coupling between the two domains by heat and mass fluxes. Furthermore, only the plates are incorporated. The fins are not included, which normally separate the air-flow into different sections.

Like the counter-flow model, the heat exchanger is subdivided into different sections. Unlike the counter-flow model, the air flows from top to bottom while the water flows from left to right in the tube. The heat and mass fluxes within the sectionalised cross-flow heat exchanger are shown in Figure 13.

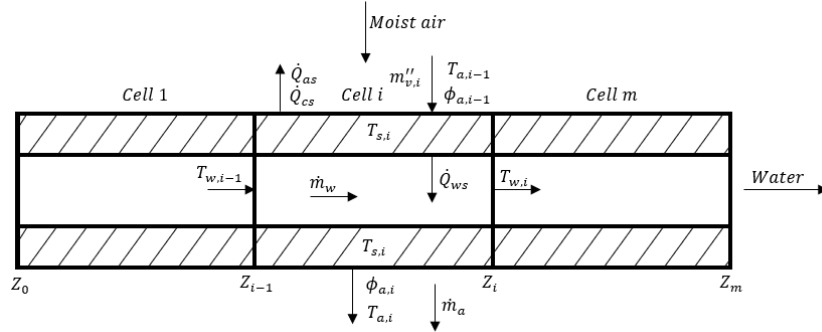


Figure 13: A sketch of the heat transfer of the entire water-air heat exchanger in wet conditions. The energy from the temperature decrease at the air side (\dot{Q}_{as}) and the latent heat (\dot{Q}_{cs}) of the condensation/deposition mass flux (m''_v) is transferred to the wall. The mass flux and change in air temperature results in a non-constant relative humidity (ϕ). These heat fluxes are equal to the heat supply rate on the waterside (\dot{Q}_{ws}). This heat supply will heat the cross-flowing water on the other side of the wall.

Similar assumptions have been made in the cross-flow model. Next, it is assumed that there is no heat exchange between the sections in the air domain in the horizontal direction. The air temperature difference between these cells is significantly lower compared to the temperature difference between air and water. Therefore, it is required to have a remarkably high amount of cells in the horizontal direction (flow direction of water). This is explained in the mesh convergence section 3.1.8.

The heat balances for the surface and water are similar to the heat balances of the counter-flow model. These are respectively shown in Eqs. 37 and 41. Only the flow direction of the air-flow is changed. Instead of flowing from boundary i to $i-1$, the air-fluid flows from boundary $i-1$ to i . This results in a heat balance of the air-fluid stream, in which $T_{a,i-1}$ and $T_{a,i}$ are reversed. That creates energy balances

for respectively the air side, waterside and surface:

$$\begin{aligned}
\dot{m}_w c_{p,w} (T_{w,i-1} - T_{w,i}) + \alpha_w A (T_{s,i} - T_{w,i-1}) &= 0 \\
\dot{m}_a c_{p,a} (T_{a,i-1} - T_{a,i}) + m''_{v,i} AL + \alpha_w A (T_{w,i-1} - T_{s,i}) &= 0 \\
\alpha_a A (T_{a,i-1} - T_{s,i}) + m''_{v,i} AL + \alpha_w A (T_{w,i-1} - T_{s,i}) &= 0
\end{aligned} \tag{42}$$

3.1.6 Model assembly

The model assembly for the counter-flow and cross-flow models is different. But for both geometries, a similar system algorithm is used. The following explanation is applicable on the counter-flow model. The energy balances, shown in Eq. 42, and a different grid are used for the cross-flow model.

As mentioned, the model employs one-dimensional heat and mass transfer based on a local averaging technique. The entire counter-flow heat exchanger is divided into different sections. On each boundary, shown in Figure 7, are the temperatures calculated according to the equations derived in the model description. This sectionalised approach of the one-dimensional heat and mass transfer can graphically be shown. The temperature, relative humidity, heat and mass transfer are shown for three different sections of the counter-flow heat exchanger, which are shown in Figure 10.

The heat transfer can be expressed in each cell. These heat transfer flows are in balance, which means that the heat transfer from the air-flow is in balance with the heat transfer to the water flow. The quasi-steady state assumption results in a stable energy flow within the time step. The quasi-steady energy balance for cell i can be expressed according to the relations derived in the model description section:

$$\frac{dQ_{w,i}}{dt} = \dot{m}_w c_{p,w} (T_{w,i-1} - T_{w,i}) + \alpha_w A (T_{s,i} - T_{w,i}) = 0 \tag{43}$$

$$\frac{dQ_{s,i}}{dt} = \alpha_a A (T_{a,i} - T_{s,i}) + m''_{v,i} AL + \alpha_w A (T_{w,i} - T_{s,i}) = 0 \tag{44}$$

$$\frac{dQ_{a,i}}{dt} = \dot{m}_a c_{p,a} (T_{a,i} - T_{a,i-1}) + m''_{v,t} AL + \alpha_w A (T_{w,i} - T_{s,i}) = 0 \tag{45}$$

As shown in the heat balances above, the index of the water temperatures is opposite from the index of the air temperatures. This difference is due to the direction of the heat flow rate. The air temperature decreases from boundary Z_i to Z_{i-1} and transfers its heat (\dot{Q}_{as}) to the waterside, while the water temperature increases from boundary Z_{i-1} to Z_i by the heat source (\dot{Q}_{ws}).

The relative humidity at both boundaries of cell i can be calculated with the following equation derived in Appendix A:

$$\phi_{i-1} = \phi_i \frac{\frac{T_{a,i-1}}{T_{a,i}} e^{\frac{17.67(T_{a,i}-273.15)}{(T_{a,i}-38.65)}}}{e^{\frac{17.67(T_{a,i-1}-273.15)}{(T_{a,i-1}-38.65)}}} - \frac{75.6064m''_{v,i}AT_{a,i-1}}{e^{\frac{17.67(T_{a,i-1}-273.15)}{(T_{a,i-1}-38.65)}}} \tag{46}$$

The expressions for the heat balance in each cell can be used for an energy balance in the entire system. Each cell needs to have an equation for the heat balance on the air and waterside and an equation for the relative humidity. Furthermore, the heat balance for the surface has to be applied for every boundary. This brings the number of equations per cell to five. Later, it will be explained that this is enough to solve this problem.

These equations can be assembled into a matrix-vector equation to create an expression for the en-

tire system consisting of multiple cells. The matrix-vector equation is shown below:

$$\begin{bmatrix} \dot{m}_w c_{p,w} S_1 - \alpha_w A S_2 & 0 & \alpha_w A S_2 & 0 \\ \alpha_w A S_2 & -\dot{m}_a c_{p,a} S_1 & -\alpha_w A S_2 & 0 \\ \alpha_w A S_2 & \alpha_a A S_2 & -(\alpha_w + \alpha_a) A S_2 & 0 \\ \alpha_w A S_3 & \alpha_a A S_3 & -(\alpha_w + \alpha_a) A S_3 & 0 \\ 0 & 0 & 0 & S_4 - S_2 \cdot H_1 \end{bmatrix} \begin{bmatrix} T_{w,0} \\ \vdots \\ T_{w,m} \\ T_{a,0} \\ \vdots \\ T_{a,m} \\ T_{s,0} \\ \vdots \\ T_{s,m} \\ \phi_o \\ \vdots \\ \phi_m \end{bmatrix} = \begin{bmatrix} 0 \\ \vdots \\ m''_{v,1} \\ \vdots \\ m''_{v,m} \\ 0 \\ \vdots \\ m''_{v,1} \\ \vdots \\ m''_{v,m} \\ 0 \\ \vdots \\ m''_{v,0} \\ \vdots \\ m''_{v,m-1} \\ \left(\begin{bmatrix} 0 \\ m''_{v,1} \\ \vdots \\ m''_{v,m} \end{bmatrix} A \right) \begin{bmatrix} T_{a,1} \\ \vdots \\ T_{a,m} \end{bmatrix} \\ \hline \left(\begin{bmatrix} T_{a,1} \\ \vdots \\ T_{a,m} \end{bmatrix} \right) \begin{bmatrix} T_{a,1} \\ \vdots \\ T_{a,m} \end{bmatrix} \\ \hline \exp \left(\begin{bmatrix} T_{a,1} \\ \vdots \\ T_{a,m} \end{bmatrix} \begin{bmatrix} -273.15 \\ \vdots \\ -38.65 \end{bmatrix} \right) \end{bmatrix} \quad (47)$$

in which

$$H_1 = \frac{\begin{bmatrix} T_{a,0} \\ \vdots \\ T_{a,m-1} \end{bmatrix} e^{\frac{17.67 \left(\begin{bmatrix} T_{a,1} \\ \vdots \\ T_{a,m} \end{bmatrix} \begin{bmatrix} -273.15 \\ \vdots \\ -38.65 \end{bmatrix} \right)}}{\begin{bmatrix} T_{a,1} \\ \vdots \\ T_{a,m} \end{bmatrix}} \quad (48)$$

$$S_1 = \begin{bmatrix} 1 & -1 & \vdots \\ \ddots & \ddots & \vdots \\ & & 1 & -1 \\ & & & & \ddots & \ddots \\ & & & & & & 1 & -1 \end{bmatrix}_{\substack{-1=1 \\ \text{cell } i=m \\ \text{cell } i=1}} \quad S_2 = \begin{bmatrix} 0 & 1 & \vdots \\ \ddots & \ddots & \vdots \\ & & 0 & 1 \\ & & & & \ddots & \ddots \\ & & & & & & 0 & 1 \end{bmatrix}_{\substack{-1=1 \\ \text{cell } i=m}} \quad (49)$$

$$S_3 = \begin{bmatrix} 1 & \vdots \\ \ddots & \vdots \\ & & 1 \end{bmatrix}_{\text{cell } i=m} \quad S_4 = \begin{bmatrix} 1 & 0 & \vdots \\ \ddots & \ddots & \vdots \\ & & 1 & 0 \end{bmatrix}_{\substack{-1=1 \\ \text{cell } i=m}}$$

This matrix-vector equation can be simplified into the following equation:

$$M \underline{B} = \underline{C} \quad (50)$$

As described, the water temperature at boundary Z_0 and air temperature and relative humidity at boundary Z_m are pre-described. These boundary conditions can be applied to the simplified matrix-vector equation to calculate the resulting temperature and air humidity. This creates a square matrix \tilde{M} which can be inverted to create a solution:

$$M\tilde{B} = \begin{bmatrix} \underline{b}_0 & \tilde{M} & \underline{b}_m \end{bmatrix} \begin{bmatrix} T_{w,0} \\ \tilde{X} \\ T_{a,m} \\ \phi_m \end{bmatrix} = \tilde{M}\tilde{B} + \underline{b}_0 T_{w,0} + \underline{b}_m T_{a,m} + \underline{b}_m \phi_m \quad (51)$$

$$\tilde{M}\tilde{B} = \underline{f} + \underline{c}, \underline{f} = -[\underline{b}_0 T_{w,0} + \underline{b}_m (T_{a,m} + \phi_m)] \quad (52)$$

The unknown temperature and relative humidity can be calculated by taking the inverse of the matrix \tilde{M} :

$$\tilde{B} = \begin{bmatrix} T_{w,1} \\ \vdots \\ T_{w,m} \\ T_{a,0} \\ \vdots \\ T_{a,m-1} \\ T_{s,0} \\ \vdots \\ T_{s,m} \\ \phi_o \\ \vdots \\ \phi_{m-1} \end{bmatrix} = \tilde{M}^{-1} \cdot (\underline{f} + \underline{c}) \quad (53)$$

3.1.7 Iterative solving

As described in the model description 3.1.4, the dependence between the relative humidity and the condensation/deposition mass flux is mutual. Furthermore, the air temperature is required to calculate the relative humidity downstream, as shown by Eq. 46. Therefore, the air temperature is the input and the output parameter in the matrix-vector equation, given by Eq. 47. That creates a non-linear matrix-vector equation. The non-linearity of the matrix-vector equation makes it impossible to get a valid solution by solving it once. This problem can only be solved iteratively [21].

The boundary conditions, latent heat, air temperature and the condensation/deposition mass flux are the input parameters of the matrix-vector equation, given by Eq. 47. These parameters need to be initialised before. Solving this matrix-vector equation gives a vector containing the air, water and surface temperature, and relative humidity at each boundary, which is given by Eq. 53. These values can be used to recalculate the condensation/deposition mass flux with Eq. 22 and 23. Iterative, this sequence is followed to solve the problem. In each iteration, the air, water and surface temperature and relative humidity at each boundary are calculated by solving the matrix-vector equation. Subsequently, the condensation/deposition mass flux is computed by using these parameters. This sequence is followed until a convergent solution is computed. Therefore, the following algorithm is followed to solve this problem iteratively:

1. Make an initial guess for each boundary's condensation/deposition mass flow. As described before, this model can also be applied to dry conditions. Therefore, the initial guess for the mass flow will equal zero.
2. Make an initial guess for the latent heat constant. Similar to the condensation/deposition mass flow, the initial guess for the latent heat constant will be equal to zero at each boundary.
3. Make an initial guess for the air temperature at each boundary. The air temperature is an input variable for the model at the inlet boundary of air. The initial guess is that the air temperature at the outlet boundary is decreased by 6 Kelvin. This depends on mass flux, heat exchange area and

temperature difference. From this guess, the air temperature at each boundary will be calculated according to the following expression:

$$T_{a,i} = T_{a,m} - \frac{6}{m}i \quad (54)$$

4. Compute the matrix-vector equation by filling in the computed variables for the condensation/deposition mass flux, latent heat and air temperature of the previous iteration. For the first iteration, these are the initialised values computed by steps 1 - 4.
5. Implement boundary conditions ($T_{w,0}$ $T_{a,m}$ ϕ_m).
6. Invert the matrix \tilde{M} and solve the matrix-vector equation $\tilde{B} = \tilde{M}^{-1} \cdot (\underline{f} + \underline{C})$. Solving this equation gives a vector containing the air, water and surface temperature, and relative humidity at each boundary, which is given by Eq. 53.
7. Calculate the condensation/deposition mass flux m_v'' at each boundary according to Eq. 22 and 23 with the temperatures and relative humidity calculated by solving the matrix-vector equation during step six.
8. Calculate the latent heat constant based on the mass flux calculated by step seven. Use Eq. 24 for this step.
9. Calculate the change between the calculated mass flux m_v'' in the previous and this iteration. The change between the initial guess and the calculated mass flux m_v'' can be calculated for the first iteration.
10. If the change, which has been calculated by step nine, is not equal to zero, go back to step five. Otherwise, the solution is converged and can be used to make figures and calculate the frost layer thickness.

The condensation/deposition mass flux is the convergence criterion. This variable is adjusted every iteration based on differences in the solution of the matrix-vector equation. If this solution, so the temperatures and relative humidity, does not change anymore, the condensation/deposition mass flux values at each boundary will also not change anymore. This means that the solution is converged.

First, the solution of the matrix-vector equation has been computed within each iteration. After that, the condensation/deposition mass flux is calculated with the solution of the matrix-vector equation. This condensation/deposition mass flux influences the temperature, and relative humidity, called mutual dependence. So, if the value of the condensation/deposition mass flux is changed, the temperature and relative humidity must also be changed. Reversed, if the values of the temperature and relative humidity are changed, the condensation/deposition mass flux needs to be changed as well. The condensation/deposition mass flux is calculated after computing the temperature and relative humidity within the algorithm. If the temperature and relative humidity differ from the values calculated within the previous iteration, the condensation/deposition mass flux has to be recalculated. This influences the temperature and relative humidity, so these values must be adapted again by solving the matrix-vector equation. This process will be continued until the condensation/deposition mass flux, and governing temperatures and air humidity do not change anymore, which means that the model shows convergence.

Not in all cases will the condensation/deposition mass flux converge. If the relative humidity increases above the saturation level, the amount of water vapour that causes this over-saturated situation needs to condense to bring the relative humidity back to saturation level, 100%. The amount of water vapour that has to condense can be calculated with Eq. 23 in the 1st iteration. This equation has only a non-zero value for over-saturated situations. If the air has a relative humidity at or below saturation level, the value of the condensation mass flux is equal to zero. As described before, the latent heat from the condensing water vapour also influences the air temperature. This air temperature is calculated with this condensation/deposition mass flux by solving the matrix-vector equation in the 2nd iteration. Due to the latent heat, the air temperature will be increased. That means the air temperature can contain more water vapour, resulting in relative humidity below the saturation level. Consequently, the amount of water vapour that has to condense due to the saturation level, calculated with Eq. 23, is equal to zero. Condensation is only possible if the fluid is in contact with a surface at a temperature beneath

its dew point. Generally, this condensation/deposition mass flux is lower, resulting in less latent heat. This results in a lower air temperature and relative humidity above saturation level, calculated in the 3rd iteration. This pattern will be repeated and not result in a converged mass flux. An example is shown in the following figure:

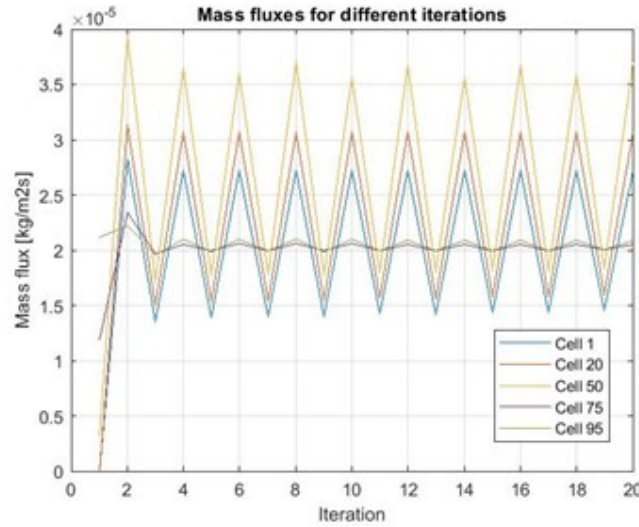


Figure 14: A figure of the mass fluxes in 5 different cells (1, 20, 50, 75, 95) for different iterations. In the first iteration, the mass flux for all cells is initially set at zero. After the first iteration is, the mass fluxes calculated based on the solution of the matrix-vector equation. The relative humidity increases above the saturation level in this example. That means that the correction method needs to be applied. In the second iteration, the correction method is applied, resulting in a higher mass flux. That brings the relative humidity for the next iteration, the third iteration, back below the saturation level. For this iteration, the correction method is not applied, resulting in a lower mass flux. This pattern is repeated in the following iterations.

According to the sketched converging problem can be concluded that the way, in which the equation for the condensation/deposition mass flux in over-saturated conditions is implemented, creates an overshooting condensation mass flux. That results in a relative humidity decrease beneath the saturation level. This means the model is unstable enough to find the correct condensation mass flux. The stability of the model has to be improved. This can be achieved by adding a relaxation factor which mutes the fluctuations between the iterations. In this way, the change in condensation/deposition mass flux can be limited so that fluctuations will decrease and finally converge. Conservation of energy is preserved. The relations described within Section 3.1 do not change. Only the fluctuation of variables between iterations is changed. The way the equations are solved within the iteration is not changed. In the iteration, the energy balances are solved.

The relaxation factor determines how much the variable changes from the previous iteration to the next. The method of under-relaxation limits this variable change. Within the model, this limits the change of the condensation mass flux. The condensation mass flux of iteration n can be computed with the following equation:

$$m_v''^n = m_v''^{n-1} + \gamma \times (m_v''^{n*} - m_v''^{n-1}) \quad (55)$$

in which $m_v''^n$ is the condensation mass flux of iteration n , which is controlled by the relaxation factor γ . This value is computed with the $m_v''^{n-1}$, the condensation mass flux of iteration $n - 1$ and $m_v''^{n*}$, the condensation mass flux which is calculated based on the methods described before. In the case of manual relaxation, values between $0.3 < \gamma < 0.7$ are recommended.

By applying the under-relaxation factor, the mass flux will show convergence. For the case, which is shown in Figure 14, the mass fluxes at different sections will show convergence by applying this solution. This is shown in the following figure:

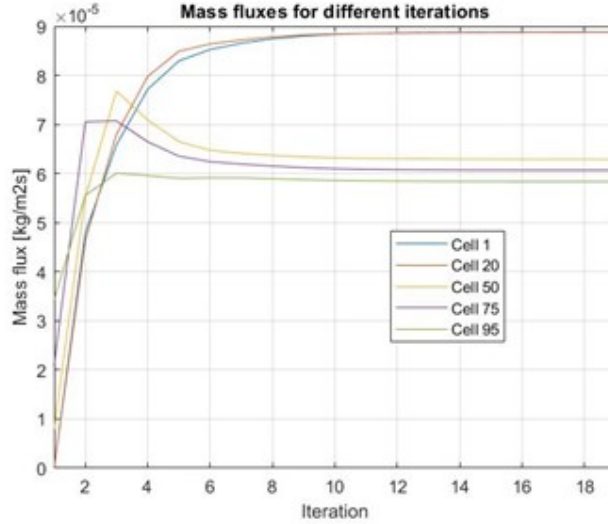
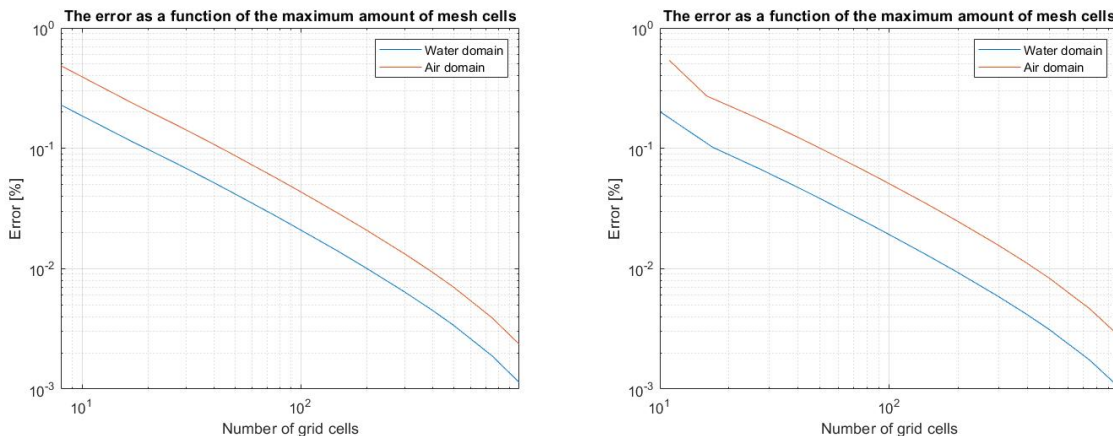


Figure 15: A figure of the mass fluxes in 5 different cells (1, 20, 50, 75, 95) for different iterations. In the first iteration, the mass flux for all cells is initially set at zero. After the first iteration is, the mass fluxes calculated based on the solution of the matrix-vector equation. Unlike the mass flux shown in figure 12, the mass fluxes showed no convergence. This can be done by limiting the change of the condensation mass flux compared to the previous iteration. This figure shows that the mass flux on most boundaries shows convergence after ten iterations. This results in less computational time for the model.

3.1.8 Mesh/time convergence

The MATLAB model is divided into several sections, shown in figure 7. The variables are computed on the boundaries of each section. A certain amount of sections is required to describe the phenomena within the heat exchanger. Too little sections cannot describe these phenomena and affect the accuracy. The rate of accuracy can be determined by performing a mesh convergence study. Mesh convergence is met if the result of the model is not affected by further increasing the number of sections. The number of sections can only be increased in the flow direction of the water flow for both counter flow as a cross-flow model.

The relative error for the grid cell count and the time step is computed as the relative error of the temperature compared to the temperature of the largest grid cell count. This selected boundary is in the centre of each domain.



(a) The relative error for the counter-flow model as a function of the grid cell count. (b) The relative error for the cross-flow model as a function of the grid cell count.

Figure 16: The convergence plots of the mesh convergence study with a time step size of 1 s.

The mesh size must be reduced to decrease the relative error, according to figure 16. Halving the

mesh size leads to an increase in computation time by a factor of 2. Selecting a proper mesh size is arbitrary since no experimental data is available for a condensing counter-flow heat exchanger. The mesh with 200 sections has been chosen by incorporating the computation time. The relative error is equal to 0.01% compared to the most refined mesh of 2000 sections. This means that the absolute temperature difference lies within 0.025 - 0.035 K. Most accurate commercial temperature sensors have an accuracy of 0.05 °C [48]. That means the relative error is lower than the minimum error of measurement devices.

The model consists of differential equations in which only the function's first derivative appears. The general transport equation, Eq. 33 consists of first-order derivatives of the temperature in the flow direction of the fluid stream. These equations should compute a first-order model accuracy [13]. This quantifies the maximum rate of convergence of a numerical approximation. The log-log slope of the mesh convergence plots can determine the accuracy rate in space. The slope of both mesh convergence plots, shown in figure 16, equals one. This means that the model has a first-order accuracy in space, which is equal to the accuracy of the equations used within the model.

The order of accuracy in time can only be determined for cases with frost growth. This frost layer's growth affects the air's mass flow rate, given by Eq. 26. This also influences the temperatures indirectly. The influence on the temperature in time has to be described properly. Therefore, it is required to compute the perform a time-step convergence study. In situations without frost growth, air's mass flow rate remains the same, resulting in non-varying temperatures over time. The steady-state solution can only be calculated for these situations.

Figure 17 shows the relative error for different time-step sizes.

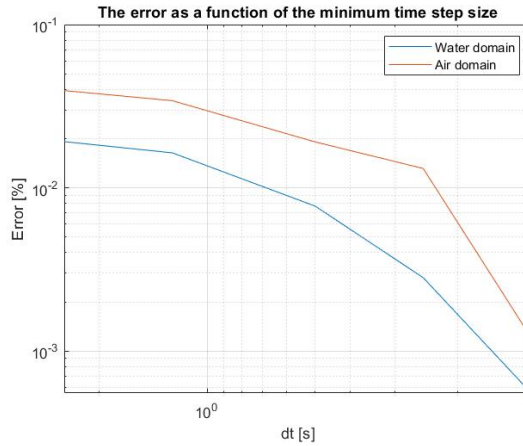


Figure 17: The relative error for the counter-flow model as a function of time step size with grid cell count = 200.

According to the time convergence plot, shown in Figure 17, is the order of accuracy in time also equal to one. Also, for selecting a time step size, the selection is arbitrary. The same convergence criteria have been applied compared to the mesh convergence study, meaning the relative error has to be beneath 0.01%. This criterion holds to a time step size of 0.0125 s according to Figure 17.

3.2 ANSYS model

Different heat exchanger geometries are modelled in ANSYS Fluent. The study was conducted for a 2D counter-flow heat exchanger within ANSYS Fluent. The materials used in each model are identical to those in the 1D MATLAB model.

3.2.1 Model explanation

The model is fundamentally based on two physical laws that apply to each flow independently of the nature of the fluid under consideration [54]. The law of conservation of mass states that the mass is conserved over time [45], and can be written as follows:

$$\frac{\partial \rho}{\partial t} + \nabla \cdot (\rho \vec{u}) = S_m \quad (56)$$

Eq. 56 is the general form, which describes the conservation of mass of the entire mixture and is valid for incompressible and compressible flows. The air-flow can also be considered as an incompressible flow since its changes in density are negligible at Mach numbers less than 1.0 ($\text{Mach} < 0.3$) [4].

The general form of the law of conservation is sufficient to describe the conservation of mass of the water fluid stream. Nevertheless, the air-flow is a mixture of water vapour, liquid and solid (frost) phases of water. The amount of mass of each substance needs to be conserved and is described by the continuity equation for the volume fraction of each substance. For each substance q , this can be expressed as:

$$\frac{1}{\rho_q} \left[\frac{\partial}{\partial t} (\alpha_q \rho_q) + \nabla \cdot (\alpha_q \rho_q \vec{v}_q) = S_{m,q} \right] \quad (57)$$

Due to condensation and deposition, mass transfer between the individual substances is defined by the source term $S_{m,q}$. The expressions given in Section A express the amount of mass transfer from water vapour to liquid water or frost. These equations are differently implemented compared to the 1D model, presented in Section 3.1. Only computational cells adjacent to the heat exchange surface can have a condensation or deposition mass flux due to contact with a surface at a temperature beneath the dew point. For these cells, both Eq. 22 and 23, are used to calculate the condensation/deposition mass flux per unit area. The maximum value of either expression is used as the source term for Eq. 81. The condensation/deposition mass flux due to contact with a surface at a temperature beneath its dew point has been calculated based on the surface temperature. This temperature can only be computed if the wall has a certain thickness. If this is not the case, the wall is a non-conformal wall with no thickness. This means that the interface wall has no nodes. The surface temperature is then replaced by the water temperature adjacent to the air-fluid domain.

Other cells not adjacent to the heat exchange surface have only a condensation/deposition mass flux if the humidity increases above its saturation level due to a decreased air temperature. For these cells, the source term can be calculated with Eq. 23.

Within the ANSYS model, the mass exchange between phases and the conservation of mass of each substance is governed by the Volume of Fluid (VOF) method. A more elaborate explanation can be found in Section B.1.

The liquid water and frost substances are modelled by one material. The phase in which the material exists is expressed by the liquid fraction. This is the volume fraction of the amount of liquid/solid water that is in liquid form. The transition process from liquid to solid starts at the liquidus temperature, and at the solidus temperature is the full solidification achieved [46]. For water, both temperatures are equal to each other. This approach models the frost layer as a porous medium. The porosity, the fraction of the solidified volume, determines the liquid velocity and the level of solidification. When the cell is completely solidified, the porosity becomes zero, and the liquid velocity drops to zero [8]. Within the ANSYS model, the liquid fraction is governed by the Solidification method. A more elaborate explanation can be found in Section B.2.

Latent heat is released during the phase transition from water vapour to either liquid water or solid water (frost). The latent heat of condensation is expressed by the difference in enthalpy of the formation of water vapour and liquid water, equal to $+2260\text{e}3$ J/kg. This is the value of the latent heat of vaporisation multiplied by minus one. The latent heat due to frost formation is expressed by the latent heat of melting multiplied by minus one, equal to $+334$ J/kg. This is the amount of heat released by converting a unit mass of the liquid into a solid without a temperature change.

This is only one type of heat transfer which is considered within the model. Also, sensible heat is exchanged within the thermodynamic system. Sensible heat is heat exchanged by a temperature change of a fluid/solid. Next to the conservation of mass, the total energy is also conserved within the heat exchanger. As described in Section 2.3, the heat of the air-flow is transferred to the water flow by forced convection, conduction and condensation/deposition. The total sum of heat transfer within the heat exchanger is equal to zero and can be written as follows [1]:

$$\frac{\partial}{\partial t} (\rho E) + \nabla \cdot (\vec{u}(\rho E + p)) = \nabla \cdot \left(k_{\text{eff}} \nabla T - \sum_j h_j \vec{J}_j + (\vec{\tau}_{\text{eff}} \cdot \vec{u}) \right) + S_h \quad (58)$$

The first three terms on the right-hand side of Eq. 58 represent energy transfer due to conduction, species diffusion, and viscous dissipation, respectively. The source term (S_h) includes the heat of a chemical reaction, like condensation or deposition. The amount of energy can be expressed in terms of sensible enthalpy, pressure, density and velocity:

$$E = h - p/\rho + u^2/2 \quad (59)$$

For incompressible flows, the sensible enthalpy can be calculated based on the sensible enthalpy of individual phases, given in Equation 87.

$$h = \sum_j Y_j \int_{T_{ref}}^T c_{p,j} dT + \frac{p}{\rho} \quad (60)$$

The reference temperature is 298.15K.

The mass flows of both fluids have to have a value in a similar range to create an observable temperature change within both fluids. The density of the air is substantially lower than the density of the counter-current flowing water flow. Therefore, the air domain's cross-flow area or the air-fluid stream's inlet velocity has to be remarkably higher. Increasing the inlet velocity can sometimes create a fluid flow in its turbulent regime depending on the Reynolds number [50]. The governing equations described above need to be modified with additional unknown variables to describe this flow. Turbulent models are required to determine these variables. Within this model, $k - \varepsilon$ turbulence model is used. This is a method based on Reynolds-averaged Navier-Stokes (RANS) equations that expresses the mean and fluctuating velocity of the fluid stream. The standard $k - \varepsilon$ model consists of transport equations for the turbulence kinetic energy k and its dissipation rate ε [50]. The transport equations for these variables are as follows:

$$\frac{\partial}{\partial t}(\rho k) + \frac{\partial}{\partial x_i}(\rho k u_i) = \frac{\partial}{\partial x_j} \left[\left(\mu + \frac{\mu_t}{\sigma_k} \right) \frac{\partial k}{\partial x_j} \right] + G_k + G_b - \rho \varepsilon - Y_M + S_k \quad (61)$$

$$\frac{\partial}{\partial t}(\rho \varepsilon) + \frac{\partial}{\partial x_i}(\rho \varepsilon u_i) = \frac{\partial}{\partial x_j} \left[\left(\mu + \frac{\mu_t}{\sigma_\varepsilon} \right) \frac{\partial \varepsilon}{\partial x_j} \right] + C_{1\varepsilon} \frac{\varepsilon}{k} (G_k + C_{3\varepsilon} G_b) - C_{2\varepsilon} \rho \frac{\varepsilon^2}{k} + S_\varepsilon \quad (62)$$

in which μ_t is the turbulent viscosity and Y_M is the fluctuating dilatation in compressible turbulence to the overall dissipation rate. The constants ($C_{1\varepsilon}$, $C_{2\varepsilon}$, $C_{3\varepsilon}$, σ_k and σ_ε) have default values, and the turbulent viscosity can be computed by combining the k and ε .

These equations describe the fluid flows and heat exchange within the heat exchanger. Additional relations are required at the boundary conditions. Three different boundaries are present in the heat exchanger: wall, inlet, and outlet. Each type of boundary has its boundary conditions.

- The Dirichlet type of the no-slip condition is the condition for the velocity components at solid walls [50]. The fluid has a zero velocity relative to the boundary in parallel and perpendicular directions for nodes adjacent to the wall. A multi-layered near-wall boundary layer is formed with a transition between the laminar and turbulent wall flow. An explanation is given in Section B.3.
- The boundary condition at the inlet boundaries is also a Dirichlet boundary condition. This means that the inlet velocity equals a single value for the entire boundary. Next, the turbulence parameters (turbulence intensity and turbulent viscosity) have to be defined [58].
- The pressure-outlet boundary condition describes the outflow boundary. The static pressure of the environment into which the flow exhausts is described along the entire boundary.

The expressions given above describe the conservation of mass and energy. These expressions explain, in essence, the ANSYS model. In practice, the model consists of more expression. A more elaborate explanation is given in the ANSYS theory guide [1].

3.2.2 Solvers

Solving a multiphase system may result in some stability of convergence problems. Time-dependent problems need to have a proper initial field to avoid instabilities. Stability is also increased when a higher-order numerical scheme is used, and the simulation starts with small time steps. The time step

size can be increased after a couple of time steps. It is recommended to run the simulations with a 2nd order upwind scheme [50]. This scheme includes 3-point backward or forward differencing and should give a 2nd order accuracy.

The accuracy of steady-state solutions can be increased by using a coupled pressure-based solver. This coupled algorithm solves the momentum and pressure-based continuity equations together [1] and is incompatible with periodic mass-flow boundary conditions. Appendix C shows the iterative time algorithm. The used under-relaxation factors are implicit, except for velocities and pressure. Coupling between the equations is achieved by discretising the pressure gradient terms in the momentum equations. The created semi-implicit solution results in a slow converging solution. This approach is also beneficial for the robustness and efficiency of single-phase flows. The coupled approach is required for a coarse mesh or large time steps for time-dependent simulations. Complex problems or higher-order schemes can still result in non-converging solutions. Reducing the Courant number makes the solution more robust [50]. For Euler or Navier-stokes equations, the Courant number must be less or equal to one. The Courant number can be expressed as:

$$C \equiv \frac{u\Delta t}{\Delta x} \leq 1 \quad (63)$$

Nevertheless, a Courant number of 0.5 is recommended for the initial stage of the simulation and can be increased to 1 after a while [14]. This requirement has to be taken into account by making a proper mesh.

All these equations are coupled and solved with a pressure-based solver. The algorithm is shown in Appendix C.

3.2.3 Geometries

The model has been applied on a 2D counter-flow current geometry. Within this geometry, the dimension is arbitrary for each case described within Sections 4 and 5. The 2D counter-flow geometry consists of two domains that share one interfacial wall. The counter-flow geometry is shown in the following figure:



Figure 18: The geometry which is used in the ANSYS model. This geometry has, comparable to the MATLAB model, two different domains. One domain for the water flow (top) and one for the humid air flow (bottom). The water-flow enters the domain on the left side (green boundary) and leaves the domain on the right side (red boundary). The air flows in other direction, from the right (blue boundary) to left (yellow boundary). The two domains are divided by an interfacial wall (black boundary) and separated from the surroundings by an adiabatic wall (orange boundaries).

The top domain of Figure 18 contains a water fluid stream. This fluid stream only consists of water. No phase change is considered within this fluid domain. The fluid stream can be described by the law of conservation of mass, given by Eq. 56, and the law of conservation of energy, expressed by Eq. 58. The water fluid flows into the heat exchanger through the green inlet boundary of Figure 18 and flows out of the heat exchanger through the red boundary of Figure 18. The inlet velocity is uniform over the inlet boundary. It is transformed into a fully-developed velocity profile due to viscous forces within the fluid and the Dirichlet type of the no-slip condition at both walls, indicated by the top orange and black line in Figure 18.

The bottom domain consists of the air-fluid stream. This flow flows opposite to the water fluid stream, from the blue to the yellow boundary of Figure 18. In some cases, the flow has a Reynolds number and tends to be turbulent. The transport equations of the $k - \varepsilon$ model describe the turbulent behaviour, given by Eq. 61 and 62. The fluid stream contains air with an arbitrary amount of water vapour at the inlet boundary. The continuity equation expresses the conservation of the mass of each substance, given

by Eq. 81. Water vapour can also condense into liquid water or de-sublimate into a frost layer. The condensation/deposition mass flux is defined by the source term of Eq. 81. The expressions given in Section A, express the amount of condensation mass transfer from water vapour to either liquid water or frost. These equations describe the mass condensation transfer as a function of the wall temperature. As described in Section 3.2.1, the wall is modelled as a non-conformal wall, which means that the wall does not consist of nodes. Therefore, the surface temperature is replaced by the water temperature adjacent to the air-fluid domain. As described in Section 3.2.1, the liquid and solid phases are expressed by one material. The fraction of this material, which is in the liquid phase, is expressed by the liquid fraction of the solidification model, described by Section B.2. This fraction is determined based on the cell temperature. If this temperature is below the freezing point of water, the liquid fraction is equal to zero. Otherwise, the liquid fraction is equal to one. The temperature is not defined per material. It is equal to the cell temperature.

The Solidification model is only applied to liquid/solid material. For other materials (water vapour and air), the freezing point is set at 0 Kelvin, and the melting heat is set at 0 J/kg. The material cannot change into a solid phase if the temperature stays above this value. Furthermore, the water material used in the water domain is modelled by a different material with the same density, specific heat, thermal conductivity, viscosity and molecular weight as the liquid/solid material described above. This material's freezing point and melting heat are also equal to zero. In this way, the Solidification model does not influence the water fluid stream in the water domain.

The condensation/deposition mass flux equals zero in cases where the absolute humidity remains constant. In this situation, the Volume of Fluid and Solidification models are still applied on the air-fluid domain, but these have no function since there is no mass transfer between phases and no liquid/solid water is formed.

All boundaries shown in Figure 18 occur in each case. Boundary conditions, which are described in section 3.2.1, are applied to each of them. Only the height and width of both domains can differ within each case. Based on these dimensions, the amount of mesh cells is chosen. The required mesh cell amount is described in section 3.2.4.

3.2.4 Mesh/time convergence

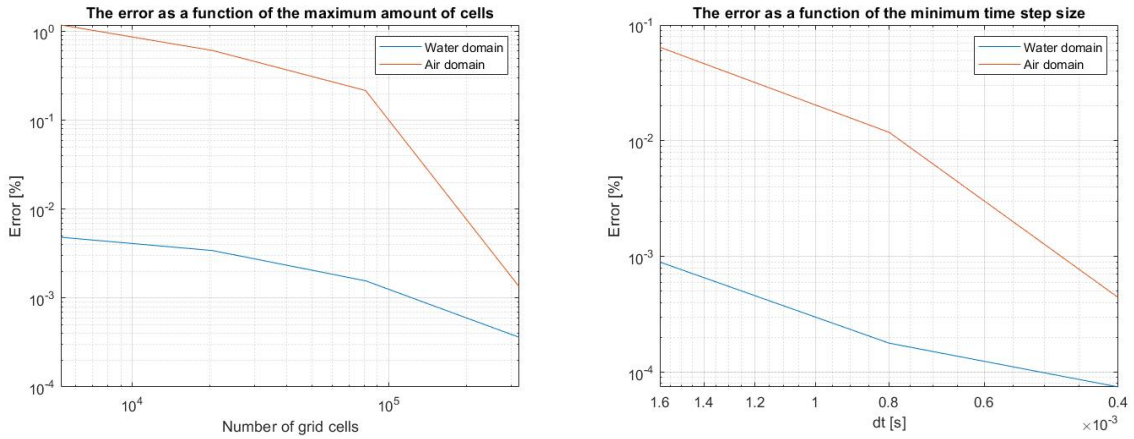
The model is solved with a pressure-based solver, described in Section 3.2.2. This solver solves the equations, which are described in Section 3.2.1, iterative. Like the 1D model, under-relaxation factors are used within the solver to reduce solution oscillations and increase the stability of the simulation. These factors limit the relative change between the iterations, which will also introduce an error in the mass and energy balance. A maximum error of 10^{-6} is set for the continuity parameters, like velocity and turbulence, to ensure that the solution is sufficiently accurate. This error is insufficient for volume fractions, and energy since the volume fraction of condensed water vapour has values in the order of 10^{-6} . The maximum error for these parameters is set at 10^{-9} , which results in a maximum relative error of 0.1 %. That has to be reached before the simulation is allowed to continue with the next time step.

The domain, shown by Figure 18, is divided into a grid with nodes. All equations of Section 3.2.1 are solved on each node. A sufficient amount of nodes is required to describe the heat and mass transfer phenomena within the heat exchanger. If the result of an analysis is not affected by an increase in the amount of nodes, mesh convergence is reached. The amount of nodes can be increased by decreasing the distance between them, also known as the mesh size. Typically, the smaller the mesh size, the more accurate the solution. During the mesh convergence study, the mesh size is decreased until the solution is not affected by further decreasing the mesh size.

The mesh of the 2D counter-flow geometry has a given amount of mesh points in the vertical and horizontal directions. Both flows move horizontally in opposite directions and exchange heat along their flow direction. The height and width of both domains are arbitrary. The distance between the nodes in vertical and horizontal direction is similar due to the limited available time for the mesh convergence study. For instance, if the domain has a height of 10 millimetres and a width of 100 mm. This means that the ratio for the number of nodes equals 1×10 (h x w). This ratio and the time step size of the transient simulation are kept constant while performing the mesh convergence study. The time step size

is kept constant to investigate the mesh size's influence. The used time step size is chosen so that the Courant number of the most refined mesh, given in Eq. 63, is not larger than one. This Courant number is adapted to the most refined mesh since a mesh refinement, by decreasing Δx with a constant time step Δt of Eq. 63, increases the Courant number. To keep the value Courant number for the most refined mesh size beneath 1, the Courant number must be equal to one for this mesh size. Coarsening the mesh results in a lower Courant number. In this way, the requirement of Eq. 63 is met for all mesh sizes.

There is no experimental data available to compare the model results with. So, comparing the results with this kind of data is impossible. It is only possible to compare it with the most accurate solution available. Typically, the smaller the mesh size, the more accurate the solution. Therefore, the error for the solution of each mesh size is expressed as the relative error to the solution of the most refined mesh. The temperature of a single mesh point within each domain is used as a variable to compute the relative error. This selected mesh point is in the centre of each domain. In this way, the boundary conditions less influence the relative error.



(a) The relative error as a function of the grid cell count with time step size = $1e-04$ (b) The relative error as a function of the time step with grid cell count = 322,000

Figure 19: The convergence plots of the mesh and time step convergence study for a 2D counter-flow geometry.

The time step size has been kept constant during mesh refinement, which is shown in the caption of Figure 19a. The default mesh size, used for the time step refinement, has two hundred mesh cells vertically and eight hundred mesh cells in the horizontal direction per flow domain.

To decrease the relative error, the time or mesh size must be reduced. Halving the mesh size increases computation time by a factor of 4 while halving the time step only increases the computation time by 2. The relative error criteria are primarily based on accuracy but secondary on computation time. The relative error may not exceed $10^{-3}\%$ to keep the computation time-limited. This is an arbitrary value since the literature states that the convergence criteria can not only be based on relative error. Next to that, it is required that each time step shows convergence according to the requirements stated before. Choosing a relative error of $10^{-3}\%$ means that the absolute temperature difference to the most refined mesh is equal to 0.1. This is not the overall accuracy of the model since the most refined mesh computes not the exact solution. It is only the most accurate solution available.

According to the convergence criteria for the relative error, the decision was made to use a grid cell count of 322,000 for a domain size of 2 m (horizontal, flow direction) by 0.01 m (vertical) and use a time step size that results in an average relative error beneath $10^{-3}\%$. The time step closest to this requirement is $4e-04$ s, which will be used during the simulations. The corresponding Courant number is equal to one.

The simulations have been computed with a second-order upwind scheme, which should compute a second-order accuracy [50]. This quantifies the maximum rate of convergence of a numerical approximation to the exact solution. According to the slope of the convergence figures, Figure 19, has the solution a

first-order accuracy in time and space. This is a lower order of accuracy than expected from the used numerical scheme. The difference can be the result of the multiphase system approach which has been used.

From Figure 19 can also be concluded that the air domain has a higher order of accuracy than the water domain. The difference in flow characteristics could be the reason for this difference. Since the relative errors are based on the results of the most refined mesh and not on exact results, it is only possible to list possible reasons for this difference. In the literature, there is also no evidence for this difference. A possible reason could be the difference in velocity. The air-fluid stream has a relatively high velocity, even in the turbulence flow regime. The turbulent fluctuations require a small mesh size. Decreasing the mesh size can incorporate these phenomena even better, resulting in a steeper decline in the relative error.

4 Validation

In this chapter, the numerical results of both models are presented. The segmented heat exchanger model in MATLAB provides a 1D spatial distribution of the heat exchanger’s physical properties over time and in a steady state. These results are compared to the results of the 2D spatial distribution heat exchanger model in ANSYS. The results of this 2D spatial field are processed to compare with the 1D spatial field of MATLAB simulations, which is explained in Appendix D.1.

4.1 Heat exchanger conditions

Different heat exchange setups have been applied within the presented models. This differs for the fluids (water/water or water/air), heat exchange area and inlet conditions (temperature, velocity & relative humidity). These variables are varied to create different setups, which can be used to compare both models. These setups are described in Table 1.

Case number	Flow configuration	Heat exchange area [m^2]	Mass flow air [kg/s]	Relative Humidity [-]	Air temperature [K]	Mass flow water [kg/s]	Water temperature [K]
Case 1*	counter (water-water)	0.579	0.019	0.0	343.15	0.072	303.15
Case 2*	counter	0.5	0.147	0.0	300	0.098	280
Case 3*	counter	5	0.147	0.0	300	0.098	280
Case 4*	counter	5	0.147	0.0	290	0.098	280
Case 5*	counter	0.5	0.0735	85.7	290	0.0499	280
Case 6	counter	0.5	0.0735	80.8	280	0.0499	260

Table 1: Conditions of the various setups to compare the ANSYS & MATLAB model. *steady-state cases

Transient simulations are executed for 500 seconds with a time step size chosen so that the Courant number equals one. The number of mesh cell count of the ANSYS model is scaled to the selected mesh in Section 3.2.4.

The wall, which separates the air- and water flow, has a constant thickness of 0 mm and is made of stainless steel. The constant thermal conductivity and density of stainless steel equal 45 W/m.K and 8030 kg/m³, respectively. The physical properties of water, water vapour and air are described in Table 2.

Property	Air	Water (l)	Water (v)
Density [kg/m^3]	1.225	998.2	0.5542
Thermal conductivity [W/(m.K)]	0.0242	0.6	0.0261
Specific heat [J/(kg.K)]	1006.3	4186	0.147
Molecular weight [kg/kmol]	28.97	18.02	18.02
Standard state enthalpy [J/kg.mol]	0	-282.6e5	-241.8e5
Pure solvent melting heat [J/kg]	-	334e3	-

Table 2: Physical properties of fluids used in heat exchanger simulations.

4.2 Dry conditions

Numerical results of the steady-state ANSYS and MATLAB models are compared. To incorporate the 2D geometry within the 1D model, the heat transfer coefficient of the 1D model is equal to the mean value of the 2D model and based on the inlet velocity for each case shown in Figure 1. This coefficient is a constant within the 1D model and is calculated based on the method described in Section 2.3.

For dry conditions, it is also possible to compare the heat exchange rate with the NTU and LMTD method, described in Section 2.3. Heat transfer coefficients have been calculated based on values in the numerical model. Therefore, this method is only partially independent of the numerical models.

The heat transfer rate \dot{Q} can be computed with Eq. 18 by using the value for both fluids' effectiveness and input temperatures. This value can be compared by the sum of the segmented heat exchange rate of the MATLAB model, given by Eq. 41. Furthermore, it is compared to the heat transfer rate of the ANSYS model. This amount of heat transfer is related to the decrease in the bulk air temperature over the length of each mesh cell in the flow direction. The total heat released by this temperature decline equals the heat transfer rate.

Next to comparing the heat exchange rate, the temperature profiles of both fluid streams are compared. The bulk temperature in both fluid streams has been calculated to compare the 2D ANSYS model with the 1D MATLAB model. The data needs to be processed, which is explained in Appendix D.1. Figure 20 shows the computed temperatures along both channels by the 1D and 2D models for case 1, described in Table 1. The air-fluid within the bottom domain is replaced by a water fluid stream, indicated by the flow configuration in Table 1.

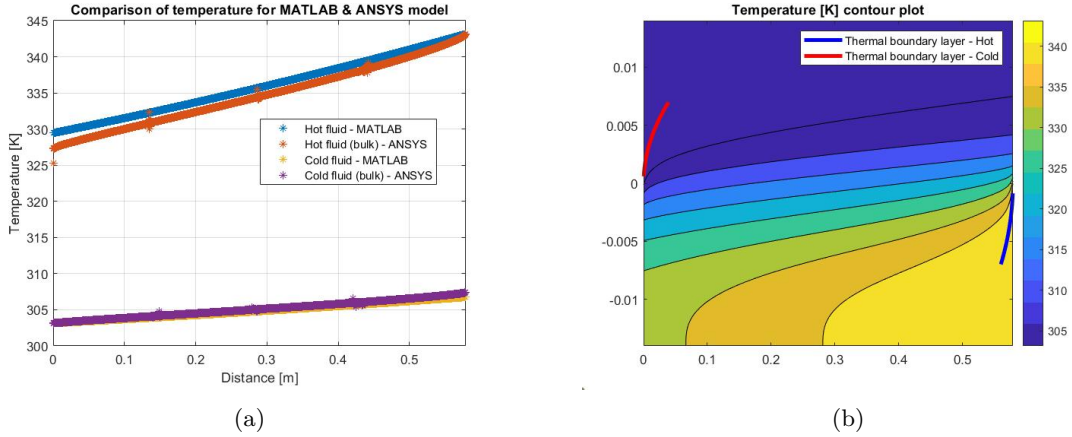


Figure 20: The temperature profiles of the ANSYS & MATLAB model for Case 1 with the bulk temperature (a) and the contour plot of the 2D model (b).

Looking at the temperature profiles in Figure 20a it becomes clear that the trends of the predicted temperatures along both fluid streams are in fair agreement. Only close to the inlet and outlet boundaries, there are some small deviations due to the different flow profiles and the lack of the thermal boundary layer.

The fluid enters a pipe at a uniform velocity, and due to viscous forces within the fluid and the no-slip condition at both walls, a fully-developed velocity profile is formed. This flow is similar to the type of flow considered in the 1D model. This fully-developed flow has a velocity equal to zero close to the wall and gradually increases to the centerline of each channel. The boundary layer is the thin transition layer between the wall and the bulk fluid flow. The thickness is defined as the distance from the solid body to the point at which the flow velocity is 99% of the free-stream velocity v_∞ , and can be expressed as:

$$\delta \approx 5.0 \frac{x}{\sqrt{Re}} \quad (64)$$

This layer also influences the heat transfer rate, governed by the thermal boundary layer. The velocity close to the wall is remarkably lower than the velocity in the centre of the fluid stream. This affects the heat transfer coefficient, given by Eq. 6. A lower value for velocity results in a lower heat transfer coefficient, expressed by Eq. 7. A lower heat transfer coefficient has a negative effect on the heat transfer rate. This results in a lower heat transfer rate for a fully-developed flow. Furthermore, the temperature varies with the temperature at the wall to the free-stream temperature at the center of the fluid domain. This temperature variation is the same over the entire length of the heat exchanger, but the thickness of the boundary layer will keep increasing. This means the temperature gradient (dT/dx) will keep decreasing (dx keeps increasing, while dT remains constant). This results in a lower heat transfer rate over the wall. Thicker is the boundary layer, and lower is the heat transfer rate. The thickness of the thermal boundary layer is linked to the thickness of the boundary layer by the Prandtl number and can

be expressed as [40]:

$$\frac{\delta}{\delta_T} = \text{Pr}^{1/3} \quad (65)$$

As the flow continues from the leading edge, the boundary layer increases in thickness. Until the layer is fully developed, the larger the distance from the leading edge, the higher the negative effect on the heat transfer rate. The thickness for the thermal boundary layer of both fluid streams is shown in Figure 20b. After some distance from the leading edge, the thickness of the boundary layer is equal to half the height of the domain. This is the maximum height of the boundary layer.

At the inlet boundary of the 2D model, the (thermal) boundary layer is equal to zero due to the uniform inlet conditions for both temperature and velocity. Figure 20b shows the uniform temperature at the inlet. This results in a higher heat transfer and, thus, a steeper temperature profile at the inlet of hot fluid, shown in Figure 20a. Since both fluids are streaming in opposite directions, the cold fluid at the outlet is influenced by the uniform inflow of the hot fluid. That also results in a steeper temperature profile of the cold fluid at its outlet boundary. The same pattern is shown at both ends of the heat exchanger.

The heat transfer rate can be derived with the bulk temperature profiles given in Figure 20a. The heat transfer rate of Case 1 for the different models is shown in Table 3. These rates are compared to the NTU and LMTD methods, described in Section 2.4.

Setup	Heat transfer rate [W]
2D model	1113.4
1D model	1064.2
NTU method	1064.6
LMTD method	1065.1

Table 3: The total heat flow rates for the 1D and 2D model, and LMTD and NTU method of Case 1.

According to the heat transfer rates, given in Table 3, it can be concluded that these are inequitable arrangements. The heat transfer rate of the 2D model is somewhat higher due to the uniform inlet velocity profile and the lack of a thermal boundary layer at the inlet boundary. The heat transfer rates of the NTU and LMTD methods are almost similar to the 1D model. Deviations can be attributed to the relative error of the mesh, explained in Section 3.1.8. For the selected 200 sections, the relative error is equal to 0.01% compared to the most refined mesh of 2000 sections. The relative error between the 1D and NTU & LMTD method is equal to 0.04%. That is in line with the relative error given for the mesh convergence study. So, although the NTU & LMTD-method are only indicative methods, it generally gives accurate results for the expected heat transfer.

The heat transfer rates of both domains are equal for the 1D model as long as it has a mesh that is fine enough and meets the mesh refinement requirements defined in Section 3.1.8. A coarser mesh has a larger deviation with the NTU & LMTD methods, which aligns with the relative errors in Figure 16a. The sum of heat flux over the heat exchange surface has computed the heat transfer rate of the 2D model. This value is different from the heat transfer rate of each domain. The total heat transfer rate of the hot fluid domain, based on the in and outlet bulk temperature and heat capacity, is equal to 1138 watts, while the cold fluid domain has a total heat transfer rate of 1169 watts. These rates have a relative difference of 2.5%, which cannot only be attributed to the relative error created by the mesh that is explained in Section 3.2.4. The thermal boundary layer causes this difference. The fluid flow has a higher heat transfer rate during the thermal entrance length since the flow is thermally not fully developed, which means that the insulating effect of the thermal boundary layer is lower [33]. Until the flow is fully developed, the temperature of the fluid that flows close to the wall is almost similar to the mean temperature of the flow and fluid that flows close to the adiabatic wall, shown in Figure 20b. As the flow develops, the temperature of the fluid adjacent to the heat transfer area drops faster than the mean temperature of the flow. That decreases the temperature difference with the fluid stream that flows adjacent to the other side of the wall, resulting in a lower heat transfer rate over the wall. The heat transferred to the adiabatic wall within the fluid stream and in the flow direction by diffusion and convection, respectively, causing a temperature profile shown in Figure 20b. So, the longer the entrance length, the higher the increase in the heat transfer rate. In this case, the thermal entrance length is longer for the cold fluid stream, resulting in a higher heat transfer rate than the hot fluid stream.

Both heat transfer rates are higher than the heat flux through the wall, given in Table 3. This heat flux represents the net heat flux through the heat exchange surface. As described, this net heat flux is mainly influenced by the flow adjacent to the heat transfer wall. The temperature difference between both sides of the wall is lower than the mean temperature difference of both flows, resulting in lower heat flux through the wall. The heat transfer rates of both domains are calculated based on the bulk temperatures, which incorporate the flow velocity. As the flow develops, the velocity close to the wall drops to zero while the velocity in the centre of the flow increases. This decreases the influence of these cells on the bulk temperature. The temperature of the cells in the centre of the domain becomes more dominant for the bulk temperature. Due to the relatively low flow velocity of the hot fluid, more heat is diffused from the adiabatic wall. Heat is also transferred from the adiabatic wall to the heat transfer wall. This results in a lower difference between the bulk temperature and the cell's temperature adjacent to the wall, shown in Figure 20b, and a higher heat transfer rate of the air-fluid stream compared to the net heat transfer rate. This transfer rate is lower due to a decreased temperature difference between both flows.

In this case, the heat transfer rate for the cold fluid stream is higher. This is thermodynamic incorrect because it is not possible to provide more heat to the cold fluid stream than generated by the hot fluid stream.

In case 1, heat is transferred between two water fluid streams. An air-fluid stream replaces one water-fluid stream within an air cooler. This stream's heat capacity and density are remarkably lower than the water stream. To create an observable temperature change within both models, the mass flow rates of both fluids have to be in the same range. Therefore, it is required to have a significantly higher inlet velocity. This influences the phenomena described before and, thus, the temperature profiles and heat transfer of the 2D model. These influences have been investigated by all other dry cases, cases 2-4. Figure 21 shows the (bulk) temperature profiles of both models for case 2, described in Table 1.

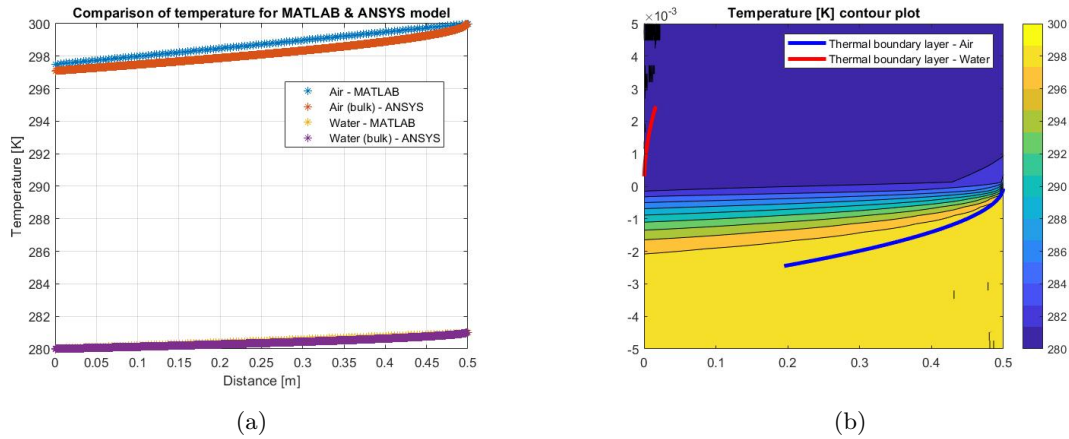


Figure 21: The temperature profiles of the ANSYS & MATLAB model for Case 2 with the bulk temperature (a) and the contour plot of the 2D model (b).

From Figure 21a can be concluded that the trends of the predicted bulk temperature profiles along both fluid streams are in fair agreement. The temperature profile for the air-fluid stream has more significant differences due to the higher inlet velocity. This influences the shape of the (thermal) boundary layer. A higher velocity, and lower density and dynamic viscosity result in an increased Reynolds number. As shown in Eq. 64, a fluid flow with a higher Reynolds number needs a larger distance from the leading edge to obtain the same thickness as the water flow stream that flows at a remarkably lower velocity. In other words, the entrance length of the fluid flow is longer. A larger distance is required until the fluid flow is fully-developed. As described before, a non-developed flow has a higher heat transfer rate. This results in a higher heat exchange rate and temperature decline of the bulk temperature in the air-fluid stream.

A higher inlet velocity also affects the heat transfer coefficient. This coefficient is kept constant within the 1D model. This means that an increase in inlet velocity for the air-fluid stream will not result in

a higher heat transfer coefficient. Especially for the airflow, in which a higher velocity is required to obtain the mass flow rate, this effect is more significant. The heat transfer rates, shown in Table 4, are also affected by this phenomena:

Setup	Heat transfer rate [W]
2D model	393.86
1D model	376.75
NTU method	376.90
LMTD method	377.45

Table 4: The total heat flow rates for the 1D and 2D model, and LMTD and NTU method of Case 2.

The thermal boundary layer of the 2D model is growing in thickness for half the length of the heat exchanger. From the leading edge to halfway through the heat exchanger, the thermal boundary layer has not have its maximum thickness. This results in a higher heat transfer coefficient for the nodes adjacent to the wall. Furthermore, the temperature gradient is higher in this part. The temperature difference between the wall and the centre of the domain remains the same. In contrast, the distance from the wall to the location where the temperature is almost equal to the mean temperature is smaller, as shown by the yellow part in Figure 21a. This distance increases over the length of the heat exchanger, resulting in a decrease in the heat transfer rate. The water flow has a (thermal) boundary layer which is more rapidly growing, which means that the flow has a fully-developed flow for a significantly larger part of the heat exchanger, shown in Figure 21b. This results in a lower mean heat transfer coefficient and conductive heat transfer rate, as explained by Case 1. Next to that, the absolute temperature difference for the water flow is always lower due to the water’s significantly higher thermal capacity. More heat is required to heat a similar amount of water than air. That results in a narrow temperature gradient in the vertical direction. The heat transfer rates of the NTU and LMTD methods are almost similar to the 1D model. The relative error between the 1D model and both methods equals 0.04%, which can be attributed to the relative error of the mesh.

The heat transfer rate for the 2D model, which is given in Table 4, is not equal to the heat transfer rate of both domains. The air domain’s total heat transfer rate equals 422 watts, while the water domain has a total heat transfer rate of 377 watts. This difference is also caused by a different thermal entrance length, which is explained by case 1. The net heat flux through the heat exchange surface, given in Table 4, is higher than the total heat transfer rate of the water domain but lower than its rate of the air domain. The water fluid stream’s thermal entrance length is remarkably shorter than for the air-fluid stream, shown in Figure 21b. This results in a lower heat transfer rate for the water fluid stream. The entire length is its flow developed, so the heat transfer rate is almost equal to the 1D model. The short entrance length and the higher heat transfer rate from the air-fluid stream cause the difference. The relatively long entrance length of the air-fluid stream results in a higher heat transfer rate. The net heat transfer rate is higher than the heat transfer rate of the water fluid stream. The transferred heat is almost not diffused within the water domain resulting in a small increase in the bulk temperature. The heat transfer rate of this domain is calculated with this temperature, resulting in a lower heat transfer rate.

Another influencing parameter is the heat exchange surface. The influence of this parameter on the difference between both models is shown in case 3. The heat exchange surface is ten times bigger compared to previous cases. In these cases, the influence of the heat transfer coefficient is significant in the difference between both models. This becomes more significant for larger heat exchange surfaces according to Eq. 6. To make a good comparison, the constant heat transfer coefficient of the 1D has been calculated based on the inlet velocity of the 2D model with Eqs. 6 and 7. The resulting heat transfer coefficients for the air and water flow stream are 8.3 and 33.5 W/m^2K , respectively, of the 1D model. Both models’ corresponding (bulk) temperature profiles for case 3 are given in figure 22.

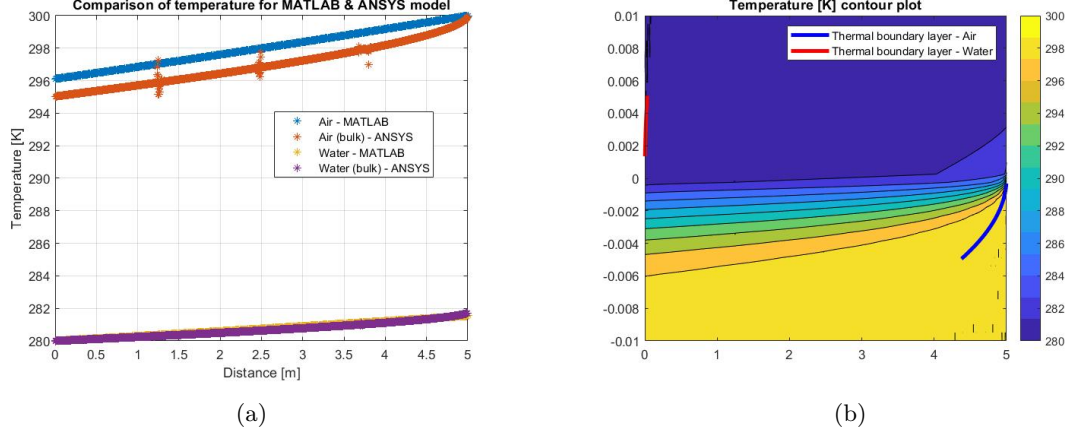


Figure 22: The temperature profiles of the ANSYS & MATLAB model for Case 3 with the bulk temperature (a) and the contour plot of the 2D model (b).

In Figure 21a, the predicted bulk temperature profile trend along the water stream is almost similar. Only close to the outlet boundary, between 4.5 and 5 metres, is the slope of the 2D temperature profile higher. The air temperature profiles also show this phenomenon. Like the first and second cases, the flow has a uniform velocity profile and temperature at the inlet boundary. Furthermore, there is no (thermal) boundary layer. Both phenomena increase the heat transfer rate and the slope of the temperature profiles. The air velocity is similar to the previous case, which results in a similar shape of the (thermal) boundary layer. But different from the previous case, the domain height is twice as large. That enables the (thermal) boundary layer to grow twice as big. The boundary layer grows thick for a distance from the leading edge of 0.6 metres. Within this length, the insulating effect is lower, and the difference between the bulk temperatures of the 1D and 2D model has been increased to 0.9 K, shown in Figure 21a. The bulk temperature profiles are almost parallel for the resulting 4.4 metres, in which the airflow transfers its heat to the water flow. Both profiles' differences are increased to 1.1 K at the outlet boundary (at a zero distance). This extra difference of 0.2 K results from using a constant heat transfer coefficient within the 1D model. These differences between the temperature profiles of both models also result in a difference in heat transfer rate. Table 5 shows these heat transfer rates.

Setup	Heat transfer rate [W]
2D model	646.86
1D model	574.24
NTU method	574.36
LMTD method	573.83

Table 5: The total heat flow rates for the 1D and 2D model, and LMTD and NTU method of Case 3.

The heat transfer rate of the 2D model is significantly higher due to the thermal boundary layer of the airflow, which has been described above. This net heat flux deviates from the heat fluxes of both domains, similar to the first and second cases. The air-fluid stream's thermal entrance length is longer, resulting in a higher heat transfer rate of 733 watts. The water-fluid stream has a relative short entrance length, which results in a heat transfer rate of 591 watts, close to the heat transfer rate of the 1D model. The net heat flux is lower than the heat transfer rate of the air-fluid stream due to the lower temperature difference of the cells close to the wall, described in case 1. The heat transfer rate of the water domain is lower than the net heat transfer rate due to the limiting diffusion rate of the heat. This limits the bulk temperature gradient and its heat transfer rate.

The heat transfer rates of the NTU and LMTD methods are almost similar to the 1D model. Deviations can be attributed to the relative error of the mesh, equal to 0.01%. The relative error between the 1D and NTU methods is equal to 0.02%, which aligns with the mesh convergence error.

The last case, case 4, has a similar heat transfer surface area but only a smaller temperature difference than case 3. Figure 35 in Appendix D.2 shows the temperature profiles. From these figures, the temperature difference has not a significant effect on the performance of both models. Similar deviations

between the 1D and 2D models for the (bulk) temperature profiles are shown. Furthermore, the heat transfer rates, shown in Table 18, show similar differences between the models.

4.3 Wet conditions

Air is considered dry air in cases 1 to 4, meaning that heat transfer is only driven by the temperature difference between two fluid streams. The relative humidity has been set to zero under these conditions. But in reality, the air always has a certain level of humidity. Decreasing its temperature results in another amount of water vapour it can contain. Colder air can contain less water vapour and becomes saturated with water vapour at a certain temperature. Further decrease in temperature results in condensation. Condensation of water vapour upon a cold surface involves the simultaneous transfer of heat and mass. These transfer flows are incorporated in case 5.

To model the condensation process, the 2D model has been extended with the volume of Fluid, which is described in Sections B.1. Governing equations describe the composition of the airflow with volume fractions. This means the bulk temperature can not be determined anymore since the fluid is not thoroughly mixed. Another method compares the temperatures of the 2D model along the flow direction of the channels along two lines with the 1D temperature profiles of the 1D MATLAB model [37]. A line parallel to the heat exchange surface is created in the middle of the height of the channels ($z=5$ mm). The lines are above and below the centerline of each channel by 1.5 mm, which is shown in Figure 23. These are non-averaged temperature profiles. The represented temperatures are the averaged temperatures of mesh cells located at this line.

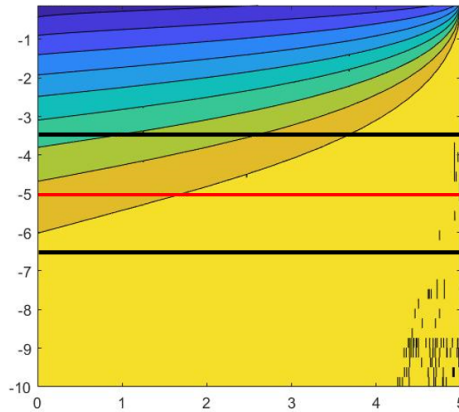


Figure 23: A schematic representation of the lines at which the air-fluid domain temperature profiles are computed. The red line represents the centerline, and the black lines represent the lines above and under the centerline.

The temperature of the water fluid stream can still be compared with the bulk temperature profile since this flow contains only liquid water, which means that it is thoroughly mixed. Figure 37 shows the computed temperatures along both channels by the 1D and 2D models for case 5, described in Table 1.

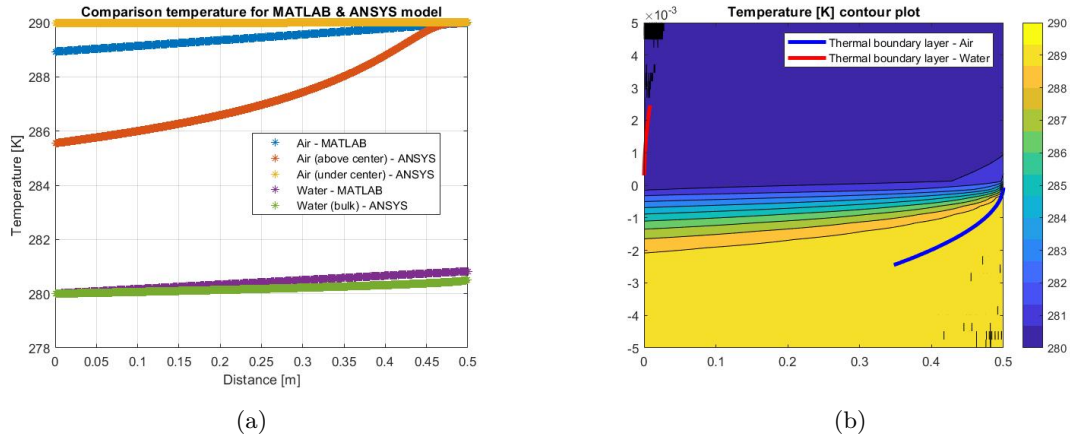


Figure 24: The temperature profiles of the ANSYS & MATLAB model for Case 5 with the temperature profiles (a) and the contour plot of the 2D model (b).

The lines above and below the centerline do not represent the bulk fluid stream, making it more difficult to compare. Only the bulk temperature profiles of the water fluid stream, shown in Figure 37, are comparable. Since the fraction of the water vapour or condensed liquid water is relatively low, shown in Figure 36b and 36c respectively, it can be assumed that the air-fluid is thoroughly mixed. That makes it possible to compare the bulk temperature of the air-fluid stream, shown in Figure 36a.

From Figure 36a can be concluded that the trend of the predicted bulk temperature profiles along both fluid streams does not match. The gradient in air temperature of the 2D model is higher. Close to the inlet boundary, the fluid flow has a uniform flow profile and a growing thermal boundary layer in thickness. This results in a higher heat transfer. The other differences caused by this are similar to case 2, explained in Section 4.2. This phenomenon affects the flow until 0.15 m from the leading edge, which is shown by the shape of the thermal boundary layer in Figure 24b. The difference in condensed water vapour declares the difference in the slope of the bulk temperature further away from the leading edge of the airflow. As explained before, condensation occurs if it is in contact with a surface beneath its dew point or if the air temperature itself drops beneath the dew point. According to the temperature contour of the 2D model, which is shown in Figure 24b, and the explanation about condensation, which is given in Appendix A, it can be expected that the shape of the liquid film is similar to the shape of the temperature contour with the highest values adjacent to the heat exchange surface. This phenomenon is visualized in the contour plot with the liquid volume fraction shown by Figure 36c.

Both models use the same expressions for the condensation mass flux, described in Section A. But there are also differences in the implementation. Within the 2D model, Eq. 74 is only applied on mesh cells adjacent to the heat exchange surface. All nodes within the 1D model are adjacent to the heat exchange surface, which means that it is applied on all mesh nodes. This difference in implementation results in a difference in condensation. This can be compared by looking at the total mass of condensed water vapour. For the 1D model, the condensation mass flux per unit area of individual sections is multiplied by the heat exchange surface of each section. Within the 2D model, this value can be computed by multiplying the volume fraction of liquid water of each cell by the cell volume and density of liquid water. The sum of all sections or cells is the total mass of condensed water vapour. The latent heat can be calculated by multiplying the mass with the values given in Eq. 24. The condensation values for both models are given in Table 6.

Setup	Condensed mass [kg]	Latent heat [W]
2D model	9.05e-7	2.04
1D model	3.70e-5	83.64

Table 6: The condensation mass flux and corresponding latent heat rates for the 1D and 2D model of Case 5.

According to the values given in Table 6 can be concluded that the condensation mass flux of the 2D model is remarkably lower than the condensation mass flux of the 1D model. This is the result of the

difference in implementation. The higher amount of latent heat of the 1D model increases the heat flux to the water fluid stream, resulting in a steeper slope for the bulk water temperature of the 1D model, shown in Figure 24a. The increased latent heat of the 1D model also decreases the temperature gradient of the air-fluid stream and affects the relative humidity. Air that has a higher temperature can contain a larger amount of water vapour and leads to a lower relative humidity. The increased condensation mass flux and a lower gradient of the bulk temperature for the air-fluid stream result in relative humidity that increases less for the 1D model. The profiles for the relative humidity, based on the bulk temperature, are shown in Figure 25.

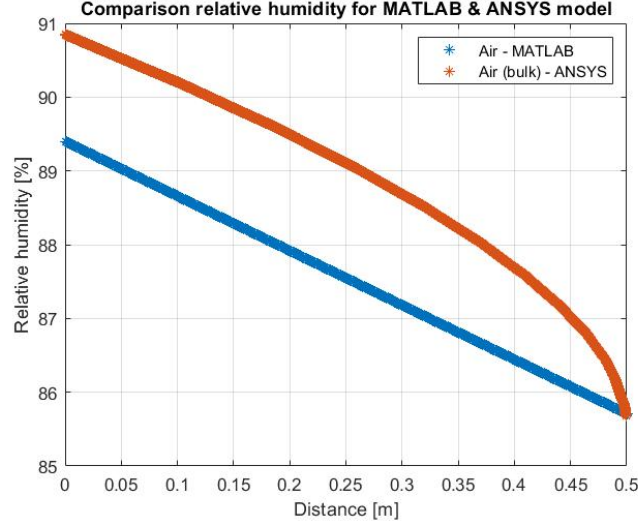


Figure 25: The relative humidity profiles of the ANSYS & MATLAB model for Case 5.

The profile for the relative humidity of the 2D model, shown in Figure 25, is not linear due to the non-linear bulk temperature profile, shown in Figure 36a.

The latent heat also affects the total heat transfer rate. It is next to the sensible heat transfer, a second heat flow. The heat transfer rates for both models and the NTU method are shown in Table 7.

Setup	Heat transfer rate [W]
2D model (Water)	96.73
2D model (Air)	105.81
1D model (Water)	164.60
1D model (Air)	81.05
NTU method	100.45
LMTD method	100.43

Table 7: The total heat flow rates for the 1D and 2D model, and NTU method of Case 5.

The heat transfer rates for the 1D model are defined for both domains in Table 7. These heat fluxes are equal for dry conditions but differ due to condensation for wet conditions. The difference between both heat fluxes equals the latent heat released by the condensation mass flux. This latent heat is transferred to both sides. In dry conditions, with a relative humidity of 0%, the heat transfer rate of the 1D model is equal to 100.5 watts. This means that 19.45 watts (23.3%) of the latent heat is used within the air domain, and 64.1 watts (76.7%) are transferred to the water domain. This heat flow results in a higher outlet water and air temperature, shown in Figure 36a.

The total heat transfer rate of the 2D model in the water domain is lower compared to the 1D model since there is less condensation within the 2D model. The difference between both heat fluxes is also not equal to the latent heat released by condensation, for the same reason explained by case 1. Comparing the heat fluxes of both domains to the heat fluxes during dry conditions should make it possible to say something about the fraction of the latent heat transferred to either side. Unlike the 1D model, this

comparison is more difficult due to the imbalance in heat transfer rates of both domains. The heat transfer flux for dry conditions in the air domain is equal to 109.39 watts and equal to 93.82 watts within the water domain. Both domains have a heat transfer rate for dry conditions that differs more than the value for the latent heat from the heat transfer rate for wet conditions, shown in table 7. This makes it impossible to calculate the fractions for the latent heat. It can only be said that the condensation mass flux decreases the heat flux by the airflow and increases the heat flux to the water flow. The net heat flux is increased from 102.8 watts for dry conditions to 104.0 watts for wet conditions, which means that 58% of the latent heat contributes to an increase in the net heat transfer rate. This also means that 58% of the latent heat is transferred to the water fluid stream, but not that the heat transfer rate of this fluid stream is increased with the amount of energy. That also depends on the diffusion rate of heat and, thus, the bulk temperature.

The NTU and LMTD methods can also be applied on condensers and evaporators by using Eq. 21, if the ratio for the heat capacity ($C_r = (\dot{m}C_p)_{min} / (\dot{m}C_p)_{max}$) is equal to zero. None of the heat capacity's within the 1D model is equal to zero, resulting in a difference in the heat exchange rates.

4.4 Frost conditions

Similar to the conditions applied in case 5, the relative humidity has been incorporated during frost conditions. This enables the water vapour to condense if the air becomes saturated due to decreased temperature or contact with a surface beneath its dew point temperature. The temperature for wet conditions is above the freezing point of water. If the surface temperature is beneath zero degrees Celsius and the saturation temperature of the surpassing air is higher than the surface temperature, the formation and growth of a frost layer can occur. This impedes the airflow and reduces the heat transfer rate. The influence of this frost layer build-up for both models has been investigated with case 6.

The 2D model, used in wet conditions, is extended with the solidification/melting model described in Section B.2. This model computes the liquid fraction within each computational cell, which determines the volume fraction of the cell that is solidified. The volume fraction of frost within each cell can be computed with the following expression:

$$X_f = (1 - \beta) * X_l \quad (66)$$

in which X_f is the volume fraction of the solidified liquid water, X_l is the volume fraction of the combined liquid and solidified water, and β is the liquid fraction. This is the volume fraction of the amount of liquid/solid water that is in liquid form.

Similar to wet conditions, the bulk temperature cannot be used within the air-fluid domain since it is not thoroughly mixed. The method with temperature profile lines above and under the centerline is used to compare the 2D temperature profile with the results of the 1D model. Due to the formation of the frost layer, the air-flow is impeded. Therefore, a similar assumption, which is done by the wet cases, cannot be made.

Both models are modelled with a transient simulation. The frost builds up over time and disturbs the airflow, which is explained in Section 3. The models simulate this process for 500 seconds with a time step size chosen so that the Courant number equals one. Models have been compared at ten seconds. Figure 26 shows the computed temperatures along both channels by the 1D and 2D models for case 6 at 10 seconds, described in Table 1.

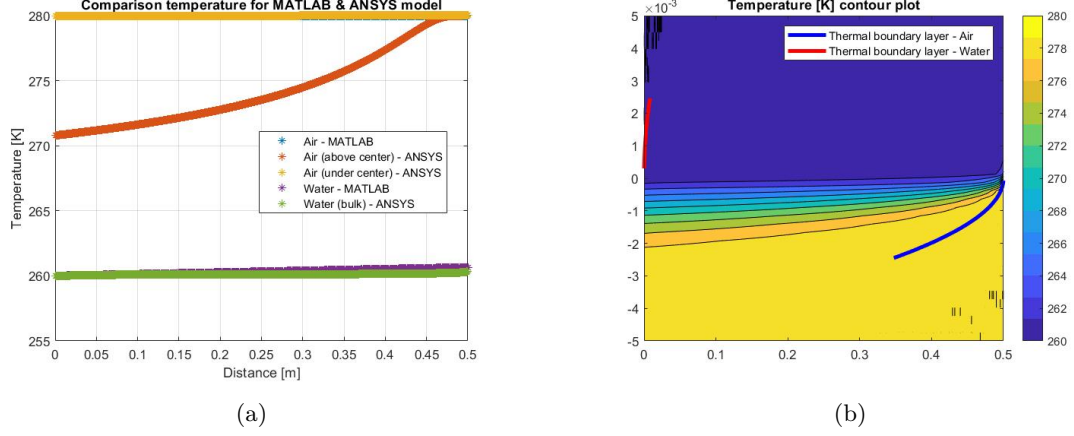


Figure 26: The temperature profiles of the ANSYS & MATLAB model for Case 6 with the temperature profiles (a) and the contour plot of the 2D model (b) at ten seconds.

The temperature profiles for the air-fluid stream, shown in Figure 26a, are difficult to compare. The bulk temperatures of the water fluid domain of both models, shown in Figure 26a, shows no corresponding profile. The water temperature of the 2D model stays almost constant over the heat exchanger, while the 1D model shows a slight increase in temperature. Nearly a similar difference is shown for the airflow temperature. The slope of the corresponding temperature profile for the 1D model is almost equal to zero. The air temperature profile above the centerline has an increasing slope until 0.15 m of the leading edge, which becomes constant further downstream. The air temperature decreases linearly in this stage of the heat exchanger. Several reasons cause this difference. First, the inflow velocity profile is uniform, and the thickness of the (thermal) boundary layer slightly increases until a distance of 0.15 m from the leading edge. Secondly, the condensation and deposition mass flow differ between the two models. There are some differences in implementing the condensation model described by the explanation of case 5 in Section 4.3. This difference also influences the composition of the volume fractions. Within the 2D model, a liquid water film is formed on the frost layer, shown in Figure 37c. The water vapour does not have to deposit if the surface temperature is below freezing point. The phase transition is based on the temperature in the computational cell and the diffusion rate of liquid water within the frost layer. The phase transition within the 1D model is based on the surface temperature. All water vapour that condenses will contribute to the frost layer if the surface temperature of the section is below the freezing point. A surface temperature above the freezing point forms only a liquid water film. So a combination of both phases is not possible within a section of the 1D model.

The latent heat due to the phase change of the 1D model can be calculated by multiplying the mass flux per unit area with the area of each section and the latent heat. The value for the latent heat of frost formation is given by Eq. 24. The total amount of latent heat can be calculated with the following equation:

$$Q_{lat} = \sum_i^k m''_{i,t} A_i L \quad (67)$$

Within the 2D model, a distinction between the contribution of the liquid and solid phases to the latent heat has to be made since both phases are formed within the heat exchanger. The total amount of latent heat per phase can be calculated by the following equations for respectively the liquid and solid phases:

$$Q_{lat,l} = \sum_i^k \beta X_l A_i \rho_f L \quad (68)$$

$$Q_{lat,f} = \sum_i^k X_f A_i \rho_f L \quad (69)$$

The latent heat values for both models are given in Table 8.

Setup	Condensed mass [kg]	Frozen mass [kg]	Total latent heat [W]
2D model	1.4186e-7	1.1724e-6	3.36
1D model	0	4.7131e-5	122.16

Table 8: The condensation & deposition mass flux and corresponding latent heat rates for the 1D and 2D model of Case 6.

According to the values given in Table 8 can be concluded that the condensation mass flux of the 2D model is remarkably lower. This is the result of the difference in the implementation that is described before. The bulk temperature profiles are also affected by the latent heat difference. An increased latent heat reduces the air temperature to drop along the heat exchanger. Furthermore, the frost layer is an insulation layer for the heat exchange to the water fluid stream. This decreases the temperature gradient of the water fluid stream, which is remarkably lower than for a situation with only condensation, shown in Figure 24a. The frost layer formation does not influence the air bulk temperature for the 2D model, since it continues to decrease as the frost layer grows. This is shown in Figure 27b. The corresponding relative humidity profile, shown in Figure 27a, is mainly influenced by the temperature profile due to the low amount of water vapour that condenses or freezes. The relative humidity profile of the 1D model, shown by the blue line in Figure 27a, decreases due to the formation of the frost layer and a constant air temperature.

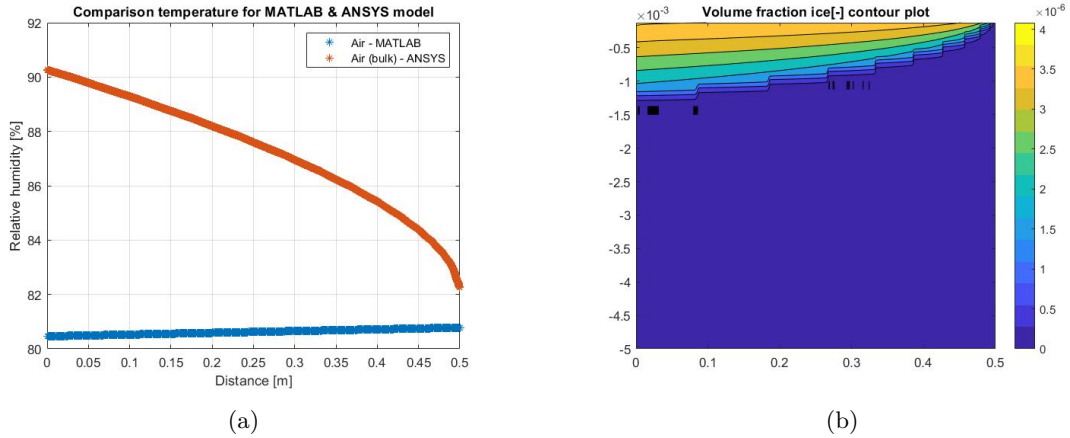


Figure 27: The relative humidity profiles of the ANSYS & MATLAB model (a) and contour plot of the volume fraction ice for the 2D model (b) at ten seconds.

The shape of the solid film, shown by Figure 27b, has a similar shape to the temperature contour with the highest values adjacent to the heat exchange surface since the condensation/deposition mass flux is dependent on the air temperature. Water vapour condenses/de-sublimates due to decreased air temperature beneath its dew point. A higher decrease in temperature close to the wall generally results in a higher amount of condensation/deposition. Furthermore, the air temperature has to be below the freezing point for frost formation. This is only the case close to the wall.

The latent heat and formation of the frost layer also affect the total heat transfer rate. The heat transfer resistance increases as the frost layer grow in thickness, shown by Eq. 27. This has a negative effect on the amount of heat that is transferred to the water fluid stream. The heat transfer rates for both models and the NTU method are shown in Table 9.

Setup	Heat transfer rate [W]
2D model (Water)	175.05
2D model (Air)	220.34
1D model (Water)	126.34
1D model (Air)	4.43
NTU method	192.63
LMTD method	208.14

Table 9: The total heat flow rates for the 1D and 2D model, and NTU method of Case 6.

The deposition and condensation mass flux also influence the heat flux balance during frost, shown in Table 9. The difference between the heat transfer rates on both domains for the 1D model equals the value for the latent heat. The formed frost layer reduces the heat transferred to the water domain. In dry conditions, the heat transfer rate of the 1D model is equal to 192.64 watts. That means that the insulating effect of the frost layer decreases the total heat transfer rate by 34.4%. This frost layer, which acts as an insulation layer, also affects the heat transfer rate of the air-fluid stream by 97.7%. This results in a lower temperature gradient of this fluid stream over the heat exchanger. The latent heat of the 1D model, shown in table 8, contributes almost 96.5% to the total heat transfer rate to the water fluid stream. Overall, the outflow temperature for the water-fluid stream is lower, while the outflow temperature for the air-fluid stream is higher. This decreases the effectiveness of the entire heat exchanger.

The total heat transfer rate to the water domain is lower for the 2D model since the condensation/deposition mass flow rate is lower. This also results in a heat transfer rate of the air side for the 2D model, which is significantly higher than the 1D model. As explained before, the latent heat is partly transferred to the air-fluid stream, resulting in a lower heat transfer rate value. This effect is lower for the 2D model since the released latent heat is significantly lower, resulting in a higher heat transfer rate. The difference between both domain heat transfer rates is larger than the value for the latent heat, which is given in table 9. This is caused by the difference in the thermal boundary layer, explained by case one. Therefore, these heat transfer rates are unusable to conclude the effect of the condensation/deposition mass flow. Comparing the net heat flux rate to show the effect of frost formation on the heat exchanger performances is better. Due to the frost formation, the net heat transfer increases from 134.63 watts to 217.79 watts. That means the condensation/deposition mass flow rate increases the net heat transfer by 61.8%. This effect differs from the 1D model, where the frost layer decreases the net mass flow rate. Different modelling approaches could declare this difference. The 1D model has a fully solidified frost layer that acts like an insulation layer. In contrast, the 2D model has a frost layer with a maximum porosity fraction of $4e-6$, shown in Figure 27b. This layer is not an insulation layer but provides an extra net heat transfer to the water domain. The increase in net heat transfer is higher than the total latent heat, shown in Table 8, which a density difference could cause. The density does increase due to the condensation and deposition phenomena close to the wall. An increase in the density results in an increased heat transfer coefficient, according to Eqs. 6 and 7. The temperature also influences the thermal conductivity, but this value is kept constant within the 2D model. This increases the heat transfer rate if the velocity remains constant. Furthermore, the condensation mass flux makes the model more complex, which could affect the stability of the result. That could also influence the difference between the heat transfer rates.

The heat transfer rate of the water fluid stream for the 2D model is increased from 106.94 watts, by dry conditions, to 175.05 watts by frost conditions. The increased net heat transfer rate probably causes this difference. The thermal entrance length is similar for both conditions, so that could not be the reason for this difference. The heat transfer rate of the air-fluid stream is almost the same, 220.63 watts for dry conditions and 220.43 watts for frost conditions. This value is almost not influenced due to the relatively low latent heat.

As explained in Section 4.3, the NTU and LMTD methods can also be applied to condensers and evaporators by using Eq. 21, if the ratio for the heat capacity ($C_r = (\dot{m}C_p)_{min} / (\dot{m}C_p)_{max}$) is equal to zero. None of the heat capacity's within the 1D model is equal to zero, resulting in a difference in the heat exchange rates. The heat transfer rate for the NTU method almost equals the heat transfer rate for dry conditions, 192.64 watts. The heat transfer rate of the LMTD method is affected by the outlet temperatures of the 1D model. The NTU method is independent of outflow temperatures. This heat transfer rate is higher since these outlet temperatures result in a larger log-mean temperature difference. Both methods have a higher rate than both models due to the insulating effect of the frost layer, which is not included in both methods.

5 Results

In this chapter, the results of all models are presented to describe the influence of different parameters on the performance of the heat exchanger. The performance is compared for three situations: dry, wet and frost. The results in section 4 describe the difference between both models and the LMTD & NTU method. The domain length, height, and temperature differences varied for dry conditions. The relative humidity and temperature difference are varied for wet and frost conditions. All cases are presented in Table 10. Some are similar to the case presented in section 4. The results are shown in Appendix E.

Case number	Domain height [mm]	Heat exchange area [m^2]	Mass flow air [kg/s]	Relative Humidity [-]	Air temperature [K]	Mass flow water [kg/s]	Water temperature [K]
Case 1*	10	0.5	0.147	0.0	300	0.098	280
Case 2*	10	5	0.147	0.0	300	0.098	280
Case 3*	10	5	0.147	0.0	290	0.098	280
Case 4*	5	0.5	0.019 (water)	0.0	290	0.072	280
Case 5*	10	5	0.019 (water)	0.0	290	0.072	280
Case 6*	14	5	0.019 (water)	0.0	290	0.072	280
Case 7*	5	0.5	0.0735	64.2	290	0.0499	280
Case 8*	5	0.5	0.0735	85.7	290	0.0499	280
Case 9*	5	0.5	0.0735	85.7	300	0.0499	280
Case 10	5	0.5	0.0735	61.7	280	0.0499	260
Case 11	5	0.5	0.0735	87.6	280	0.0499	260
Case 12	5	0.5	0.0735	87.6	300	0.0499	260

Table 10: Conditions of the various setups to express the influence of these conditions. *steady-state cases

The physical properties of the substances used within these cases are described in Table 2. The wall separating the air and water flow has a constant thickness of 0 mm and is made of stainless steel, similar to the cases presented within section 4.

5.1 Dry conditions

In this section, the steady state results of both models are presented for cases one - six. The domain length, height, and temperature differences are varied in these cases. Other variables are kept constant. The effectiveness of each case indicates the efficiency of the heat exchanger. The effectiveness measures the ratio of the heat transferred in the heat exchanger to the maximum possible heat transfer in a heat exchanger geometry. This value can be computed with Eq. 20. The bulk temperature profiles, heat exchange coefficient and heat transfer rates are also given for each parameter variation.

5.1.1 Temperature difference

The temperature difference between the two fluid streams is the driving force for heat transfer within the heat exchanger in dry conditions. Heat flows from a fluid with a higher temperature to a fluid with a lower temperature. The larger the temperature difference, the higher the heat flow, according to the equations of both models. Cases 2 and 3 are used to investigate the influence of the temperature difference. These cases have a temperature difference of 10 and 20 Kelvin. The inlet temperature of the water fluid stream is equal to 280 Kelvin for both cases, while the inlet temperature of the air-fluid stream is changed from 290 to 300 Kelvin. Other parameters, like the heat exchange surface area and mass flows, are kept constant. Figure 28 shows the governing bulk temperature profiles.

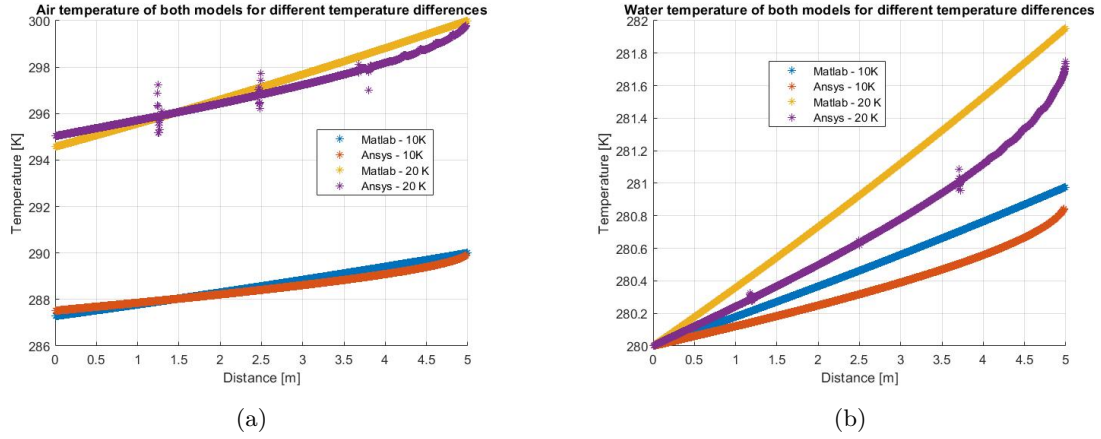


Figure 28: The bulk temperature profiles of the ANSYS & MATLAB model for Cases 2 & 3. Results of the air domain (a) and water domain (b).

According to the temperature profiles shown in Figure 28 is the temperature gradient for both fluid streams higher as the inlet temperature difference increases. The outlet temperature for the water fluid stream is increased from 0.8-1 Kelvin to 1.8-1.9 Kelvin depending on the model. The temperature difference of the air-fluid stream between in and outlet is increased from 2.5-2.7 Kelvin to 5-5.4 Kelvin depending on the model. Approximately this means that doubling the inlet temperature difference results in an increase in temperature gradient by a factor of two. Thus, the ratio between the actual and maximum heat transfer, the efficiency (or effectiveness), remains almost constant, shown in Table 11.

Temperature difference	10	20
Effectiveness	0.272	0.265
Heat exchange rate - NTU	400.54	786.35
Heat exchange rate - LMTD	400.58	786.86
LMTD	9.34	18.34
Heat exchange rate - 1D	400.41	785.23
Heat exchange rate - 2D	407.23	739.47
Heat transfer coefficient - air	11.69	11.34
Heat transfer coefficient - water	64.29	64.29

Table 11: The performance indicators of the heat exchanger for a temperature difference of 10 K and 20 K. The temperature difference is given in Kelvin, heat exchange rates are given in Watts, and the heat transfer coefficient is given in $[W.m^{-2}.K^{-1}]$. These are the mean heat transfer coefficients used in the 1D model. The heat transfer coefficient of the 2D model varies over the heat exchanger.

The values shown in Table 11 align with the bulk temperature profiles shown in Figure 28. The mean heat transfer coefficients remain almost constant due to a similar inlet velocity and height. A small decrease in the air-fluid stream's heat transfer coefficient results from a lower density. The heat transfer coefficient deviation also leads to a slight decrease in the effectiveness. All models' resulting heat transfer rates do not increase by a factor of 2 if the temperature difference, thus the maximum heat transfer, doubles.

5.1.2 Domain height

The domain height influences the inlet velocity of both fluid streams as the mass flow rates are kept constant. The inlet velocity increases inversely proportional to the domain height. This leads to an increase in the heat transfer coefficient since this coefficient is dependent on the Reynolds number and, thus, the velocity, according to the relation for the Nusselt number, given by Eq. 6. Cases 4, 5, and 6 are used to investigate the influence of the domain height. Within these cases, both flows contain a water-fluid stream. The mass flow rates and inlet temperatures are kept constant for each case. Only the domain height is changed to 5, 10, and 14 millimetres within cases 4, 5, and 6, respectively. Figure 28 shows the governing bulk temperature profiles.

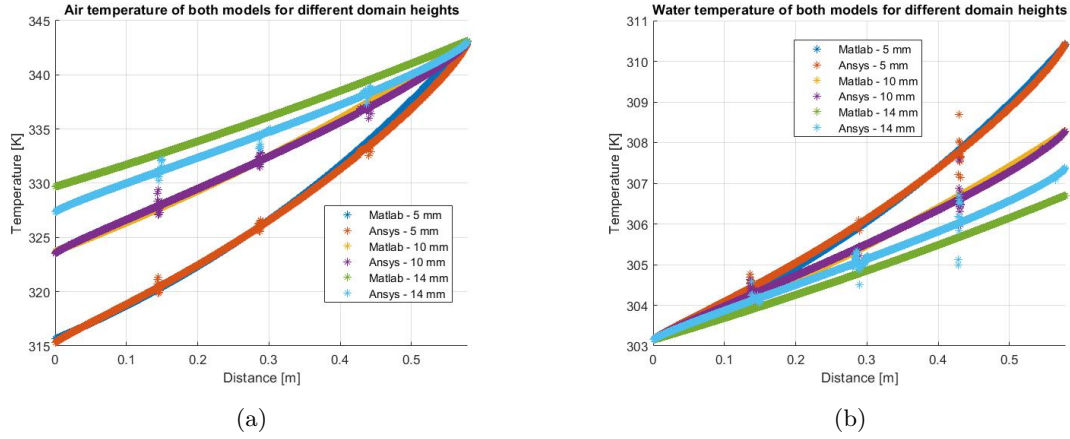


Figure 29: The bulk temperature profiles of the ANSYS & MATLAB model for Cases 4, 5 & 6. Results of the air domain (a) and water domain (b).

The temperature profiles, shown in Figure 29, show an increase in both temperature gradients as the domain height decreases. An increased heat transfer coefficient drives this increase. This coefficient is approximately 1.8 times higher for a decrease in domain height by a factor of two, from ten to five millimetres. These coefficients are shown in Table 12.

Domain height	5	10	14
Effectiveness	0.69	0.49	0.34
Heat exchange rate - NTU	2187.15	1545.07	1068.10
Heat exchange rate - LMTD	2187.71	1545.35	1067.75
LMTD	21.00	27.09	31.23
Heat exchange rate - 1D	2186.80	1544.69	1069.43
Heat exchange rate - 2D	2210.94	1558.37	1113.40
Heat transfer coefficient - air	303.43	166.20	50.48
Heat transfer coefficient - water	441.86	242.02	73.51

Table 12: The performance indicators of the heat exchanger for a domain height of 5, 10, and 14 mm. The domain heights are given in millimeters, heat exchange rates are given in Watts, and the heat transfer coefficient is given in $[W.m^{-2}.K^{-1}]$.

The heat transfer coefficient, shown in Table 12, increases the heat transfer rate. This increase is lower due to the thermal boundary layer and the temperature difference. A decrease in domain height affects the growth of this layer. The distance from the leading edge to a full-growth thermal boundary layer is lower, negatively affecting the heat transfer rate. Furthermore, the temperature difference between the two fluid flows is lower. The bulk temperature plots, shown in Figures 41a, 42a and 43a, show that the log-mean temperature difference decreases with the domain height, which is also shown in Table 12. This difference is the driving force for heat transfer. A decrease in the log-mean temperature difference has a negative effect on the heat transfer rate, governed by Eq. 15. This results in a smaller difference between the heat transfer rates than expected from the ratio of the heat exchange coefficients. But the heat transfer rate increase leads to the heat exchanger's higher efficiency or effectiveness, as shown in Table 12. The maximum heat transfer remains constant while the actual heat transfer is increased for a smaller domain height. Concluding, a decrease in domain height results in a higher heat transfer rate and efficiency of the heat exchanger.

5.1.3 Domain length

The domain length determines the size of the heat transfer area. This is where heat can be transferred between the two fluids. The 2D model has a default depth of 1 meter, meaning the heat transfer area scales linearly with the domain length. This is similar to the 1D model. The sum of the area of all individual sections, considered by the energy balance of Eq. ??, equals the heat transfer area of the entire heat exchanger. Cases 1 and 2 are used to investigate the influence of the domain length. Case 1 has a heat transfer area of $0.5 m^2$ while case 2 has a heat transfer area of $5 m^2$. The mass flow rates,

inlet temperatures, and domain height are equal for both cases.

The bulk temperatures are expressed along the domain length. Therefore, the bulk temperature profiles can not be compared within one figure. The bulk temperature profiles of both cases are shown in Figures 38a and 39a. These figures show that the difference between the in and outlet temperatures is bigger for the case with a longer domain length, which could be expected from the energy balance of the 1D model, Eq. 43, 44 and 45. This also results in a higher heat transfer rate, shown in Table 13.

Domain length	0.5	5
Effectiveness	0.10	0.27
Heat exchange rate - NTU	292.25	801.08
Heat exchange rate - LMTD	292.26	801.16
LMTD	18.65	16.25
Heat exchange rate - 1D	292.13	800.82
Heat exchange rate - 2D	393.86	739.47
Heat transfer coefficient - air	37.03	11.65
Heat transfer coefficient - water	204.30	64.29

Table 13: The performance indicators of the heat exchanger for a domain length of 0.5 and five meters. The domain lengths are given in meters, heat exchange rates are given in Watts, and the heat transfer coefficient is given in $[\text{W}\cdot\text{m}^{-2}\cdot\text{K}^{-1}]$.

According to the heat transfer rates in Table 13, the heat transfer area influences the total amount of heat transferred. This rate increases if the heat transfer area is increased. But this heat exchanger’s heat transfer rate per unit area is lower due to the lower log-mean temperature difference and heat transfer coefficient. The global temperature difference between the two fluid streams determines the log-mean temperature. This difference decreases over the length of the heat exchanger since heat is transferred. This means that the global temperature difference decreases if more heat is transferred. The mean heat transfer coefficient is also lower for the heat exchanger with a longer domain length. This coefficient decreases as the distance from the leading edge increases. The total and mean distance is larger for the case with a domain length of 5 meters, resulting in a lower mean heat transfer coefficient. This coefficient is used as a constant within the 1D model.

Nevertheless, the effectiveness of the heat exchanger is higher for the larger heat exchanger. This performance parameter is determined by the actual heat transfer rate, which is higher for the larger heat exchanger, and the maximum heat transfer rate, which is similar for both cases. The maximum heat transfer rate is only influenced by the mass flow rate and inlet temperatures, which are similar for both cases. Therefore, this parameter needs to be computed per unit area. The effectiveness per unit area is higher for the smaller heat exchanger since this heat exchanger’s actual heat transfer rate per unit area is higher.

5.2 Wet conditions

The air-fluid stream considered within the dry conditions has a relative humidity equal to zero. Heat is only transferred due to the temperature difference between both fluid streams. The models described within Section 3 also consider an extra heat flow due to the condensation of water vapour. Therefore, the relative humidity within the 1D model or vapour volume fraction within the 2D model is defined at the inlet of the air-fluid stream. This parameter changes over the length of the heat exchanger due to condensation and a temperature difference. The condensation mass flux is an extra heat source influencing the bulk temperature of both fluid streams. Since the fraction of the water vapour or condensed liquid water is relatively low, as shown in Figures 44c and 44d, respectively, it can be assumed that the air-fluid is thoroughly mixed, similar to the cases presented in Section 4.3. That makes it possible to compare the bulk temperature of the air-fluid stream.

In this section, the steady state results of both models are presented for cases seven - nine. Within these cases, the inlet temperatures and humidity are varied. Other variables are kept constant. Next to the performance parameters given in Section 5.1 are the condensation mass flux and relative humidity incorporated within the comparison between both models. Furthermore, the air-fluid stream consists of several phases. For these fluid streams, the equation for the effectiveness, which is used during dry

conditions, is not applicable. In case of a phase change, is the effectiveness given by Eq. 21.

5.2.1 Temperature difference

The temperature difference is not the only heat source within an air-fluid stream with a certain humidity. Also, the latent heat, released due to condensation, influences the heat transfer and the temperature of both fluid streams. This condensation mass flux results from the air that drops below its dew point temperature. So, the temperature difference also influences the amount of water vapour that condenses. The influence of this temperature difference on all parameters is investigated in cases 8 and 9. These cases have a temperature difference of 10 and 20 Kelvin. The inlet temperature of the water fluid stream is equal to 280 Kelvin for both cases, while the inlet temperature of the air-fluid stream is changed from 290 to 300 Kelvin. Figure 30 shows the governing bulk temperature profiles and relative humidity profiles.

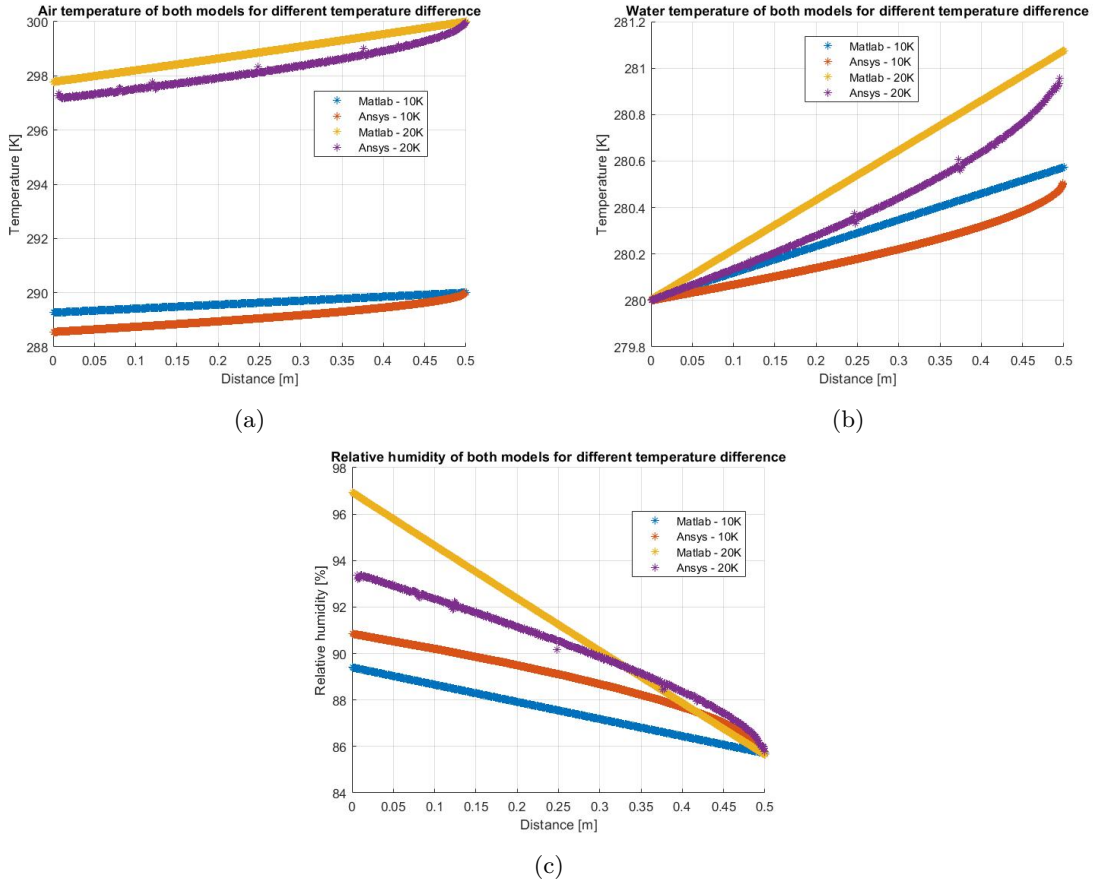


Figure 30: The bulk profiles of the ANSYS & MATLAB model for Cases 8 & 9. Results of the temperature in air domain (a) and water domain (b), and relative humidity (c).

The bulk temperature and relative humidity profiles in Figure 30 show a higher temperature gradient for the case with a temperature difference of 20 Kelvin. The temperature difference of the water-fluid stream is increased by 83-100%, depending on the model. For the air-fluid stream, the temperature difference is increased by 68 - 100%. This increases the value for the log-mean temperature by a factor of two, shown in Table 14. This means that the ratio between the actual and maximum heat transfer remains constant, similar to the comparison for dry conditions. The temperature difference also influences the relative humidity, shown in Figure 30c. Especially the 1D model shows large deviations. The relative humidity is further increased due to the larger temperature difference. As mentioned before, the relative humidity is influenced by the bulk temperature profile. This profile is linear, leading to a linear profile for the relative humidity. The profile for the 2D model is also equal to the trend of the corresponding temperature profile, shown in Figure 30a. The difference in the relative humidity for both cases is remarkably lower in the 2D model, shown in Figure 30c. This is probably the result of the lower condensation heat flux compared to the 1D model. Table 14 shows the condensation heat flux. Figure

30 shows profiles for the 2D model with a temperature difference of 20 Kelvin with points that deviate from the trend. This could indicate unstable results, which will be explained further within Section 6.

Temperature difference	10	20
Effectiveness	0.10	0.10
Heat exchange rate - NTU	73.84	147.72
Heat exchange rate - LMTD	74.08	145.42
LMTD	9.34	18.34
Heat exchange rate - 1D (water)	127.19	321.51
Heat exchange rate - 1D (air)	62.69	113.36
Heat exchange rate - 1D (condensation)	64.54	208.15
Heat exchange rate - 1D (net)	127.26	321.67
Heat exchange rate - 2D (water)	105.07	286.60
Heat exchange rate - 2D (air)	105.22	391.33
Heat exchange rate - 2D (condensation)	2.57	11.33
Heat exchange rate - 2D (net)	104.00	285.21
Heat transfer coefficient - air	36.63	36.58
Heat transfer coefficient - water	203.32	203.32

Table 14: The performance indicators of the heat exchanger for a temperature difference of 10 and 20 Kelvin. The temperature difference is given in Kelvin, heat exchange rates are given in Watts, and the heat transfer coefficient is given in $[\text{W}\cdot\text{m}^{-2}\cdot\text{K}^{-1}]$.

The change in temperature difference between both fluid domains does not increase the effectiveness, according to Table 14. The inlet mass flow rate and heat transfer coefficient influence the effectiveness according to the equation for the NTU, Eq. 19. Both parameters are almost not changed, which results in constant effectiveness. Nevertheless, the heat transfer rates are higher for a larger temperature difference. These scales almost proportionally for the heat transfer rates of NTU and LMTD, in which the condensation mass flux is not incorporated. These mass fluxes are increased due to a larger temperature decline by approximately a factor of 4 for both models. This results in a higher net heat transfer rate and heat transfer rate for both domains, increasing by a factor of 3. That should increase effectiveness since the heat input, the maximum amount of heat transfer, is doubled, and the heat output is more than doubled.

5.2.2 Humidity

The humidity at the inlet boundary of the air-fluid stream influences the amount of water vapour that condenses within the heat exchanger. Condensation takes place if the air decreases beneath its dew point temperature. The higher the initial relative humidity, the higher the dew point temperature. This increases the condensation mass flux and influences both fluid temperatures and heat fluxes. The humidity's influence at the air-fluid stream's inlet boundary is investigated in cases 7 and 8. The cases have an initial relative humidity of 61.7% and 85.7%, respectively. Figure 31 shows the governing bulk temperature profiles and relative humidity profiles.

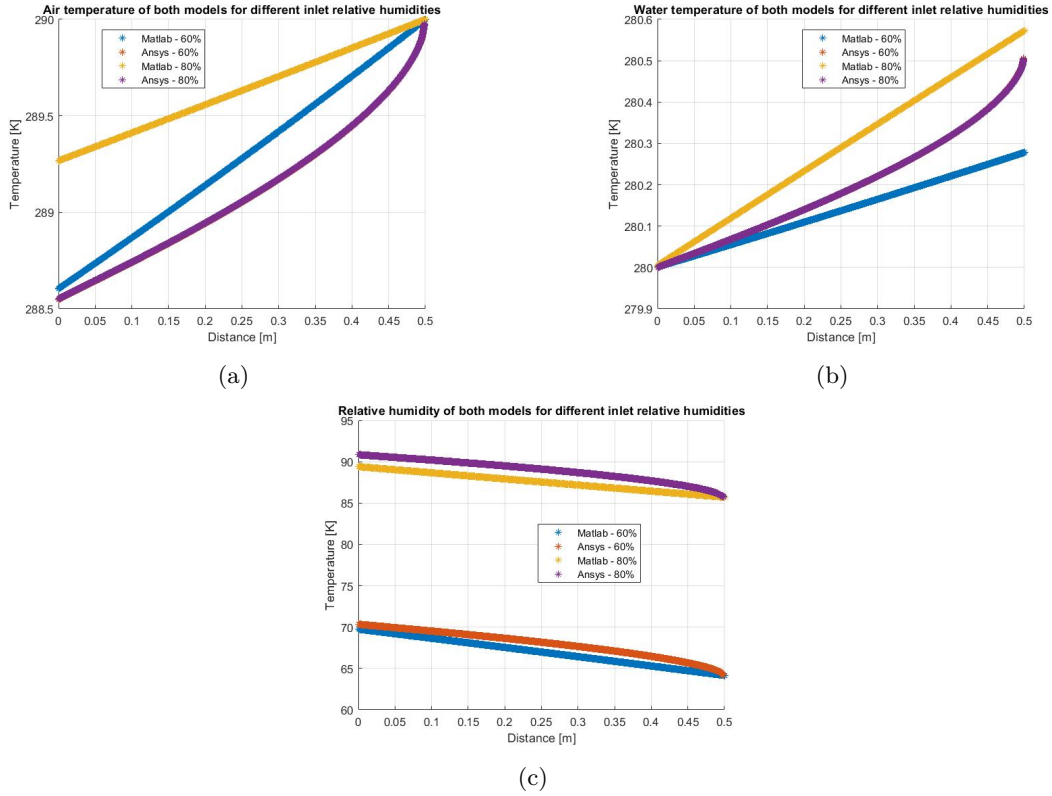


Figure 31: The bulk profiles of the ANSYS & MATLAB model for Cases 7 & 8. Results of the temperature in air domain (a) and water domain (b), and relative humidity (c).

The bulk profiles of Figure 31 show the influence of the relative humidity. Especially for the 1D model, the difference is visible. An increase in relative humidity results in a lower gradient for the air temperature. A fraction of the heat released by the condensation mass flux is transferred to the air domain, resulting in a lower temperature gradient if more water vapour is condensed. The resulting latent heat is transferred to the water fluid stream. This leads to an increase in the net heat transfer and water temperature gradient. This result is remarkably smaller for the 2D model since a significantly lower amount of water vapour is condensed within this model. The differences between both models are explained in Section 4. These differences are also shown in the performance parameters by Table 15

Relative humidity	61.7	85.7
Effectiveness	0.10	0.10
Heat exchange rate - NTU	73.87	73.54
Heat exchange rate - LMTD	72.55	74.08
LMTD	9.15	9.35
Heat exchange rate - 1D (water)	80.74	127.19
Heat exchange rate - 1D (air)	71.01	62.69
Heat exchange rate - 1D (condensation)	9.74	64.54
Heat exchange rate - 1D (net)	80.78	127.26
Heat exchange rate - 2D (water)	105.46	105.07
Heat exchange rate - 2D (air)	105.22	105.22
Heat exchange rate - 2D (condensation)	0.22	2.57
Heat exchange rate - 2D (net)	107.59	104.00
Heat transfer coefficient - air	36.69	36.63
Heat transfer coefficient - water	203.32	203.32

Table 15: The performance indicators of the heat exchanger for a relative humidity at the inlet boundary of 61.7% and 85.7%. The temperature difference is given in Kelvin, heat exchange rates are given in Watts, and the heat transfer coefficient is given in $[W.m^{-2}.K^{-1}]$.

The difference between the latent heat of both models, shown in Table 15, is significant. A higher relative humidity at the inlet leads to increased water vapour that condenses, resulting in a larger condensation heat transfer rate. This results in a lower heat transfer rate for the air-fluid stream but increases the heat transfer rate through the wall and the water-fluid stream. The heat transfer coefficients are only slightly changed due to a difference in density. Air containing a larger fraction of water vapour is lighter, resulting in a lower heat transfer coefficient. The heat transfer coefficient of the water-fluid stream is not influenced, resulting in a similar value for effectiveness. Nevertheless, the heat transfer rates of the 1D model are increased for a higher relative humidity value. An increase in relative humidity by a factor of approximately 1.4 leads to an increase in heat transfer by a factor of 1.6. The 2D model shows barely any differences due to the relatively low amount of water vapour that has been condensed.

5.3 Frost conditions

The relative humidity is also incorporated during frost conditions. In this situation, the water vapour cannot only change into the liquid phase but also into the solid phase. This means that two different phase changes are taken into account. The phase change from liquid to solid can occur if the cell's temperature is below and the saturation temperature is above the freezing point of water. The 1D and 2D models modelled the frost layer differently, described in Section 3. Heat is released during the formation of this layer, which also acts as an extra insulation layer between the water and air-fluid streams.

In this section, the transient results of both models are presented for cases ten - twelve. Within these cases, the inlet temperatures and humidity are varied. Other variables are kept constant. Similar to wet conditions, the air-fluid stream consists of several phases. For these fluid streams, the effectiveness given by Eq. 21. The results are given at three different times: 10, 100 and 1800 seconds.

The bulk temperatures of the air-fluid stream are compared. This approach is different from the frost cases presented in Section 4.4. The frost growth impedes the air-flow, but this influence is limited. The frost layer is modelled as a porous medium. The porosity is relatively high, which is shown by Figures 48g - 48i. This results in a limited influence on the velocity profile of the air-flow, shown by Figures 48p - 48r. Therefore, it can be assumed that the air-flow is thoroughly mixed, which means that the bulk temperature can be expressed. The velocity profile of the 2D model has not been presented for the cases presented in Section 4.4. Due to time restrictions, this was not possible to do any more. Therefore, the assumption cannot be made for those cases.

5.3.1 Temperature difference

During frost conditions, the temperature difference is not the only heat source within the heat exchanger. The heat released by condensation or deposition is an extra heat source. This heat source also depends on the air temperature and influences the temperature of both fluid domains. Next, the frost layer blocks a part of the heat flux to the water domain due to its insulating effect and impedes the air-flow. The influence of the temperature difference is investigated by comparing cases 11 and 12. These cases have a temperature difference of 20 and 40 Kelvin, respectively. The inlet temperature of the water fluid stream is equal to 260 Kelvin for both cases, while the inlet temperature of the air-fluid stream is changed from 280 to 300 Kelvin. Figure 32 shows the governing bulk temperature profiles and relative humidity profiles at 10, 100 and 1800 seconds.

The bulk profiles in Figure 32 show large deviations between the two models. These differences are explained in Section 4 and will not be treated within this section. Only the influence of the temperature difference is examined. The bulk temperature profiles of the air-fluid stream (Figures 32a - 32c) show an increase in the temperature gradient of the 2D model. This gradient is almost not affected by frost growth. It becomes 0.2 Kelvin smaller over the entire time frame considered, which is also visualized by the plot with relative humidity, Figures 32g - 32i. Over time, the relative outlet humidity is slightly decreased due to a relatively low condensation/deposition mass flow rate compared to the total heat flux, shown in Table 16. This mass flux is lower for case 11, with a smaller temperature difference, since this flux is affected by the temperature decline. If this temperature decline is larger, it is more likely that the air-fluid stream drops below its dew point, resulting in a higher condensing mass flux. This results in a lower outlet relative humidity of both models for a larger temperature difference, shown in Figure 32g. The condensing mass flux of the 1D model is significantly higher due to a different modelling approach, which is explained in Section A. The air temperature profile of the 1D model, shown in Figure 33b,

remains constant over the heat exchanger at 100 and 1800 seconds since a fraction of the latent heat is transferred to the air-fluid stream. The outlet temperature of the air-fluid stream, shown in Figure 33d, is somewhat lower than the inlet temperature at 10 seconds, resulting in a slight increase for the relative humidity, shown in Figure 33g. At this stage of the simulation is the frost layer relatively thin. The frost growth over time deteriorates the heat transfer to the water fluid stream, resulting in a lower temperature at the outlet boundary. Furthermore, it is easier for the air-fluid stream to transfer heat to the water-fluid stream. Resulting in a higher net heat transfer rate and a slight decrease in the air temperature.

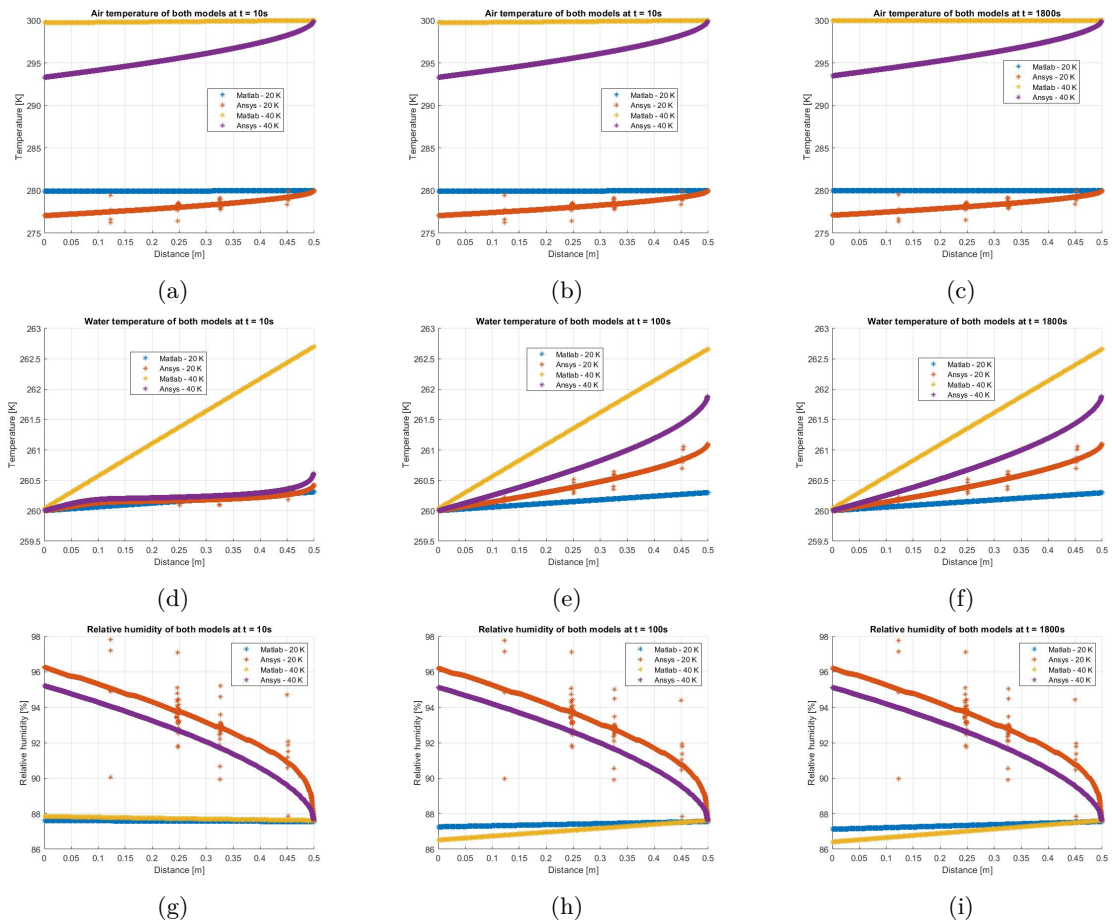


Figure 32: The bulk profiles of the ANSYS & MATLAB model for Cases 11 & 12. Results of the temperature in air domain (a-c) and water domain (d-f), and relative humidity (g-i) at time 10, 100 and 1800 seconds respectively.

Temperature difference (Time)	20 (10)	20 (100)	20 (1800)	40 (10)	40 (100)	40 (1800)
Effectiveness	0.18	0.18	0.18	0.18	0.18	0.18
Heat exchange rate - NTU	266.22	266.22	266.22	532.03	532.04	532.04
Heat exchange rate - LMTD	300.67	301.25	301.46	584.33	586.62	586.80
LMTD	19.80	19.84	19.85	38.47	38.62	38.64
Heat exchange rate - 1D (water)	64.11	62.03	61.26	556.11	548.05	547.41
Heat exchange rate - 1D (air)	6.88	2.00	0.23	21.40	1.72	0.12
Heat exchange rate - 1D (latent heat)	90.59	90.83	90.92	816.29	817.83	817.97
Heat exchange rate - 1D (net)	94.72	91.63	90.50	822.70	810.77	809.83
Heat exchange rate - 2D (water)	89.91	230.05	230.05	128.59	392.84	392.72
Heat exchange rate - 2D (air)	216.14	212.52	212.52	485.91	473.43	473.36
Heat exchange rate - 2D (latent heat)	3.66	3.55	3.55	23.96	23.28	23.27
Heat exchange rate - 2D (net)	223.53	219.73	219.72	413.54	404.90	404.89
Heat transfer coefficient - air	35.68	35.68	35.68	35.68	35.68	35.68
Heat transfer coefficient - water	204.30	204.30	204.30	204.30	204.30	204.30

Table 16: The performance indicators of the heat exchanger for a temperature difference at the inlet boundary of 20 and 40 Kelvin at 10, 100 and 1800 seconds. The temperature difference is given in Kelvin, heat exchange rates are given in Watts, and the heat transfer coefficient is given in $[W.m^{-2}.K^{-1}]$.

Comparing the bulk water temperatures of both cases, Figures 32d - 32f, shows an increase in outflow temperature for Case 12. The difference is increased by a factor of 9. This results from an increased mass that changes phase by a factor of 9 and a heat flux of the air-fluid stream that stays almost constant compared to the increase in the water and net heat fluxes. This also results in an increase in efficiency since the maximum amount of heat transfer is only doubled. The effectiveness, shown in Table 16, is not affected since the heat transfer coefficient and capacity remains constant. The increase in heat transfer of the 2D model is significantly lower than 2, which should lead to a decrease in effectiveness. The effectiveness shown in Table 16 has been calculated with Eq. 21 and is based on the log-mean temperature difference and heat transfer coefficients. The log-mean temperature is almost doubled since the outlet air temperature is not affected and the outlet water temperature is slightly increased. This results in a similar increase in the LMTD heat exchange rate. The NTU heat exchange rate is doubled due to an increase of the inlet temperatures by a factor of two, in line with Eq. 19.

The latent heat exchange rate is higher for Case 12, shown in Table 16. As explained before, the mass flux is lower for Case 11, since the mass flux is affected by the temperature decline. The air temperature decline of Case 12 is higher, shown in Figures 49d - 49f compared to Figures 48d - 48f, which causes a further increase in relative humidity. The weighted average relative humidity, shown in Figures 32g - 32i, does not reach the saturation level of 100%. The local relative humidity close to the heat exchange surface increases above this saturation level. This leads to frost formation close to the surface, at places where the temperature is below the freezing point, and a liquid film formation further from this surface where the temperature is above the freezing point and the relative humidity is above its saturation level.

A higher condensation and deposition rate and increased heat transfer rate of the air-fluid stream lead to a higher net heat transfer rate. This heat transfer rate decreases over time since the frost layer thickness for the 1D model and porosity of this frost layer for the 2D model increases. The release of latent heat remains constant or decreases while a higher amount of the latent heat is transferred to the air-fluid stream due to the insulating effect of the frost layer, shown in Table 16. This decreases both the net heat flux and the heat flux of the air-fluid stream. The heat transferred to the air-fluid stream decreases the temperature, resulting in lower heat flux.

The sum of the 1D heat transfer rates from the air-fluid stream and latent heat is not equal to the heat transfer rate of the water-fluid stream. These heat transfer rates do not have to be equal since a fraction of the latent heat is transferred to the air-fluid stream, and a part is transferred to the water-fluid stream. This leads to an increase in the water heat transfer rate and a decrease in the air heat transfer rate, which is explained in Section 4.4. Case 11 has similar dimensions and almost similar inlet conditions compared to Case 6 of Section 4, but the heat fluxes are different. The latent heat flux is 26% lower, whereas a higher latent heat flux should be expected due to the higher inlet relative humidity of Case 11. Furthermore, heat fluxes of the water and air domain differ substantially from the results presented

in Section 4.4. This should not be possible and could result from an in-robust model. Increasing the relative humidity should lead to a higher condensation/deposition mass flux. The higher this mass flux, the more difficult it will be to solve the simulation properly. Several attempts have been done to make the model more robust, for instance, further increasing the number of mesh cells and decreasing the time step size and relaxation factor. But none of these attempts led to a single and robust solution. It cannot be said what causes this inrobustness.

5.3.2 Humidity

The relative humidity at the inlet boundary of the air-fluid stream is another parameter that influences the performance of the heat exchanger. This parameter determines, together with the temperature difference, the amount of water vapour that contributes to the formation of the frost layer or liquid film. Air with a higher relative humidity will already condense by a smaller temperature decline. The influence of the humidity at the inlet boundary of the air-fluid stream is investigated in cases 10 and 11. The cases have an initial relative humidity of 61.7% and 87.6%, respectively. Figure 32 shows the governing bulk temperature profiles and relative humidity profiles at 10, 100 and 1800 seconds.

The profiles, shown in Figure 33, also show a large deviation between both models. The 1D model has almost a constant relative humidity, shown by Figures 33g - 33i, for both cases while the relative humidity of the 2D model increases over the length of the heat exchanger. The difference between both models is similar to the difference shown in Section 5.3.1, which explains the reason. The increase in relative humidity of the 2D model is higher for Case 10, with an inlet relative humidity of 61.7%. This is caused by a lower amount of water vapour that is condensed, shown by the latent heat exchange rate in Table 17, and a similar bulk temperature profile of the air-fluid stream, shown in Figures 33a - 33a. Both cases' air bulk temperature profile does not differ much because heat release by the frost formation and condensation is relatively low compared to the total heat transfer. Nevertheless, the difference of the water bulk temperature is better visualized by Figure 33, by Figures 33d - 33f. The increase in relative humidity leads to a higher outlet temperature of the water-fluid stream of both models. The outlet temperature of the 2D model is higher due to the low heat transfer rate of the air-fluid stream within the 1D model. Within the 1D model, a larger fraction is possibly transferred to the air-fluid stream, resulting in a lower heat transfer rate of the air and water-fluid stream. The bulk temperature profiles of the water-fluid stream of the 2D model, shown in Figure 33d, have deviating trend. Based on the results presented, no declaration can be given since the latent heat flux is relatively low and the air temperature, in Figure 32a, has a different trend. It could result from an unstable and in-robust solution, which will be explained in Section 6. Similar differences are shown for Case 12.

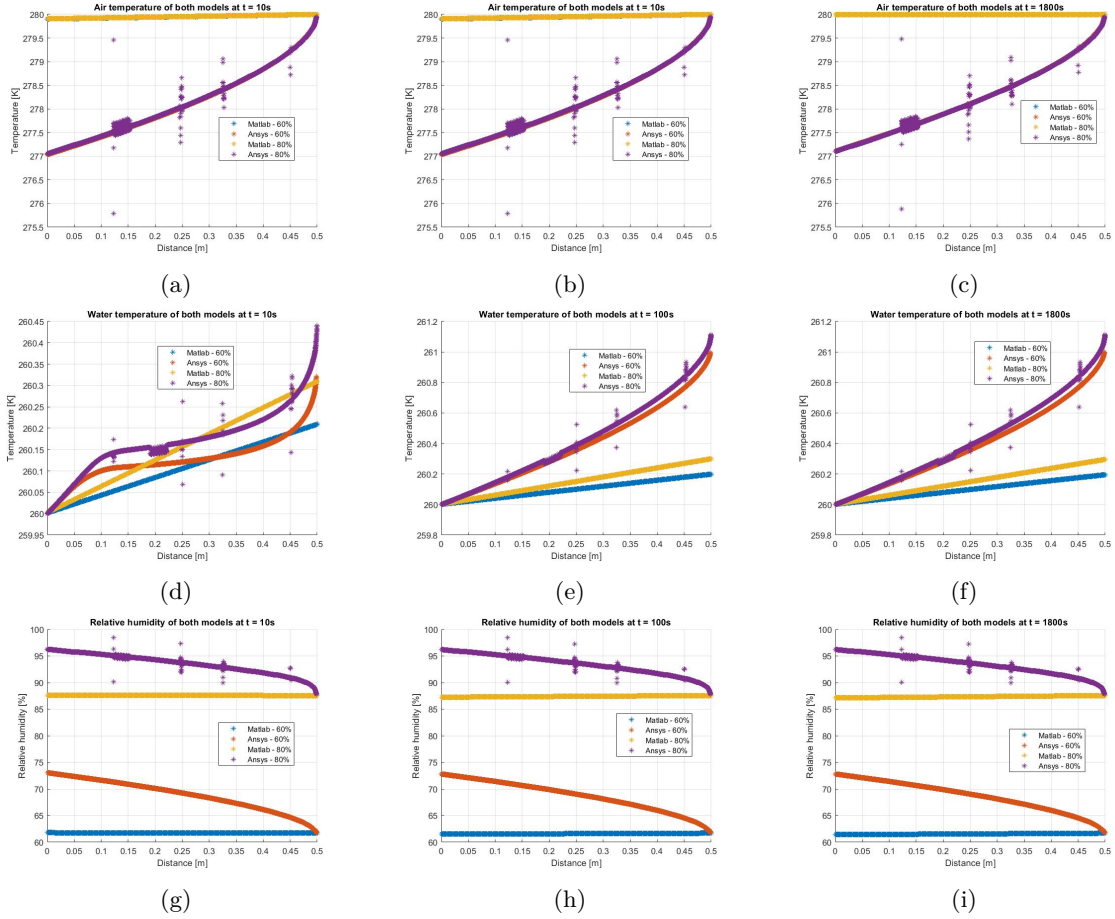


Figure 33: The bulk profiles of the ANSYS & MATLAB model for Cases 10 & 11. Results of the temperature in air domain (a-c) and water domain (d-f), and relative humidity (g-i) at time 10, 100 and 1800 seconds respectively.

Relative humidity (Time)	61.7 (10)	61.7 (100)	61.7 (1800)	85.7 (10)	85.7 (100)	85.7 (1800)
Effectiveness	0.18	0.18	0.18	0.18	0.18	0.18
Heat exchange rate - NTU	273.18	273.18	273.18	266.22	266.22	266.22
Heat exchange rate - LMTD	310.44	311.05	311.26	300.67	301.25	301.46
LMTD	19.90	19.88	19.90	19.80	19.84	19.85
Heat exchange rate - 1D (water)	59.44	59.44	59.44	64.11	62.03	61.26
Heat exchange rate - 1D (air)	0.31	0.31	0.31	6.88	2.00	0.23
Heat exchange rate - 1D (latent heat)	59.91	59.91	59.91	90.59	90.83	90.92
Heat exchange rate - 1D (net)	59.74	59.74	59.74	94.72	91.63	90.50
Heat exchange rate - 2D (water)	68.36	209.41	209.94	89.91	230.05	230.05
Heat exchange rate - 2D (air)	215.37	210.49	210.45	216.14	212.52	212.52
Heat exchange rate - 2D (latent heat)	1.76	1.66	1.66	3.66	3.55	3.55
Heat exchange rate - 2D (net)	220.26	215.50	215.50	223.53	219.73	219.72
Heat transfer coefficient - air	36.94	36.94	36.94	35.68	35.68	35.68
Heat transfer coefficient water	204.30	204.30	204.30	204.30	204.30	204.30

Table 17: The performance indicators of the heat exchanger for a relative humidity at the inlet boundary of 61.7 and 82.1% at 10, 100 and 1800 seconds. The relative humidity is given in percentages, heat exchange rates are given in Watts, and the heat transfer coefficient is given in $[W.m^{-2}.K^{-1}]$.

The effectiveness of both cases, shown in Figure 17, are similar since the heat transfer coefficients are almost similar. These coefficients are somewhat higher for Case 10 due to the difference in relative humidity. This results in slightly lower NTU heat exchange rates. The log-mean temperature difference of Case 11 is somewhat lower since the outlet temperature of the water-fluid stream is higher, resulting in a lower LMTD heat exchange rate. This higher temperature gradient of the water-fluid stream leads to a higher governing heat exchange rate for both models.

As described, the condensing/deposition mass flux is higher for Case 11. This results, together with the increased air heat flux, in a higher net heat flux. Similar to the results shown in Section 5.3.1. The water heat flux of the 1D model decreases over time since frost layer thickness increases. Nevertheless, the water heat flux of the 2D model is increased over time. This could result from the deviating trend, shown in Figure 33d. This can mean that the water heat transfer at 10 seconds is incorrect, which will be further explained in Section 6.

6 Discussion

The results presented in Chapter 4 and 5 are discussed in this chapter. Looking at the results given by the figures in these chapters and their corresponding appendices, interesting observations can be made. These observations are grouped into several topics: experimental validation, heat transfer, condensation, frost formation and stability.

Experimental validation

The results presented are not validated with experimental results. The models are only compared to each other and the NTU and LMTD methods. In the literature, no experimental data is available to compare these results with. Most tested heat exchangers have a way more complex or different geometry. This heat exchanger consists mostly of a cross-flow flow configuration. Nevertheless, in the literature, some papers describe experiments on counter-flow heat exchangers [37]. But the configuration of inlet and outlet boundaries used within these experiments differs from the geometry used within the models presented in this research. Deviating results can be expected, which makes a comparison not valuable.

Since the models are not validated properly, which model performs better is unknown. All statements based on the given results are possible reasons for the differences. It cannot be said whether this is why a difference occurs. The statements are based on circumstances within a heat exchanger described in the literature. The models are also based on relations described within the literature. But implementation errors could have been made since the results were not compared with others. This is more likely to occur in cases with condensation and frost formation. Cases with only heat transfer can more easily be checked with the NTU and LMTD methods. These methods do not take into account condensation and frost formation. Therefore, these methods do not have similar results for these circumstances as the models presented.

Both models' mesh and time convergence study is also not compared to experimental data. Only the relative error to the most refined mesh or time step can be computed to investigate whether the model shows convergence. It is unknown in what way these results differ from reality. Therefore, it is impossible to determine the overall accuracy and check whether the mesh or time step computes valid results. The decreasing relative error by a grid or time step refinement shows that the solution is approaching the most accurate solution available.

Heat transfer

Both models implement the exchange of heat in different ways. The equations of the 1D model consider a fully-developed flow. In contrast, the 2D model has a uniform inlet velocity profile which develops due to viscous forces and no-slip conditions on the wall to a fully-developed flow. During this transition, also referred to as the thermal entrance length, is the heat exchange rate higher. Since both fluids are flowing in opposite directions, the heat exchange rate at the outlet boundary is also increased by the thermal entrance length of the counter-flowing fluid. This results in a higher overall heat exchange rate for the 2D model.

The heat exchange rates of the NTU & LMTD methods also consider a fully-developed flow. Therefore, the heat exchange rates of these methods are roughly similar to the heat exchange rate of the 1D model during dry conditions. Small deviations can be attributed to the relative error created by the mesh. The NTU method is not influenced by the outlet temperatures of the 1D model, only by the mean heat transfer coefficient of the 2D model. The LMTD method is influenced by both factors, resulting in larger possible deviations.

The different implementation of the heat transfer coefficient also influences the heat exchange rates. This coefficient is kept constant within the 1D model, while it is a function of the velocity and density within the 2D model. It results in an increasing coefficient over the length of the heat exchanger and a higher value at the centre of the fluid stream if the fluid flow is fully developed. The heat transfer coefficient of the 1D model equals the mean value of the coefficient 2D model. This results in an over-estimated coefficient, thus the heat transfer rate, in the first part (from the leading edge) of the heat exchanger and an underestimated coefficient in the last part. The coefficients of both models are not equal halfway to the total length since the coefficient of the 2D model scales not linearly with the length.

For each case, presented in Chapters 4 and 5, is the overall heat exchange rate and the heat exchange rate for both individual fluid streams given. These heat exchange rates are equal for dry conditions within the 1D model. Within the 2D model, these rates can differ due to a difference in the thermal boundary layer of each fluid stream, explained in Section 4.2. But it is not possible that more heat is transferred to the water (or cold) fluid stream than is released by the air (or hot) fluid stream. In Case 1, shown in Section 4.2, is the heat transfer rate of the cold fluid higher than the net heat transfer rate and heat transfer from the hot fluid. This is thermodynamic incorrect because it is not possible to provide more heat to the cold fluid stream than generated by the hot fluid stream. This simulation has been recalculated several times but did not lead to a different solution. It is unknown why this problem occurs in this case. In all other cases presented in Section 4.2, this problem does not occur.

Condensation

How condensation is implemented is different for both models. Water vapour can become saturated if the temperature decreases beneath its dew point or when it has contact with a surface at a temperature beneath its dew point. Therefore, it is required that the nodes are adjacently located to the heat exchange surface. Within the 1D model, all sections are adjacent to the heat exchange surface, while in the 2D model, only a fraction of the nodes have direct contact with this surface. Only for these nodes can this effect be incorporated. All other nodes can become saturated if the air temperature decreases beneath its dew point. This difference in implementation results in a different mass flux of condensation, which makes them unable to compare with each other. The condensing mass flux of the 1D model is generally higher.

The amount of condensed water vapour due to contact with a surface at a temperature beneath its dew point has been calculated based on the surface temperature. This value is expressed within the 1D model, based on Eq. 41. This value can only be computed within the ANSYS model if the wall has a certain thickness. But in most cases, the wall is a non-conformal wall that has no thickness. This means that the interface wall has no nodes. The adjacent mesh cell with a temperature lies within the water domain, which generally has a lower temperature than the surface temperature.

The temperature profiles for both models are expressed by the bulk temperature, explained within Section D.1. This temperature is the weighted average temperature which should be based on the local mass flux. The density can be considered a constant for a thoroughly mixed fluid. The bulk temperature can be computed based on the velocity, given in Eq. 99. Due to the condensation, mass flux is the density varying, which means that the temperature needs to be corrected by this parameter to compute a correct value for the bulk temperature. Nevertheless, the bulk temperature is only expressed on the velocity. This results in an incorrect value for the bulk temperature.

Frost formation

The equations used for the condensation mass flux are also applied to calculate the amount of mass that forms the frost layer. That means that similar differences can be observed, which are encountered by wet conditions. Furthermore, the build-up of the frost layer is different. The frost layer of the 1D model is dense and grows only in thickness. In contrast, the frost layer of the 2D model has a certain porosity and grows by combining two contributions, densification and increased frost thickness. This makes it impossible to compare the frost thickness of both models. Only the latent heat can be compared due to a certain amount of mass that undergoes a phase change.

The distribution of the heat fluxes over the separate domains also differs due to the different frost layer characteristics. Within the 1D model, the frost layer increases the resistance for heat transfer to the water-fluid stream, described within Section 3.1.3. As the frost layer thickness increases over time, the heat exchange rate to the water-fluid stream decreases, as shown in Table 16. To increase the outlet temperature, a fraction of the latent heat is transferred to the air-fluid stream. Within the 2D model, the resistance is not increased that much. The permeability of the frost layer is relatively high, shown in Figure 27b. Over time, the net heat transfer and heat transfer to the water-fluid stream is increased.

This difference also affects the mass flow rate governed by both models. An increase in frost layer thickness decreases the mass flow rate of the air-fluid stream within the 1D model. The inlet velocity is kept constant while the cross-section area decreases by frost growth, resulting in lower mass flow and heat exchange rates. This mass flow rate is kept constant within the 2D model.

The 1D model is modelled based on a quasi-steady state assumption. Within each time step, the airflow is stable, and the properties of air and frost are constant. At the same time, the time derivatives of these parameters are incorporated within the 2D model. Generally, this simulation can handle conditions that change with time and assess the time-dependent impact on thermal and flow conditions. It can not be said whether this different modelling approach impacts the results of both models. This difference is minimized with the time-step convergence study to create constant results.

The implementation differences of both models make it more difficult to compare both models to each other.

Stability

The simulations executed by both models need to show convergence to create a robust and stable solution. This solution is stable if it is the only solution created every time the simulation is executed. To create this solution, convergence criteria have been described. These criteria are described within Section 3.2.4 for the 2D model. These criteria are not always met as the relative humidity at the inlet boundary or the temperature difference between both fluid streams increases. Especially when a frost layer is formed, the complexity of the simulation is increased. The bulk temperature profiles, shown in Figure 33, show some deviating data points. This could be the consequence of a non-converging solution.

The 1D model is in-robustness for the frost cases presented in Section 5.3.1. Case 11 of Section 5 has similar dimensions and almost similar inlet conditions compared to Case 6 of Section 4, but the heat fluxes are significantly different. This should not be possible and could be the result of an in-robust model. Increasing the relative humidity should lead to a higher condensation/deposition mass flux. The higher this mass flux, the more difficult it will be to solve the simulation properly. Several attempts have been done to make the model more robust, for instance, further increasing the number of mesh cells and decreasing the time step size and relaxation factor. But none of these attempts led to a single and robust solution for that particular Case, Case 11 of Section 5. It cannot be said what causes this inrobustness. Similar differences are shown for Case 12.

7 Conclusions and Recommendations

7.1 Conclusions

This report presents two heat exchanger models with a special focus on frost formation. The models are based on a segmented approach and can be applied to a counter-flow heat exchanger geometry. The 1D quasi-steady state model predicts the dynamic formation of a dense frost layer and condensation by heat and mass balances. The 2D time-dependent model is based on conservation laws for each phase and the entire mixture and an enthalpy-porosity formulation for forming a frost layer. The following conclusions can be drawn from the comparison of both models:

- predicted temperatures along both fluid streams of both models are in fair agreement for dry conditions. The uniform velocity profile of the 2D model results in deviations close to the inlet and outlet boundaries.
- frost formation & condensation and thus latent heat is generally underestimated by the 2D model.
- heat transfer by the 2D model is generally overestimated for dry conditions.
- insulating effect of the frost layer is higher for the 1D model.

This is only a comparison between both models. The results are not validated with experimental results. Given statements are possible reasons for the shown differences. Nevertheless, several parameters' influence on the heat exchanger's performance has been investigated. It is demonstrated from the results of both models that:

- increasing the temperature difference between both fluid streams does not affect the efficiency.
- decreasing the cross-sectional area results in a higher effectiveness and heat transfer.
- the total amount of water vapour that condenses increases for a higher temperature difference and inlet humidity.
- the heat transfer rate is decreased over time due to frost formation.

From the results, it became clear that there are still inconsistencies in the numerical outcomes. Additional research and comparison with experimental results are required to have a model that can be used to optimise the heat exchanger design.

7.2 Recommendations

As mentioned in Section 7.1, additional research is required to develop a model that provides valid results. This additional research should mainly focus on the comparison with experimental results and the improvement of stability.

The 1D model is a very basic model that can be used to roughly predict frost thickness. This prediction can be made more accurate if the frost layer is modelled with a porosity level, the heat transfer coefficient is non-constant, the temperature and relative humidity become time-dependent and a temperature distribution in vertical direction can be made.

To make the comparison with the 2D model more accurate, the condensation and frost formation method should be implemented similarly, and the inlet velocity profile should be uniform instead of fully developed.

The stability of both models can be increased by further minimising the time step size and higher amount of mesh cells. This increases the required computational time substantially. This was not possible within this research.

Experiments should be executed on a similar geometry under controlled conditions and accurate measuring equipment. Especially the relative humidity and temperature at the inlet and outlet boundary should be measured very accurately. These parameters have a large influence on performance.

At last, the model can be extended to other and more complex geometries and such that defrosting can be included. This would allow for optimising the optimal design for operating the air cooler in winter conditions, where the air cooler needs to be defrosted as well.

References

- [1] ANSYS Fluent User's Guide, 2021R1, 2021.
- [2] Hewitt G.F. aborek, J. and N. Afgan. *Heat Exchangers: Theory and Practice*. Hemisphere Publishing Corporation., 1983.
- [3] Nawaf F. Aljuwayhel. Numerical and Experimental Study of the Influence of Frost Formation and Defrosting on the Performance of Industrial Evaporator Coils. 2006.
- [4] Jr Anderson, John D. *Fundamentals of aerodynamics 6th edition*. McGraw-Hill Education, 2017.
- [5] Yusuf Baçoğul, Onur Vahip Güler, and Ali Keçebaş. Binary geothermal power plant. *Thermodynamic Analysis and Optimization of Geothermal Power Plants*, pages 113–129, 2021.
- [6] W.E. Bird, R.B.; Stewart. *Transport phenomena, Second Edition*. John Wiley Sons, Inc., 2002.
- [7] A.C.; Nagle W.M. Bowman, R.A.; Mueller. Mean temperature difference in design. *Trans. Am. Soc. mech. Engrs.*, (62):283–294, 1940.
- [8] Voller V R & Prakash C. A Fixed grid numerical modelling methodology for convection diffusion mushy region phase change problems. *International Journal of Heat Mass Transfer*, 30(8):1709–1719, 1978.
- [9] Y. Cengel. *Heat and mass transfer: fundamentals and applications*. McGraw-Hill Higher Education, 2014.
- [10] H.H.S. Churchill, S.W.; Chu. Correlating Equations for Laminar and Turbulent Free Convection from a Horizontal Cylinder. *International Journal of Heat and Mass Transfer*, (18):1049–1053, 1975.
- [11] Mehrnoush Davanipour, Hamidreza Javanmardi, and Nasrin Goodarzi. Chaotic Self-Tuning PID Controller Based on Fuzzy Wavelet Neural Network Model. *Iranian Journal of Science and Technology - Transactions of Electrical Engineering*, 42(3):357–366, 2018.
- [12] DeCaria. Cloud Physics and Precipitation Processes Lesson 8 - Growth of Ice Crystals. pages 1–7.
- [13] Jiankai Dong, Shiming Deng, Yiqiang Jiang, Liang Xia, and Yang Yao. An experimental study on defrosting heat supplies and energy consumptions during a reverse cycle defrost operation for an air source heat pump. *Applied Thermal Engineering*, 37:380–387, 2012.
- [14] A. J. Fabiano and J. Qiu. FVM vs FDM. *Journal of Neurosurgical Sciences*, 59(2):157–167, 2015.
- [15] N. H. Fletcher. *The Chemical Physics of Ice*. Cambridge Monographs on Physics. Cambridge University Press, 1970.
- [16] Y. Hayashi, A. Aoki, S. Adachi, and K. Hori. Study of frost properties correlating with frost formation types. *Journal of Heat Transfer*, 99(2):239–245, 1977.
- [17] Christian J.L. Hermes, Robson O. Piucco, Jader R. Barbosa, and Cláudio Melo. A study of frost growth and densification on flat surfaces. *Experimental Thermal and Fluid Science*, 33(2):371–379, 2009.
- [18] Ellen Hertle, Simon Van Buren, Patric Figueiredo, Reinhold Kneer, and Wilko Rohlf. Modelling the defrost process in complex geometries - Part 2: Wall-function based coupling to a multi-region CFD solver. *E3S Web of Conferences*, 22(November), 2017.
- [19] Chengzhi Huang, Yugang Zhao, and Tian Gu. Ice dendrite growth atop a frozen drop under natural convection conditions. *Crystals*, 12(3), 2022.
- [20] D.P.; Bergman T.L.; Lavine A.S. Incorpora, F.P.; Dewitt. *Fundamentals of heat and mass transfer - 6th edition*, volume 112. John Wiley & Sons, Inc., 2007.
- [21] Noreen Jamil. A comparison of iterative methods for the solution of non-linear systems of equations. *Int. J. Emerg. Sci*, 3(2):119–130, 2013.

- [22] Byron W. Jones and Jerald D. Parker. Frost Formation With Varying Environmental Parameters. *American Society of Mechanical Engineers (Paper)*, (74 -HT-52):255–259, 1974.
- [23] C. Zemach J.U. Brackbill, D.B. Kothe. A continuum method for modeling surface tension. *Journal of Computational Physics*, 100:335–354, 1992.
- [24] U. Kaminski, S.; Groß. Luftseitiger wärmeübergang und druckverlust in lamellenrohr-wärmeübertragern. *Luft-und Kältetechnik*, 1(36):13–18, 2000.
- [25] W.M. Kays and A.L. London. *Compact Heat Exchangers*. McGraw-Hill series in mechanical engineering. McGraw-Hill, 1984.
- [26] M.S. Kreith, F.; Bohn. *Principles of Heat Transfer, Sixth Edition*. Brooks/Cole: Pacific Grove, 2001.
- [27] J.M.; Jallut C. Le Gall, R.; Grillot. Modelling of frost growth and densification. *International Journal of Heat and Mass Transfer*, 13(40):3177–3187, 1997.
- [28] J.M.; Jallut C. Le Gall, R.; Grillot. Modelling of frost growth and densification. *International Journal of Heat and Mass Transfer*, page 40(13):3177–3187, 1997.
- [29] L.S. Liu. On Fourier’s law of heat conduction. *Continuum Mechanics and Thermodynamics*, page 301–305, 1990.
- [30] C. H.M. Machielsen and H. G. Kerschbaumer. Influence of frost formation and defrosting on the performance of air coolers: standards and dimensionless coefficients for the system designer. *International Journal of Refrigeration*, 12(5):283–290, 1989.
- [31] G. Mader and C. Thybo. A new method of defrosting evaporator coils. *Applied Thermal Engineering*, 39:78–85, 2012.
- [32] M.H. Monteith, J.L.; Unsworth. *Principles of Environmental Physics*. Academic Press, 2007.
- [33] Swati Mukhopadhyay. Analysis of Boundary Layer Flow and Heat Transfer along a Stretching Cylinder in a Porous Medium. *ISRN Thermodynamics*, 2012:1–7, 2012.
- [34] F. Murray. On the Computation of Saturation Vapor Pressure. *Journal of Applied Meteorology*, pages 203–204, 1967.
- [35] Byeongchul Na and Ralph L. Webb. A fundamental understanding of factors affecting frost nucleation. *International Journal of Heat and Mass Transfer*, 46(20):3797–3808, 2003.
- [36] W. Nusselt. Eine neue Formel für den Wärmeübergang im Kreuzstrom. *Tech Mech U Therm*, (1):417–422, 1930.
- [37] Ali Pakari and Saud Ghani. Comparison of 1D and 3D heat and mass transfer models of a counter flow dew point evaporative cooling system: Numerical and experimental study. *International Journal of Refrigeration*, 99:114–125, 2019.
- [38] Ahmet Z. Sahin. Effective thermal conductivity of frost during the crystal growth period. *International Journal of Heat and Mass Transfer*, 43(4):539–553, 2000.
- [39] R. Sanders. Frost formation: the influence of frost formation and defrosting on the performance of air coolers. 1974.
- [40] H. Schlichting. *Boundary-Layer Theory, 7th ed.* McGraw Hill, 1979.
- [41] K. Schlichting, H.; Gersten. *oundary-Layer Theory. 8th Edition*. Springer-Verlag, Berlin, 2000.
- [42] Liang Liang Shao, Liang Yang, and Chun Lu Zhang. Comparison of heat pump performance using fin-and-tube and microchannel heat exchangers under frost conditions. *Applied Energy*, 87(4):1187–1197, 2010.
- [43] C. Shavit, A.; Gutfinger. *Thermodynamics: From concepts to applications (2nd edition)*. Taylor & Francis group, 2008.

- [44] A. Sokolichin, G. Eigenberger, A. Lapin, and A. Lübbert. Dynamic numerical simulation of gas-liquid two-phase flows: Euler/Euler versus Euler/Lagrange. *Chemical Engineering Science*, 52(4):611–626, 1997.
- [45] G. E.; Hood J. M. Sterner, R. W.; Small. "The Conservation of Mass". *Nature*. 2022.
- [46] Dong Liang Sun, Jin Liang Xu, and Li Wang. Development of a vapor-liquid phase change model for volume-of-fluid method in FLUENT. *International Communications in Heat and Mass Transfer*, 39(8):1101–1106, 2012.
- [47] Linquip Team. What is cross flow heat exchangers and its working principles. <https://www.linquip.com/blog/cross-flow-heat-exchangers/>, 2021.
- [48] Agilent technologies. Hints for selecting the correct temperature sensor for your application. *Measurement tips*, 1(3):3–6, 2008.
- [49] C. P. Tso, Y. C. Cheng, and A. C.K. Lai. An improved model for predicting performance of finned tube heat exchanger under frosting condition, with frost thickness variation along fin. *Applied Thermal Engineering*, 26(1):111–120, 2006.
- [50] W. Versteeg, H. K.; Malalasekera. *Introduction to Computational Fluid Dynamics*. Pearson Education Limited, 2007.
- [51] Th. von Kármán. Mechanical Similitude and Turbulence. *Nachrichten von der Gesellschaft der Wissenschaften zu Göttingen, Fachgruppe 1 (Mathematik)*, page 5: 58–76, 1930.
- [52] Water Science School. Sublimation and the Water Cycle, 2019.
- [53] B Wellig, M Imholz, M Albert, and K Hilfiker. Defrosting the Fin Tube Evaporators of Air / Water Heat Pumps Using Ambient Air. *9th International IEA Heat Pump Conference*, (May):20–22, 2008.
- [54] Wilson Rorrer Welty, Wicks. *Fundamentals of Momentum, Heat and Mass transfer 5th edition*. John Wiley Sons, Inc., 2008.
- [55] M. Xiong and A. V. Kuznetsov. Comparison between lever and Scheil rules for modeling of micro- porosity formation during solidification. *Flow, Turbulence and Combustion*, 67(4):305–323, 2001.
- [56] Bing Yu, Xichun Wang, and Peter Luscuere. Performance prediction on the finned-tube dry cooler in winter period. *IBPSA 2009 - International Building Performance Simulation Association 2009*, pages 385–391, 2009.
- [57] Y.; Ki Min M. Yun, R.; Kim. Modeling of frost growth and frost properties with airflow over a flat plate. *International Journal of Refrigeration*, page 25(3):362–371, 2002.
- [58] H. Zaïdi, S. Fohanno, R. Taïar, and G. Polidori. Turbulence model choice for the calculation of drag forces when using the CFD method. *Journal of Biomechanics*, 43(3):405–411, 2010.
- [59] Li-Zhi Zhang. Chapter 11 - effectiveness-ntu methods for heat and mass transfer processes. In Li-Zhi Zhang, editor, *Conjugate Heat and Mass Transfer in Heat Mass Exchanger Ducts*, pages 309–334. Academic Press, Boston, 2013.

A Condensation & Deposition

Condensation is the change in the state of water vapour to liquid water when in contact with a liquid or solid surface and is the reverse of vapourization. These processes occur simultaneously, but the ratio depends on several conditions expressed by the relative humidity. It indicates the percentage of water in the air as a percentage of the total water that can be contained until the saturation point is reached at a certain temperature, the dew point temperature [43].

The relative humidity is below 100% if the air temperature is above the dew point temperature. This means the vapourization mass flow rate is higher than the condensation mass flow rate. These mass flow rates are equal if the air temperature is at its dew point temperature, with a relative humidity of 100%. Relative humidity above 100% means that the air temperature is below its dew point temperature and that there is a net condensation mass flow rate.

Thus, the relative humidity depends on the air temperature. It can be expressed as the ratio between the partial pressure of the water vapour to the equilibrium vapour pressure of water, also known as the saturation vapour pressure [43]. The equilibrium vapour pressure of water is the pressure at which water vapour is in thermodynamic equilibrium with its condensed state. Excess water vapour would condense at pressures higher than the vapour pressure, whilst at lower pressures water would evaporate. The equilibrium vapour pressure of water increases with increasing temperature. As the temperature of water molecules increases, the kinetic energy of its molecules also increases. As the kinetic energy of the molecules increases, the number of molecules transitioning into a vapour also increases, thereby increasing the vapour pressure.

The air humidity can increase above its saturation level due to a decrease in air temperature beneath its dew point or contact with a surface at a temperature beneath the dew point [43].

A.1 Contact with a surface

The mass flow rate of condensation due to contact with a surface at a temperature beneath the dew point can be expressed with the humidity ratios or specific humidity, denoted by ω . This humidity ratio describes the ratio between the mass of the moisture to that of the dry air:

$$\omega = \frac{m_w}{m_a} = 0.622 \frac{\phi p_{sat}}{p - \phi p_{sat}} \quad (70)$$

where ϕ is the relative humidity as a fraction of the saturation humidity level and p is the ambient air pressure in Pascal. There are many expressions to approximate the saturation vapour pressure of water. One of them is the Tetens equation. This equation expresses the saturation vapour pressure as a function of the air temperature. The Tetens' formula for temperatures above 0 °C can be expressed as [32].

$$P_{sat} = 610.78 \exp\left(\frac{17.27T_a}{T_a + 237.3}\right) \quad (71)$$

with P_{sat} as the saturation pressure in Pascal and T_a representing the air temperature in Degrees Celsius. For temperatures below 0 °C can the Tetens' formula be expressed as [34]:

$$P_{sat} = 610.78 \exp\left(\frac{21.875T_a}{T_a + 265.5}\right) \quad (72)$$

In general, ω is not linear with ϕ . However, for temperature <35 °C, the saturation pressures are very low, compared with the atmospheric pressure and may be neglected in the denominator. Under these conditions, the specific humidity is almost proportional to the relative humidity. Thus, for $p_{sat} \ll p$:

$$\omega = \frac{m_w}{m_a} = 0.622 \frac{p_{sat}}{p} \phi \quad (73)$$

The condensation mass flux can be calculated by subtracting the humidity ratio at the surface from the humidity ratio of the flowing air [43]. This difference in humidity ratio can be multiplied with a mass transfer coefficient U_m . The resulting equation for the condensation mass flux is as follows:

$$m_v'' = U_m(\omega_a - \omega_s) \quad (74)$$

where m_v'' is the condensation mass flux per unit area, ω_a is the humidity ratio of the flowing air and ω_s is the humidity ratio of the surface in the 1D MATLAB model. The humidity ratio ω_{fst} is calculated with the adjacent mesh cell to the heat exchanger surface in the water domain of the ANSYS model. In most cases, the wall has no thickness and has, thus, no contributing resistance to the heat transfer coefficient. For these circumstances, the wall is non-conformal. This means that the interface wall has no nodes on both cells. The adjacent mesh cell to calculate the humidity ratio ω_{fst} with lies in the water domain. It is assumed that the relative humidity of this mesh cell is equal to 100%. The mass transfer coefficient of Eq. 74 can be calculated by:

$$U_m = \frac{\alpha_a}{C_{p,a}Le} \quad (75)$$

All nodes have contact with the heat exchange surface within the 1D MATLAB model. Therefore, this phenomenon is applicable to all nodes. Within the 2D & 3D ANSYS are only some nodes adjacent to the heat exchange surface. Only for these nodes can this effect be incorporated. All other nodes have only the condensing effect due to the decrease in air temperature beneath their dew point.

A.2 Decrease air temperature

Calculating the mass flow rate for condensation when it is in contact with a surface at a temperature beneath its dew point can result in a relative air humidity above 100%. This can occur if the temperature difference between the air and surface is relatively big and the air humidity is close to 100%.

If the temperature difference is relatively big, this results in a relatively big air temperature decrease and thus a great decrease in maximum water vapour the air can contain. A relatively large amount of water vapour must condense to keep the relative air humidity constant. Depending on the conditions, the relative air humidity will not decrease or remain constant at a certain temperature difference. Still, it will increase by increasing the temperature difference between the air and surface [43].

An increase in relative humidity above 100% results in over-saturated air and provides a net condensation mass flow rate [53]. This mass flow rate can be calculated based on relative humidity and air temperature. The humidity is expressed in percentages. This is the dimension for the relative humidity which the model uses. But the mass flow due to condensation has to be expressed in a mass flux per unit area [kg/m^2s]. To calculate this, the relative humidity has to be expressed as absolute humidity by using the following equation [43]:

$$AH = \frac{0.0132e^{\frac{17.67(T_a - 273.15)}{(T_a - 38.65)}}}{T_a} \phi \quad (76)$$

The absolute humidity has been calculated with Eq. 76 on each boundary in the 1D MATLAB models. The difference between the two boundaries' absolute humidity is water vapour's mass flux. This can be expressed in the following equation, in which the mass flux is multiplied by the cell area A :

$$AH_i = AH_{i+1} - m_{v,i}''A \quad (77)$$

The MATLAB model computes a mass flux at each boundary. So for instance, cell i has boundaries i and $i + 1$, shown in Figure 7. The mass flux for boundary i will be used to calculate the temperatures and air humidity at boundary i . To calculate which amount of mass vapour that has to condense to stay at a relative humidity of 100% at boundary i , the difference in absolute humidity between boundary i and $i + 1$ has to be incorporated since the air-flow directions is from boundary $i + 1$ to i .

The mass flux per unit area in terms of relative humidity and air temperature can be calculated by substituting the equation for the absolute humidity into the equation for the mass flux:

$$m_{v,i}'' = \frac{\frac{0.0132e^{\frac{17.67(T_{a,i+1} - 273.15)}{(T_{a,i+1} - 38.65)}}}{T_{a,i+1}} \phi_{i+1} - \frac{0.0132e^{\frac{17.67(T_{a,i} - 273.15)}{(T_{a,i} - 38.65)}}}{T_{a,i}} \phi_i}{A} \quad (78)$$

The value relative humidity at boundary i will be set at 100% if the value is higher than 100%. This way, the relative humidity will not get over-saturated and exceed the value of 100%.

The ANSYS model computes the mass flux at each mesh point. The condensation mass flux can be expressed based on the absolute humidity, which is computed with the volume fraction of water vapour and air temperature. The expression for the absolute humidity is as follows:

$$AH = \phi_v \rho_v \quad (79)$$

The resulting mass flux, which sets a limit on the relative humidity at 100%, can be computed with the following equation:

$$m''_{v,i} = \frac{AH - 1.32e^{\frac{17.67(T_{a,i} - 273.15)}{(T_{a,i} - 38.65)}}}{A} \quad (80)$$

If the relative humidity is over-saturated, the expression for mass flux Eq. 79 corrects it to a value of 100%. The mass flux of Eq. 79 is set to zero for a mesh cell with relative humidity below 100%.

The MATLAB and ANSYS model compare the resulting mass flux computed by both methods: the mass flux due to contact with a surface at a temperature beneath the dew point and the mass flux due to increased air humidity above its saturation level. The highest mass flux is used as the resulting mass flux.

A.3 Deposition

Next to the phase change from gas (water vapour) to liquid (water), another phase change occurs in the heat exchanger with temperatures below the freezing point of water. The condensed water vapour will form a frost layer on the heat exchange surface area when it is below 0 °C. This transition can occur in two steps. First, the water vapour will condensate to water. Secondly, the formed water will freeze to the surface. But this step can also be taken once, from water vapour to frost. This is called deposition [57].

In practice, this process will also occur in two steps. The condensed water vapour enters the frost layer. Part of the water vapour transferred to the frosted surface will be diffused into the existing frost layer before it freezes [28]. The diffused water vapour will contribute to an increase in frost density. The ice sheet will grow if the mass flow of water from the air exceeds the flow downwards. The ice will grow very fast in the beginning. The density of the ice close to the fin will be higher at the surface. This will overestimate the growth, but the frost surface saturation assumption is valid.

The phase change from water to frost is also an endothermic process, which releases energy. For this phase change, 334 J/g will be released [52]. This is significantly lower than the latent heat of the phase change from water vapour to water, which is 2500 J/g. A combination of both processes creates a larger amount of latent heat. This is incorporated into the latent heat variable in the model, shown in Eq. 24.

The method, in which the mass flow rate of condensation due to contact with a surface at a temperature beneath the dew point has been calculated, can be used for temperatures below and above 0 °C. But there are differences between the resulting mass flux. The mass flux will be higher if the surface temperature is beneath 0 °C, so when a frost layer is formed. The saturation vapour pressure determines the growth rate. The saturation vapour pressure is lower in frost conditions, meaning the air can contain less water vapour. Therefore, the diffusional growth of ice crystals is more rapid than that of liquid water droplets due to the lower saturation vapour pressure of ice [12].

B ANSYS model

B.1 Volume of Fluid (VOF)

The interphase coupling of the air-flow with water vapour, liquid water and frost, and the transition rate of water vapour to liquid water and liquid water to frost can be expressed with volume fractions. This can be modelled with an Euler-Euler approach [44], in which the different phases are expressed as mathematical continua with a volume fraction. This means that the sum of the volume fractions equals one and that the individual phases are not interpenetrating. The volume fraction is defined in each computational cell. Conservation equations for each phase have a similar structure for all phases. The Volume of Fluid (VOF) model uses a single momentum equation for all fluids, and a volume fraction equation for each fluid in every single computational cell throughout the domain [11]. Compared to other Euler-Euler multiphase models, this model is applicable for all steady or transient tracking of any liquid-gas interface. Only one substance can be defined as a compressible ideal gas. This does not apply to the heat exchanger since all substances are expressed as incompressible.

The Volume of Fluid method is generally used to compute a time-dependent solution [1]. But it is also possible to evaluate a steady-state solution. This only applies if the solution is independent of initial conditions and clear inflow boundary conditions for individual phases are defined. The Volume of Fluid method is especially more flexible and efficient than other methods for free boundary problems. At the mesh boundaries, it is required to set boundary conditions. With these conditions, the Volume of Fluid method computes a layer of fictitious cells surrounding the mesh to create free boundary problems [11].

A continuity equation computes the interface between the individual substances for the volume fraction of each substance. For each substance q , this can be expressed as:

$$\frac{1}{\rho_q} \left[\frac{\partial}{\partial t} (\alpha_q \rho_q) + \nabla \cdot (\alpha_q \rho_q \vec{v}_q) = S_{m,q} \right] \quad (81)$$

The source term ($S_{m,q}$) is defined by a user-defined mass source function, which is described in Appendix A. The continuity function is not solved for the primary phase air. This volume fraction can be derived based on the constraint that the sum of all volume fractions in a computational cell equals one. The material properties in the transport equations are computed by the volume fractions of substances in each control volume [46].

The conservation equations for energy, used in the Volume of Fluid model, are given by Eq. 58. The energy E and temperature T quantities in Eq. 58 are mass-averaged variables. These can be expressed as:

$$E = \frac{\sum_{q=1}^n \alpha_q \rho_q E_q}{\sum_{q=1}^n \alpha_q \rho_q} \quad (82)$$

The resulting velocity field of the momentum equation is also shared among the substances with the same approach. This shared-field approximation reduces the Volume of Fluid method's accuracy for phases with relatively large velocity or temperature differences. Eventually, that could lead to convergence and correctness limitations. These limitations are also imputable for other quantities, like turbulence variables.

Time-dependent simulations are solved using an explicit time scheme. The volume fractions are computed based on values of the previous time step with a standard finite-difference interpolation scheme. The continuity equation for the volume fraction of each substance, Eq. 81, can be rewritten into:

$$\frac{\alpha_q^{n+1} \rho_q^{n+1} - \alpha_q^n \rho_q^n}{\Delta t} V + \sum_f l (\rho_q V_f l^n \alpha_{q,fl}^n) = [S_{m_q}] V \quad (83)$$

The volume fraction can be updated once for each time step or once for each iteration within each time step.

The surface tension along the interface between each pair of phases is also included in the Volume of Fluid model. This tension results from a different attraction between molecules. The attraction of liquid molecules to each other is larger (also cohesion) than the attraction between liquid molecules to air

(adhesion). Due to this effect, the condensed water bubbles will attract other water bubbles to decrease the contact area. The surface tension model is the continuum surface force (CSF) model proposed by [23]. The divergence theorem can express the surface tension force as a volume force.

$$F_{\text{vol}} = \sum_{\text{pairs } ij, i < j} \sigma_{ij} \frac{\alpha_i \rho_i \kappa_j \nabla \alpha_j + \alpha_j \rho_j \kappa_i \nabla \alpha_i}{\frac{1}{2} (\rho_i + \rho_j)} \quad (84)$$

in which σ and κ are the surface tension coefficient and interface curvature, respectively. The interface curvature can be expressed as [46]:

$$\kappa_s = -\kappa_{uns} = -\nabla \cdot \left(\frac{\nabla \alpha_s}{|\nabla \alpha_s|} \right) \quad (85)$$

The influence of the surface tension is based on one dimensionless number: the Weber (We) or capillary number (Ca), depending on the Reynolds number. Surface tension effects can be neglected if $Ca \gg 1$ or $We \gg 1$.

All these equations are coupled and solved with a pressure-based solver. The algorithm is shown in Appendix C.

B.2 Solidification

The Volume of Fluid model is used to model the condensation process of water vapour to liquid water in the air-flow. The condensation mass flux results from a temperature decrease in the air-flow or contact with a surface with a temperature beneath its dew point. This dew point temperature can be below the freezing point of water, resulting in the condensation of water vapour and freezing of liquid water to frost. This leads to a frost layer at the fins and tubes of the heat exchanger. Frosting deteriorates the operation and energy efficiency and reduces the output heating capacity. It reduces the air-flow passages area and acts as a thermal insulator, leading to performance degradation or even shutdown [46].

The freezing process can be modelled with a solidification model. This model uses an enthalpy-porosity formulation to model a liquid-solid mushy zone, which is treated as a porous region with a porosity equal to the liquid fraction [1]. This convective-diffusion mushy region has a moving liquid-solid interface and can handle phase changes at a different material or over a temperature range [8]. The porosity determines the liquid velocity and the level of solidification. During this process, an air gap is created between the wall and the solidified material, which results in thermal contact resistance. These effects are all incorporated within the solidification model. This model is not applicable to compressible flows, and the reactions are solved throughout the entire domain. They are not only restricted to the liquid region.

The solidification model computes a porosity (liquid fraction), based on an enthalpy balance, in each computational cell. When the cell is completely solidified, the porosity becomes zero, and the liquid velocity drops to zero [8]. The governing energy equation is as follows:

$$\frac{\partial}{\partial t} (\rho H) + \nabla \cdot (\rho \vec{u} H) = \nabla \cdot (k \nabla T) + S \quad (86)$$

The enthalpy of the material, also known as the total heat content, can be expressed as

$$H = h_{ref} + \int_{T_{ref}}^T c_p dT + \Delta H \quad (87)$$

The latent heat ΔH is specified as a function of temperature, T .

$$\Delta H = \begin{cases} L, & T \geq T_l \\ L(1 - \beta), & T_l > T \geq T_s \\ 0, & T < T_s \end{cases} \quad (88)$$

The latent heat can vary between zero for a solid, and L for a liquid. The transition process from liquid to solid starts at T_l , and at T_s is the full solidification achieved [46]. For water, both temperatures are equal to each other.

The decrease in momentum, due to the reduced porosity, can be expressed according to the following relation:

$$F = \frac{(1 - \beta)^2}{(\beta^3 + 0.001)} A_{\text{mush}} (\bar{u} - \bar{u}_p) \quad (89)$$

This source term is added to the momentum equation in Eq. ???. The pull velocity \bar{u}_p is the solid velocity due to the pulling of solidified material out of the domain [1]. This relative velocity quantifies the difference between the liquid and solid phases. The effect of this pull velocity is relatively low in heat exchangers due to a low air velocity. Especially in continuous casting processes, it is an essential process to correct for. The pull velocity depends on Young's modulus and Poisson's ratio of the solid and the forces acting on it. The pull velocity is only computed in solid regions.

Also, in turbulence equations, a correction must be made to account for the presence of solid matter in mushy and solidified zones. The correction term can be expressed as:

$$S = \frac{(1 - \beta)^2}{(\beta^3 + \epsilon)} A_{\text{mush}} \phi \quad (90)$$

in which ϕ represents the turbulence quantity (k or ϵ) and A_{mush} represents the mushy zone constant.

The Lever rule describes the species transport equation and assumes infinite diffusion of the liquid water in the mushy zone [55]. This is especially applicable for thinner and less dense frost layers. For thicker frost layers, it develops in a dense structure, such that the density is high and diffusion of vapour in the frost layer is almost negligible. The species transport equation, with mass fractions of the species, can be expressed as:

$$\frac{\partial}{\partial t} (\rho Y_i) + \nabla \cdot (\rho [\beta \vec{v}_1 Y_{i,l} + (1 - \beta) \vec{v}_p Y_{i,\text{sol}}]) = -\nabla \cdot \vec{J}_i + R_i \quad (91)$$

The reaction rate \vec{J}_i is defined as

$$\vec{J}_i = -\rho [\beta D_{i,m,l} \nabla Y_{i,l} + (1 - \beta) D_{i,m,\text{sol}} \nabla Y_{i,\text{sol}}] \quad (92)$$

The liquid velocity (\vec{v}_1) can be computed from the average and pull velocity and the porosity factor.

B.3 Turbulence boundary conditions

The fluid has a zero velocity relative to the boundary in parallel and perpendicular directions for nodes adjacent to the wall. The thin viscous sub-layer also influences nodes close to the wall. The buffer layer governs the transition between this viscous sub-layer and the turbulent free stream. This multi-layered near-wall boundary layer is classified as laminar or turbulent depending on:

$$y^+ = \frac{\Delta y}{u} \sqrt{\frac{\tau_w}{\rho}} \quad (93)$$

The boundary layer is considered turbulent if the value of y^+ is greater than 11.63. The flow is in the log-law region of the turbulent boundary layer [50]. Wall functions, which are accompanied by the log law, are used in this region. This log-law states that the average velocity of a turbulent flow at a certain point is proportional to the logarithmic distance from that point to the wall [51]. The logarithmic law of the wall is used to calculate the shear stress, heat flux and turbulence parameters k and ϵ [41]. This law is valid for flows at high Reynolds numbers.

The near-wall relation for the momentum tangential to the wall consists of a function for the wall shear stress and wall force, respectively given in Eq. 94 and 95. The velocity in a normal direction to the wall is equal to zero due to the significantly low distance to the wall [50].

$$\tau_w = \rho C_\mu^{1/4} k_P^{1/2} u_P / u^+ \quad (94)$$

$$F_s = -\tau_w A_{\text{Cell}} = -\left(\rho C_\mu^{1/4} k_P^{1/2} u_P / u^+\right) A_{\text{Cell}} \quad (95)$$

The turbulent kinetic energy and dissipation rate are respectively given by Eq. 96 and Eq. 97.

$$k = \left(\tau_w u_P - \rho C_\mu^{3/4} k_P^{3/2} u^+ \right) \Delta V / \Delta y_P \quad (96)$$

$$\varepsilon_P = C_\mu^{3/4} k_P^{3/2} / (\kappa \Delta y_P) \quad (97)$$

The energy equation is based on the wall temperature and the temperature in the mesh cell (shown as T_p , the temperature of cell P). The resulting wall heat flux can be expressed as:

$$q_w = -C_P \rho C_\mu^{1/4} k_P^{1/2} (T_P - T_w) / T^+ \quad (98)$$

in which the universal velocity u^+ and temperature T^+ distributions for near-wall turbulent flows are used [50].

C Algorithm flowchart

The model is solved iteratively with a pressure-based solver, which solves the flow problem in a coupled manner. This coupled scheme is more robust and efficient. For transient simulations, this scheme is required when the quality of the mesh or if large time steps are used. Momentum and pressure-based continuity equations are solved together. This full implicit coupling is achieved by an implicit discretization of pressure gradient terms in the momentum equations and an implicit discretization of the face mass flux [1].

Each time step of the transient simulation is solved iteratively until convergence criteria are met. Several outer iterations are required to solve the equations in most cases. With this iterative scheme, the non-linearity of the individual equations and inter-equation couplings are fully accounted for, eliminating the splitting error [1]. The ANSYS iterative algorithm for the heat exchanger model is as follows:

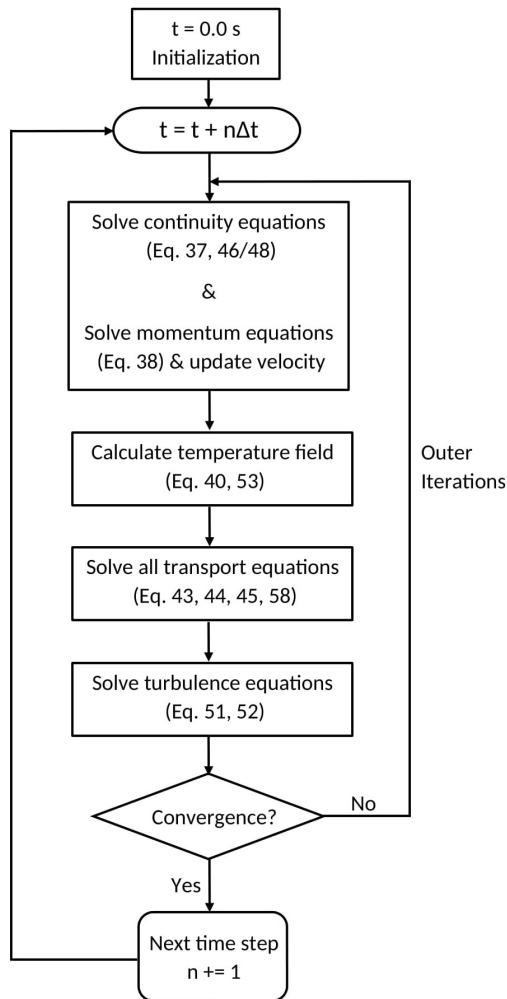


Figure 34: ANSYS heat exchanger model simulation algorithm flowchart

Figure 34 shows that continuity and momentum equations for the density, velocity and pressure are solved together according to the pressure-based solver. Additional temperature, volume fractions and turbulence parameters equations are solved separately according to the order shown in figure 34. If convergence criteria are unmet, another outer iteration is executed with the computed values. Under-relaxation factors limit the maximum difference between the computed values of consecutive iterations. This process continues until the convergence criteria are met so the time can be incremented with the time step Δt .

D Validation results

D.1 Processing results 2D counterflow model

The 2D counterflow ANSYS model has a temperature gradient in the horizontal direction and vertical direction within each fluid domain, shown in Figure 20b. The bulk temperature has been computed to compare the fluid stream of a 2D model with a 1D model. The bulk temperature is the equilibrium temperature that accurately reflects the average temperature of the moving fluid if it is thoroughly mixed [26]. This shows a reference point for properties influenced by the convective heat transfer, particularly in heat exchangers with a flow in ducts.

The bulk temperature can be computed by taking the weighted average of the temperature in the vertical direction based on the velocity in the flow direction. It can be expressed as:

$$T_b(x) = \frac{1}{H\bar{u}} \int_0^H (uT)_x dy \quad (99)$$

in which the bulk temperature at position x is $T_b(x)$, the height of the fluid domain is H , mean velocity in the flow direction is \bar{u} and the mesh cell temperature and velocity is T_x and u_x , respectively.

D.2 Validation results

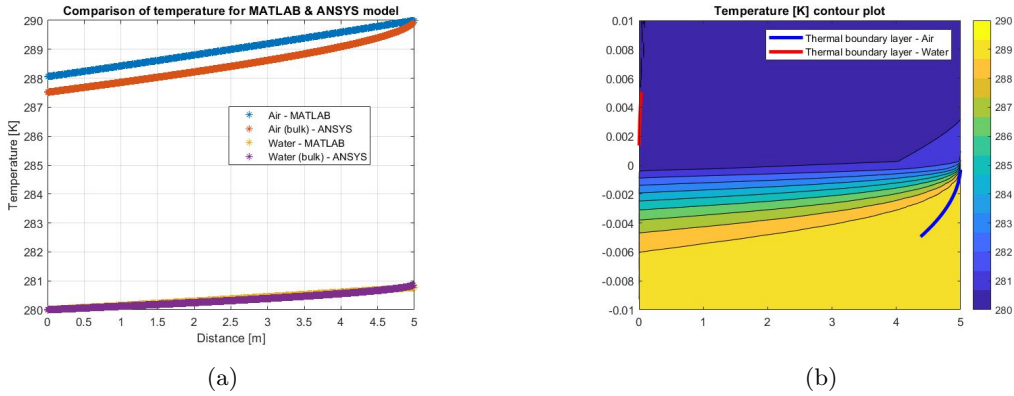
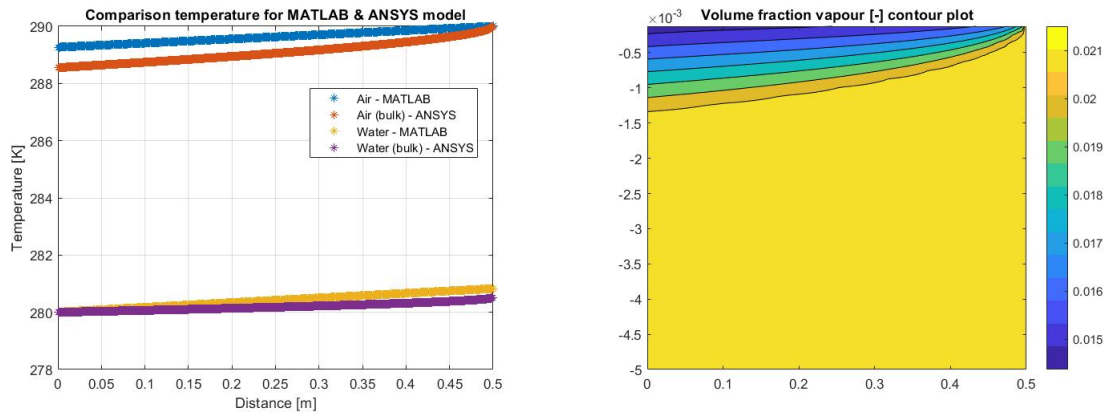


Figure 35: The temperature field of the ANSYS & MATLAB model for Case 4. The bulk temperature (a), and the contour plot of the ANSYS 2D model (b).

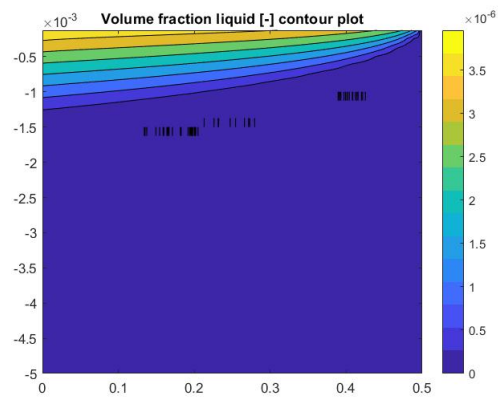
Setup	Heat transfer rate [W]
2D model	407.23
1D model	288.71
NTU method	288.97
LMTD method	288.83

Table 18: The total heat flow rates for the 1D and 2D model, and LMTD and NTU method of Case 4.



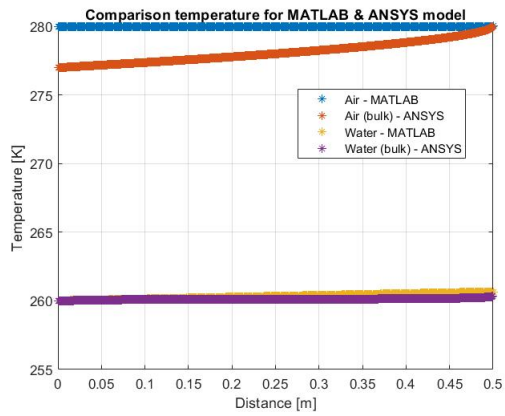
(a)

(b)

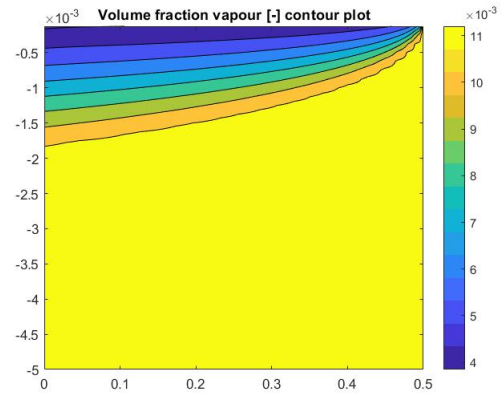


(c)

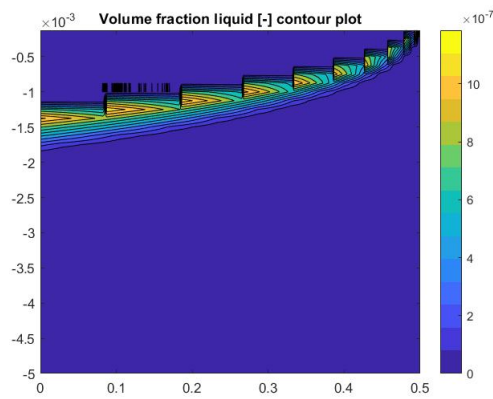
Figure 36: The results of the ANSYS & MATLAB model for Case 5. The bulk temperature (a), and the contour plot of the 2D model with volume fraction of vapour (b) and liquid water (c) in the air domain.



(a)



(b)



(c)

Figure 37: The results of the ANSYS & MATLAB model for Case 6. The bulk temperature (a), and the contour plot of the 2D model with volume fraction of vapour (b) and liquid water (c) in the air domain at ten seconds.

E Results

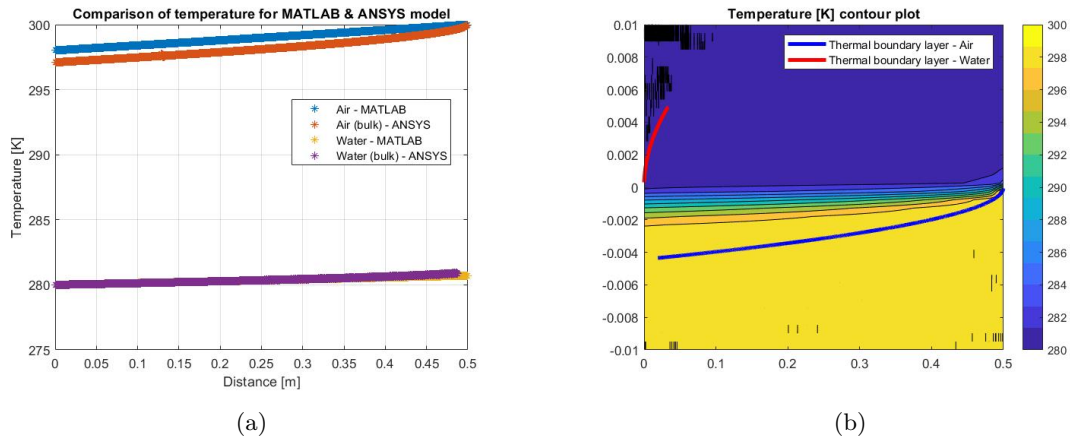


Figure 38: The results of the ANSYS & MATLAB model for Case 1. The bulk temperature (a), and the contour plot of the ANSYS 2D model (b).

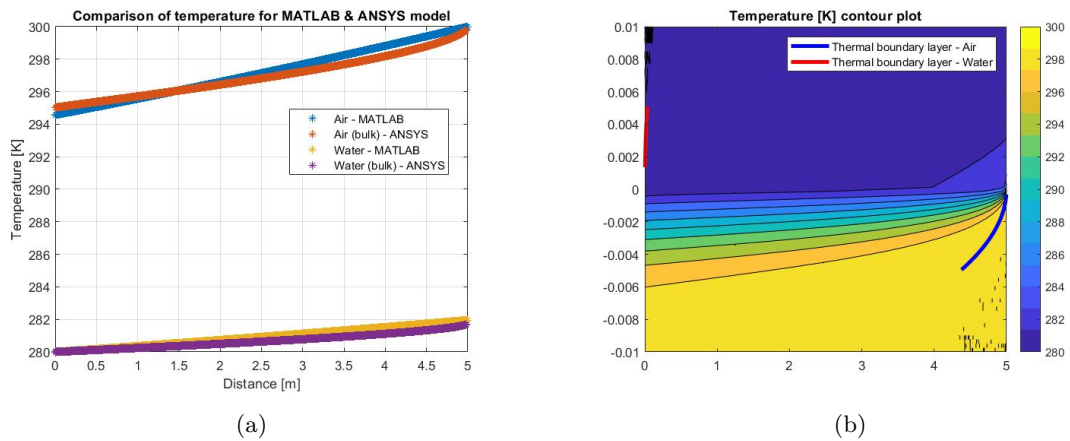


Figure 39: The results of the ANSYS & MATLAB model for Case 2. The bulk temperature (a), and the contour plot of the ANSYS 2D model (b).

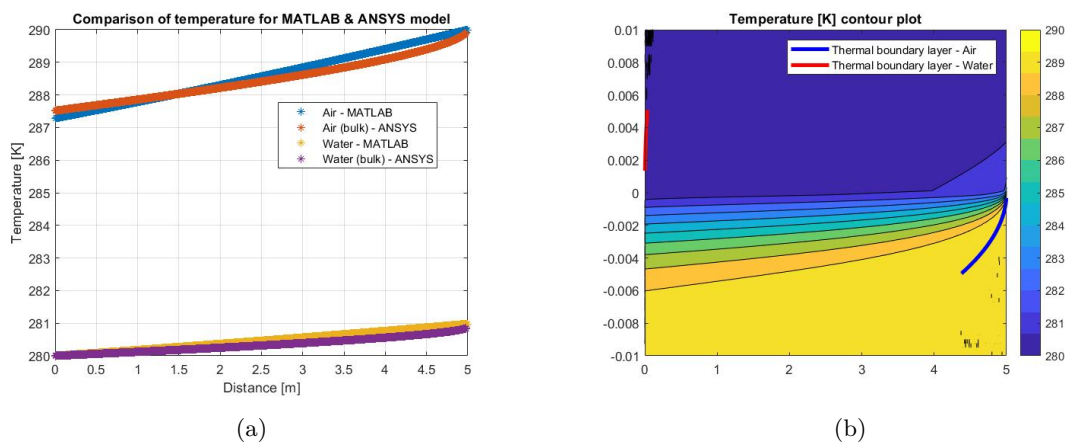
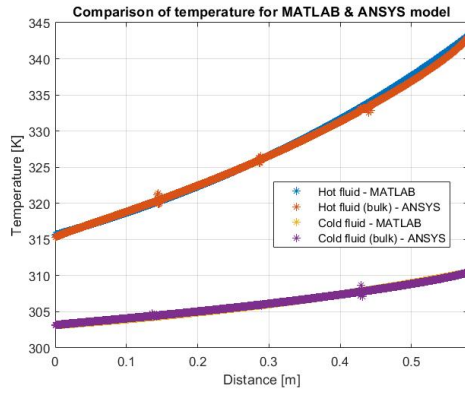
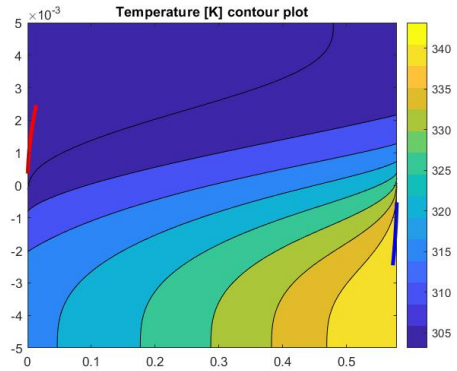


Figure 40: The results of the ANSYS & MATLAB model for Case 3. The bulk temperature (a), and the contour plot of the ANSYS 2D model (b).

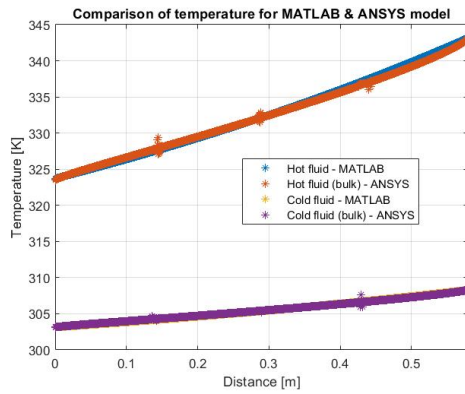


(a)

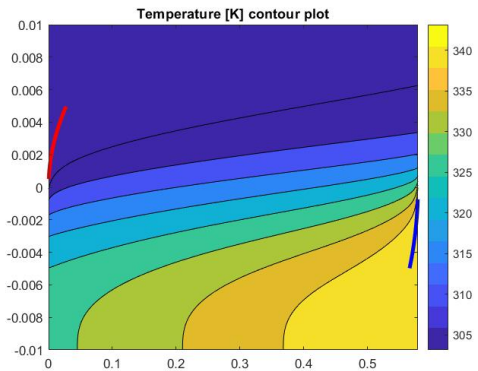


(b)

Figure 41: The results of the ANSYS & MATLAB model for Case 4. The bulk temperature (a), and the contour plot of the ANSYS 2D model (b).

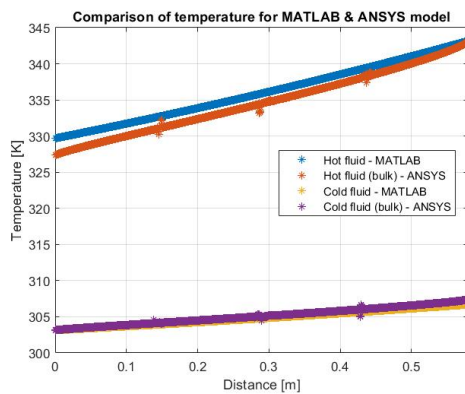


(a)

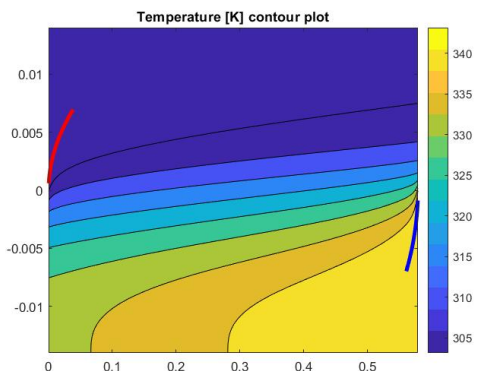


(b)

Figure 42: The results of the ANSYS & MATLAB model for Case 5. The bulk temperature (a), and the contour plot of the ANSYS 2D model (b).

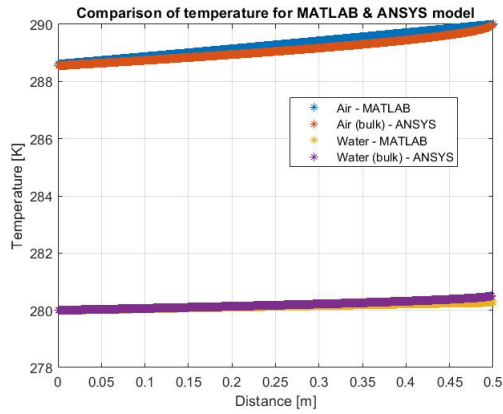


(a)

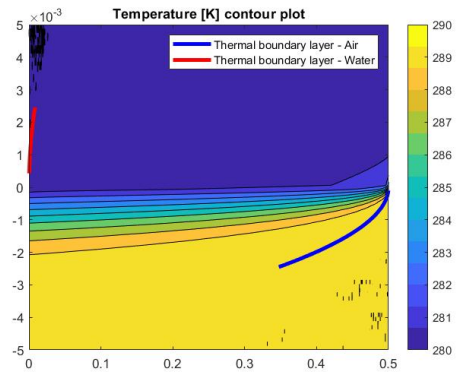


(b)

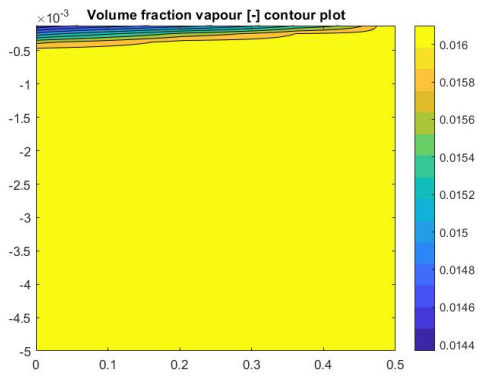
Figure 43: The results of the ANSYS & MATLAB model for Case 6. The bulk temperature (a), and the contour plot of the ANSYS 2D model (b).



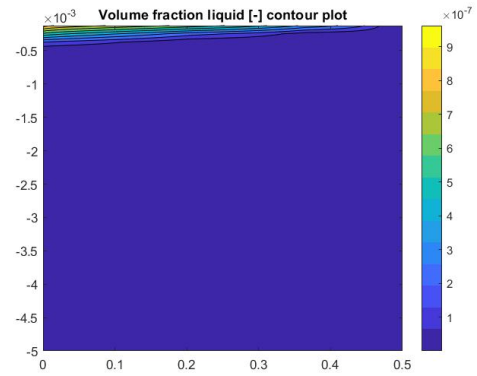
(a)



(b)



(c)



(d)

Figure 44: The results of the ANSYS & MATLAB model for Case 7. The bulk temperature (a), the contour plot of the 2D model with volume fraction of vapour (b) and liquid water (c) in the air domain, and the temperature (d) in both domains.

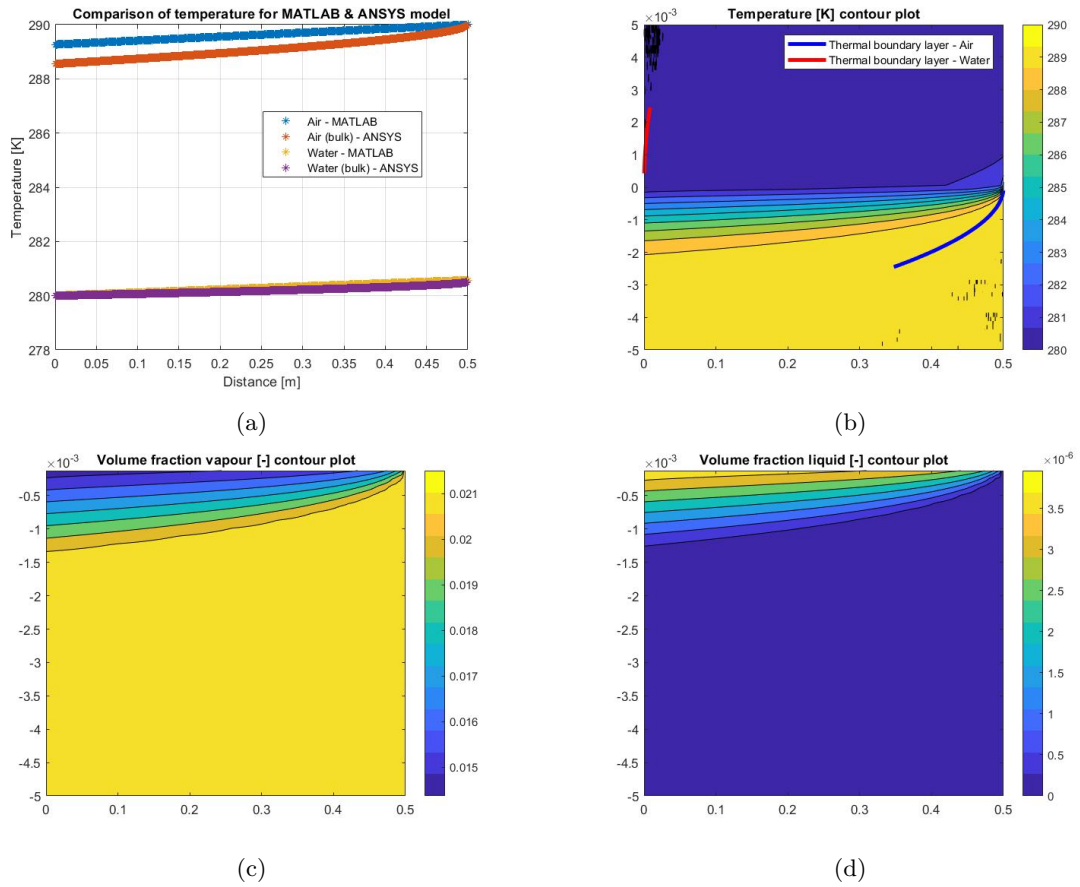


Figure 45: The results of the ANSYS & MATLAB model for Case 8. The bulk temperature (a), the contour plot of the 2D model with volume fraction of vapour (b) and liquid water (c) in the air domain, and the temperature (d) in both domains.

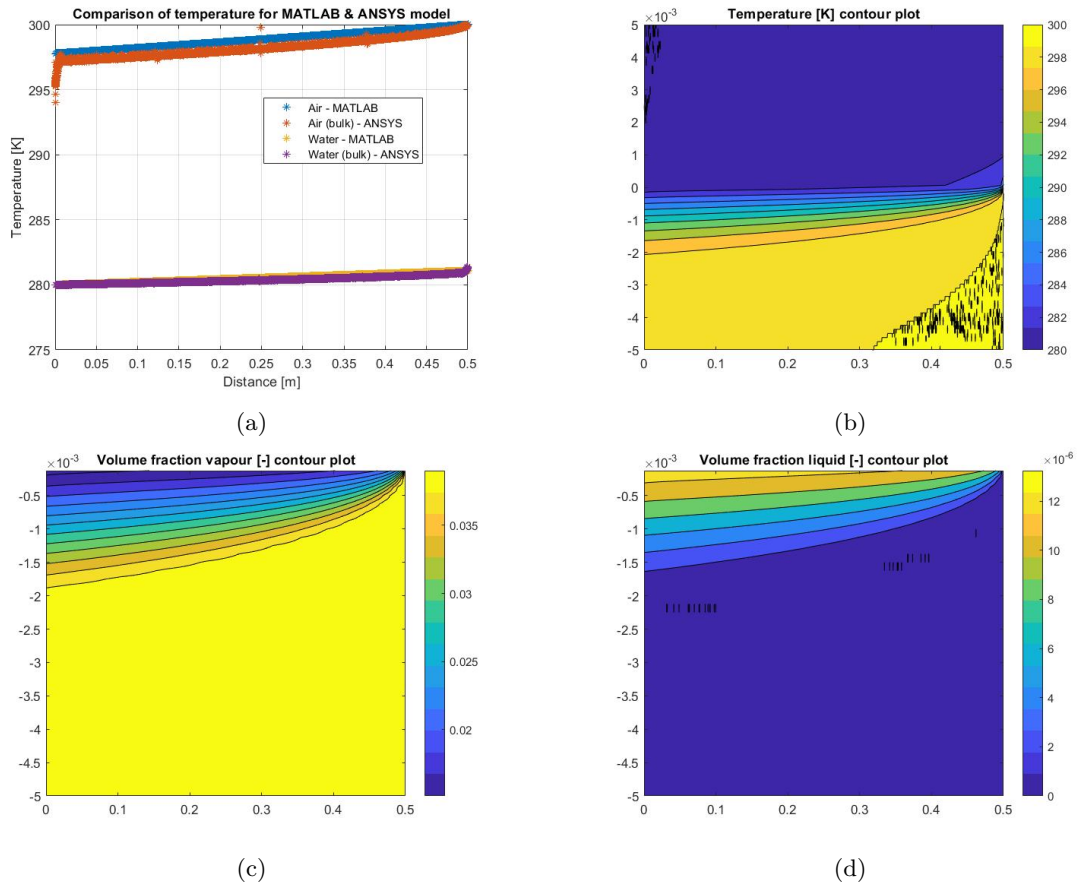


Figure 46: The results of the ANSYS & MATLAB model for Case 9. The bulk temperature (a), the contour plot of the 2D model with volume fraction of vapour (b) and liquid water (c) in the air domain, and the temperature (d) in both domains.

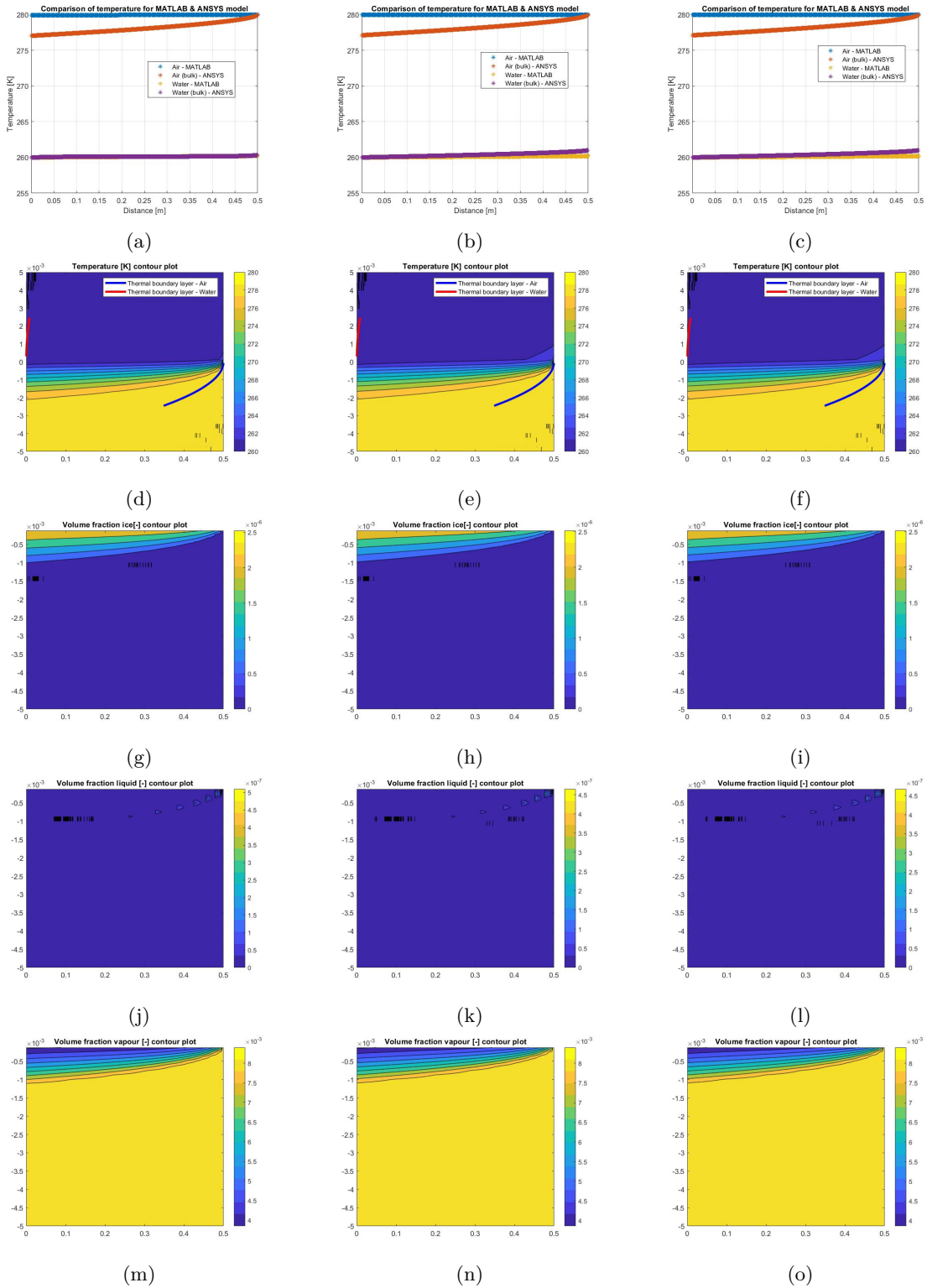


Figure 47: The results of the ANSYS & MATLAB model for Case 10. The bulk temperature (a-c), the contour plot of the 2D model with the temperature in both domains (d-f), the volume fraction of ice (g-i), liquid water (j-l) and vapour (m-o) in the air domain at time 10, 100 and 1800 seconds respectively.

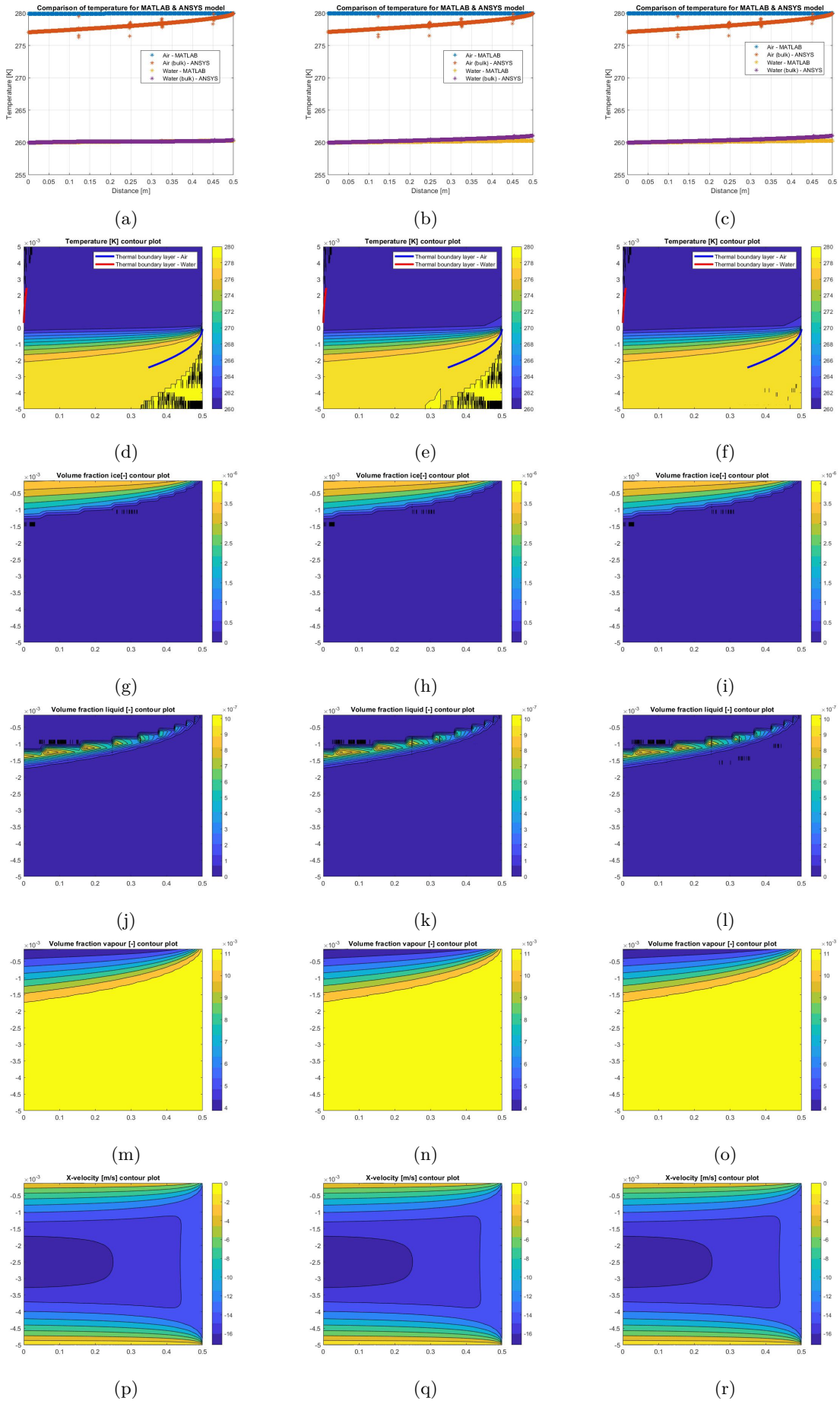


Figure 48: The results of the ANSYS & MATLAB model for Case 11. The bulk temperature (a-c), the contour plot of the 2D model with the temperature in both domains (d-f), the volume fraction of ice (g-i), liquid water (j-l) and vapour (m-o), and velocity profile (p-r) in the air domain at time 10, 100 and 1800 seconds respectively.

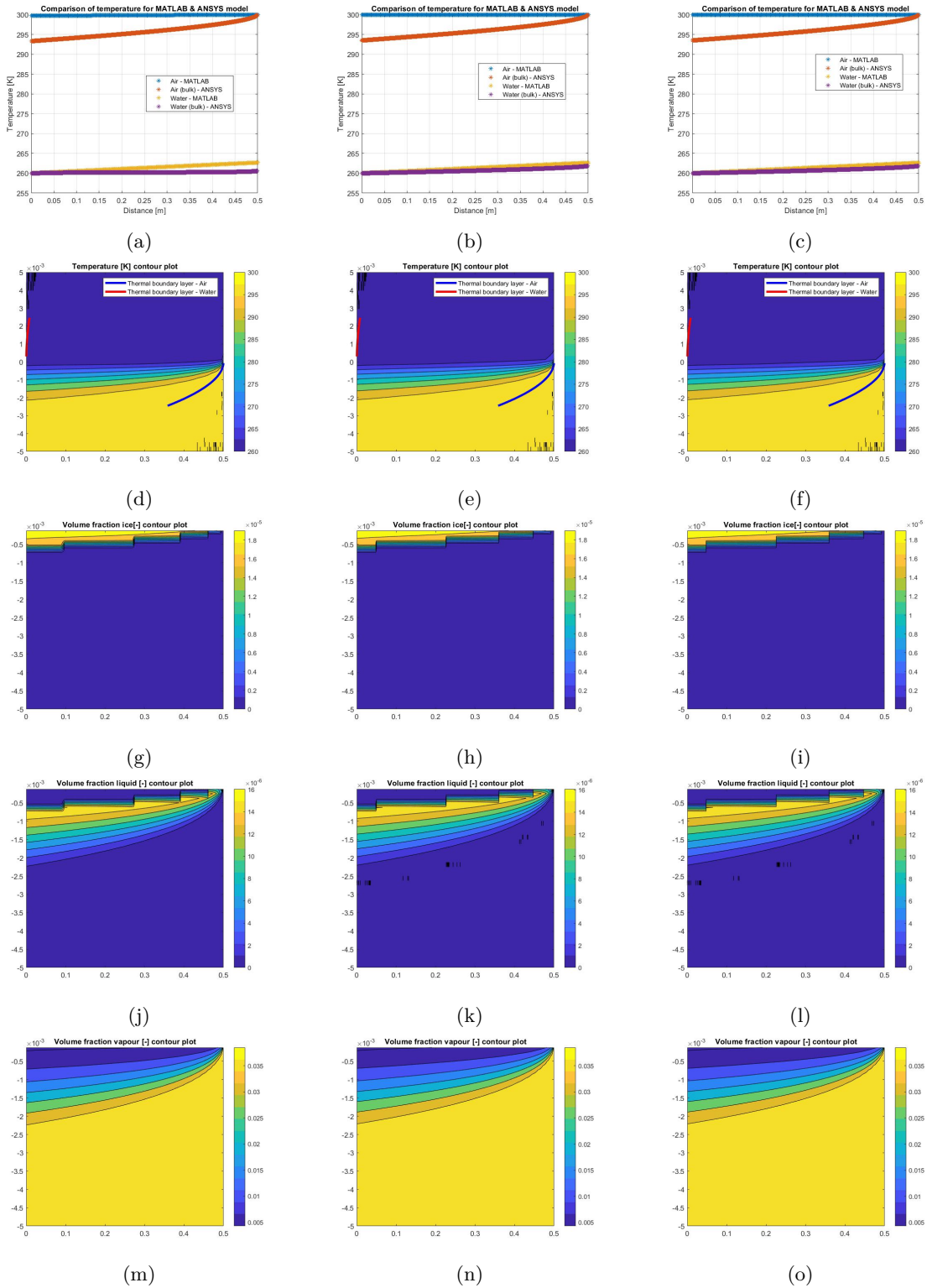


Figure 49: The results of the ANSYS & MATLAB model for Case 12. The bulk temperature (a-c), the contour plot of the 2D model with the temperature in both domains (d-f), the volume fraction of ice (g-i), liquid water (j-l) and vapour (m-o) in the air domain at time 10, 100 and 1800 seconds respectively.

